

Digital Holographic Measurement of Nanometric Optical Excitation on Soft Matter by  
Optical Pressure and Photothermal Interactions

by

David C. Clark

A dissertation submitted in partial fulfillment  
of the requirements for the degree of  
Doctor of Philosophy  
Department of Physics  
College of Arts and Sciences  
University of South Florida

Major Professor: Myung K. Kim, Ph.D.  
Lindsey N. Shaw, Ph.D.  
Garrett Matthews, Ph.D.  
Casey Miller, Ph.D.  
Andreas Muller, Ph.D.

Date of Approval:  
September 5, 2012

Keywords: phase imaging, interferometry, optical manipulation, remote sensing,  
metrology

© Copyright 2012, David C. Clark

Dedicated to my parents, Joyce and Thomas,

and

in loving memory of Chrissy and Russell.

## ACKNOWLEDGEMENTS

I would first like to express my appreciation for my advisor, Dr. Myung K. Kim, for the incredible opportunity to work and learn under his guidance. His expertise in optics and his innovative approach to research are nothing short of superb. In addition, he has an uncanny ability to inspire the work ethic, the motivation, and the careful attention to detail necessary for young researchers to succeed.

I would like to thank each member of my committee for their helpful input and friendly advice throughout the dissertation process. I would like to extend a special thank you to Dr. Lindsey Shaw of the Department of Cell Biology, Microbiology and Molecular Biology for taking a professional yet friendly approach to his position as chairperson of my committee.

Past members of the Digital Holography and Microscopy Laboratory, Bill Ash and Leo Krzewina, were instrumental in mentoring me during my earlier years after joining the group.

My parents, Thomas and Joyce, deserve my eternal gratitude for their endless support and sacrifice over the years. Without this, my accomplishments would not have been possible. Their unfaltering belief in my ability to succeed gives me the strength to do just that. I am forever in their debt for all they have given of themselves.

My brother, Tom, has always been a strong influence on me regardless of the different paths that we have taken in life and the geographical distance between us. His success inspires me and his unmatched friendship bolsters me in everything I do. If not for his belief in my ability to achieve, I may likely have fallen short. For all of this, I express my undying gratitude and hope that I am able to reciprocate even a fraction what I receive from him.

Finally, I would like to thank my friends. Though too numerous to be named here, their contribution is far too important to go unsung. They have kept me encouraged, motivated, and entertained. Looking into the future of these life-long friendships, I can only hope that I am somehow able to repay them in kind.

## TABLE OF CONTENTS

LIST OF FIGURES .....	iii
LIST OF TABLES .....	vi
ABSTRACT .....	vii
CHAPTER 1. GENERAL INTRODUCTION .....	1
1.1 Holography .....	1
1.2 Optical Interaction .....	2
1.3 Dissertation Overview .....	5
1.4 References .....	5
CHAPTER 2. PHASE IMAGING .....	9
2.1 Introduction .....	9
2.2 Techniques .....	10
2.2.1 Zernike phase contrast microscopy .....	10
2.2.2 Differential interference contrast microscopy .....	12
2.2.3 Digital holographic microscopy .....	14
2.3 Digital Holography, Angular Spectrum Method .....	16
2.4 Conclusion .....	18
2.5 References .....	20
CHAPTER 3. THERMAL LENSING .....	21
3.1 Introduction .....	21
3.2 Theory .....	23
3.3 Experiments .....	25
3.3.1 Measurement application using high-power excitation .....	26
3.3.2 Thermal lens time-resolution .....	36
3.3.3 Improved precision for standard-power excitation .....	37
3.4 Discussion and Conclusion .....	45
3.5 References .....	47
CHAPTER 4. CONTINUOUS WAVE OPTICAL RADIATION PRESSURE .....	49
4.1 Introduction .....	50
4.2 Theory .....	52
4.3 Experiments .....	58

4.3.1 Thermal behavior of benzyl alcohol .....	61
4.3.2 Detection of optical pressure effect .....	64
4.4 Discussion and Conclusion .....	66
4.5 References .....	67
CHAPTER 5. PULSED OPTICAL PRESSURE AND APPLICATION .....	70
5.1 Introduction .....	71
5.2 Theory .....	76
5.3 Experiments .....	80
5.4 Discussion and Conclusion .....	83
5.5 References .....	85
CHAPTER 6. CONCLUSIONS AND FUTURE WORK .....	89
6.1 Summary of conclusions .....	89
6.2 Future work .....	94
6.3 References .....	96
BIBLIOGRAPHY .....	99
APPENDICES .....	100
Appendix A: Apparatus Photographs .....	101
Appendix B: Computer Programs .....	105
Appendix C: List of Publications .....	117
ABOUT THE AUTHOR .....	End Page

## LIST OF FIGURES

Figure 2.1.	Zernike phase contrast microscope.....	11
Figure 2.2.	Differential interference contrast microscope.....	13
Figure 2.3.	Digital holography by angular spectrum method.....	15
Figure 2.4.	Phase aberration compensation.....	19
Figure 3.1.	Cross-sectional representation of a thermal lens in a cuvette of liquid.....	22
Figure 3.2.	Experimental apparatus.....	27
Figure 3.3.	Phase images of methanol with, A) no excitation beam and B) 700 mW excitation beam power.....	30
Figure 3.4.	Cross-sectional profile of the thermal lens shown in Figure 3.3B (dashed line).....	31
Figure 3.5.	Experimental data (scatter plots) and model predictions (solid lines) at 330mW, 440mW, and 550mW excitation powers for both A) methanol and B) ethanol.....	33
Figure 3.6.	Improved phase images of a sample, A) with no excitation and B) with optical excitation.....	35
Figure 3.7.	Experimental data (scatter plots) and 2D infinite model predictions (solid lines) at several time-resolved stages of the thermal lens excitation event in methanol.....	37
Figure 3.8.	Experimental apparatus.....	39
Figure 3.9.	Example phase maps of a sample with (a) no excitation and (b) optical excitation resulting in a thermal lens.....	41

Figure 3.10.	Single cross-section through center of the thermal lens phase structure in benzyl alcohol. ....	43
Figure 3.11.	Phase shift vs. radial distance from center of excitation beam for experimental data (dotted) and model predictions (solid) for a thermal lens in benzyl alcohol. ....	44
Figure 4.1.	Model prediction for the thermal lens (TL) and optical pressure (Opt Press) effects for a sample of layered benzyl alcohol and water with an interfacial tension of 3.5 mN/m. ....	58
Figure 4.2.	Experimental apparatus. ....	59
Figure 4.3:	Time-resolved thermal lens phase shift measurements (at $r = 900 \mu\text{m}$ ) of benzyl alcohol with model prediction (solid line). ....	62
Figure 4.4.	Phase shift data (scatter) and model predictions (solid) at 5 points in time of an excitation event. ....	65
Figure 5.1.	Experimental apparatus. ....	73
Figure 5.2.	Time-dependent surface response to optical impulse for DI water. ....	74
Figure 5.3.	Time-series data. ....	75
Figure 5.4.	Capillary wave front velocity. ....	79
Figure 6.1.	Application to biological cell membrane. ....	95
Figure A.1.	Early apparatus. ....	101
Figure A.2.	Improved apparatus. ....	102
Figure A.3.	Acousto-Optic Modulator (AOM) shutter system. ....	103
Figure A.4.	Pulsed optical pressure, time resolved DH-QPM apparatus complete. ....	104
Figure B.1.	Front panel and block diagram of the Fourier Transform VI. ....	105
Figure B.2.	Front panel and block diagram of the sub-VI for filtered angular spectrum numerical diffraction. ....	106
Figure B.3.	Front panel of the sub-VI for phase correction routines. ....	107
Figure B.4.	Block diagram for wavefront curvature mismatch correction. ....	108

Figure B.5.	Block diagram for general background phase aberration compensation. ....	108
Figure B.6.	Block diagram for phase level stabilization.....	109
Figure B.7.	Block diagram for phase tilt correction. ....	109

## LIST OF TABLES

Table 3.1.	Experimental Parameters for methanol and ethanol .....	32
Table 3.2.	Experimental parameters for methanol. ....	36
Table 3.3.	Experimental Parameters for Benzyl Alcohol. ....	42
Table 4.1.	Experimental parameters for benzyl alcohol and water layers. ....	64
Table 6.1.	Comparison of improved measurement precision. ....	91
Table 6.2.	Experimental results for surface tension (mN/m). ....	93

## ABSTRACT

In this dissertation we use digital holographic quantitative phase microscopy to observe and measure phase-only structures due to induced photothermal interactions and nanoscopic structures produced by photomechanical interactions. Our use of the angular spectrum method combined with off-axis digital holography allows for the successful hologram acquisition and processing necessary to view these phenomena with nanometric and, in many cases, subnanometric precision. We show through applications that this has significance in metrology of bulk fluid and interfacial properties.

Our accurate quantitative phase mapping of the optically induced thermal lens in media leads to improved measurement of the absorption coefficient over existing methods. By combining a mathematical model describing the thermal lens with that describing the surface deformation effect of optical radiation pressure, we simulate the ability to temporally decouple the two phenomena. We then demonstrate this ability experimentally as well as the ability of digital holography to clearly distinguish the phase signatures of the two effects. Finally, we devise a pulsed excitation method to completely isolate the optical pressure effect from the thermal lensing effect.

We then develop a noncontact purely optical approach to measuring the localized surface properties of an interface within a system using a single optical pressure pulse and a time-resolved digital holographic quantitative phase imaging technique to track a

propagating nanometric capillary disturbance. We demonstrate the method's ability to accurately measure the surface energy of pure media and chemical monolayers formed by surfactants with good agreement to published values. We discuss the possible adaptation of this technique to applications for living biological cell membranes.

# **CHAPTER 1**

## **GENERAL INTRODUCTION**

This chapter presents a brief history of holography, an introduction to optical interactions with media along with the motivation for this research, and an outline of the organization of this dissertation. The principles of holography contribute to several important imaging mechanisms necessary for our investigations of interactions of light and soft matter. The thermal and weak optical pressure interactions of light and fluid matter have significant relevance in metrology of fluid and surface properties. These principles will be introduced here and discussed in detail throughout the dissertation.

### **1.1 Holography**

Holography was discovered by Dennis Gabor in 1948 as a technique in which the wavefronts from an object were recorded and reconstructed using a background reference wave in such a way that the amplitude and the phase of the wave field were recovered. Gabor called the recorded interference pattern a hologram from the Greek word holos, meaning whole, because it contained the full three-dimensional wave field as amplitude and phase [1-3]. In 1967, Joseph Goodman demonstrated the feasibility of numerical reconstruction of holographic images using a densitometer-scanned holographic plate [4]. Schnars and Juptner, in 1994, were the first to use a CCD camera interfaced with a

computer as the input, completely eliminating the photochemical process, in what is now referred to as digital holography [5-7].

The application of digital holography in microscopy is especially important due to the narrow depth of focus of high-magnification systems [8, 9]. Numerical focusing to different image planes can be accomplished from a single captured hologram. Direct access to phase information can be used for numerical compensation for various aberrations of optical systems, such as wavefront curvature and anamorphism [10]. Digital holography has been a particularly useful tool in such areas as metrology, deformation measurement, and vibrational analysis [11-13]. Digital holographic microscopy has been applied to imaging of microstructures and biological systems [11, 14, 15].

## **1.2 Optical interactions**

Measurement of optical radiation pressure effects can be a very useful tool in soft matter physics for the efficient characterization of fluid interfaces and membranes. Although it is one of the most noninvasive methods, very little work has been done in this area due to the difficulty in observing these effects. Surface deformation on a fluid interface by optical radiation pressure using a continuous wave laser source is typically very weak. The output power of these lasers, even when focused tightly on the surface, is often insufficient to overcome the surface tensions of most fluid interfaces enough to form readily observable deformations. For this reason, pulse laser sources are often used to amplify laser intensity and, therefore, the resulting deformation to a more easily observable level [16]. Alternatively, standard liquids may be replaced with well-

engineered temperature sensitive phase-separating microemulsions that form a fluid-fluid interface with exceptionally reduced surface tension near a critical temperature [17, 18]. The method often used to sense these deformations is far-field diffraction. The bent surface of a fluid acts as a lens and the profile of the exiting laser beam [16-18], or separate probing laser beam [19], can be analyzed to deduce the shape and size of the deformation.

It has been our intent to use the method of digital holographic microscopy to image such deformations with nanometric precision and length scales. The quantitative phase analysis inherent to digital holography [20, 21] yields an imaging method which can observe very slight surface deformations of standard fluid-fluid interfaces by continuous wave or pulsed laser optical radiation pressure. The freedom to choose from a potentially broad selection of fluids is advantageous as the optical properties are likely to be well known making conversion of the optical phase images to real physical deformations quite straightforward. The relationship between surface deformation by known optical forces and other important surface properties, such as surface tension and viscosity, has been derived [22, 23].

Many studies on optical radiation pressure have dismissed thermal effects simply due to the transparent nature of the media under observation. In fact, even transparent media can have a thermal effect which is far dominant to the effect of optical radiation pressure. For this reason, it was a necessary step to study and understand these effects in working toward the study of optical radiation pressure effects.

When a beam of incident light passes through a medium, that medium may absorb some of the energy of the beam. This absorbed energy, in turn, will cause a change in

temperature of the absorbing region of the media which then will diffuse to other parts of the medium and its surroundings in a regular way determined by the thermal properties of the media involved. Because the index of refraction is a temperature dependant property, the temperature gradient also causes a refractive index gradient. This causes a change in the optical path length to any light incident through the affected area of the media. This effect is referred to as thermal lensing and has been the focus of many other studies as an indicator of the optical and thermal properties of materials [24, 25].

If a thermal lens is present during the course of an optical radiation pressure study, any far-field diffraction observed is actually the result of the superposition of the two lens effects. Our use of digital holography as an imaging method has proven to be a valuable indicator of both thermal and optical effects. Through our work in thermal lensing, it was possible to decouple these effects so that optical radiation pressure deformations could be easily observed. As will be discussed in detail below, these deformations always result in a longer optical path length (positive phase shift) within the structure. Meanwhile, the thermal lensing effect results in a shortened optical path length (negative phase shift). Additionally, these two effects differ greatly in the time scale with which they occur.

It was the goal of our research to make use of these differences to produce quantitative phase analyses of the two effects with excellent accuracy and precision using a Mach-Zehnder configured digital holographic microscope with an integrated optical excitation arm. The deformation can therefore be measured with nanometric precision enabling the possibility of calculating surface properties using non-invasive “light-only”

manipulation and imaging techniques. This is ideal for our current work on fluid interfaces and the future application to biological cell membranes.

### **1.3 Dissertation overview**

This dissertation is organized in a way that should take the reader through the necessary steps of our research goals with similar reconstruction of the chronology of accomplishments. Chapter 2 will provide the background and theory of digital holographic quantitative phase microscopy, the necessary imaging tool to achieve our high-precision, nanometric observations. In chapter 3, we discuss not only the necessary mapping of the spatial and temporal behavior of the thermal lens, but apply our highly accurate and precise methods to make improved measurements of photothermal properties of media. At this point, with the thermal lens, well-modeled and tested, we discuss our decoupling and observation of thermal and optical pressure effects using a continuous wave laser excitation source in chapter 4. Then, with both of these effects modeled and tested, chapter 5 discusses our use of short laser pulsed excitation to produce a purely optical pressure effect and our successful, unique application of this achievement.

### **1.4 References**

1. Gabor, D., "A new microscope principle," *Nature* **161**, 777-778 (1948).
2. Gabor, D., "Microscopy by reconstructed wavefronts," *Proc. Roy. Soc.* **A197**, 454-487 (1949).

3. Gabor, D., "Microscopy by reconstructed wavefronts: II," Proc. Phys. Soc. **B62**, 449-469 (1951).
4. Goodman, J.W., and Lawrence, R.W., "Digital image formation from electronically detected holograms," Appl. Phys.Lett. **11**, 77-79 (1967).
5. Schnars, U., "Direct phase determination in hologram interferometry with use of digitally recorded holograms," J. Opt. Soc. Am. A **11**, 2011-5 (1994).
6. Schnars, U., and Jueptner, W., "Direct recording of holograms by a CCD target and numerical reconstruction," Appl.Opt. **33**, 179-181 (1994).
7. Schnars, U., and Jueptner, W., "Digital recording and numerical reconstruction of holograms," Meas. Sci. Technol. **13**, R85-R101 (2002).
8. Barty, A., Nugent, K.A., Paganin, D., and Roberts, A., "Quantitative optical phase microscopy," Opt. Lett. **23**, 817 (1998).
9. Cuche, E., Bevilacqua, F., and Depeursinge, C., "Digital holography for quantitative phase-contrast imaging," Opt. Lett. **24**, 291 (1999).
10. Ferraro, P., De Nicola, S., Finizio, A., Coppola, G., Grilli, S., Magro, C., and Pierattini, G., "Compensation of the inherent wave front curvature in digital holographic coherent microscopy for quantitative phase-contrast imaging," Appl. Opt. **42**, 1938-46 (2003).
11. Xu, M.L., Peng, X., Miao, J., and Asundi, A., "Studies of digital microscopic holography with applications to microstructure testing," Appl. Opt. **40**, 5046-51 (2001).
12. Pedrini, G., and Tiziani, H.J., "Quantitative evaluation of two-dimensional dynamic deformations using digital holography," Opt. Laser Technol. **29**, 249-56 (1997).

13. Picart, P., Leval, J., Mounier, D., and Gougeon, S., "Some opportunities for vibration analysis with time averaging in digital Fresnel holography," *Appl. Opt.* **44**, 337–43 (2005).
14. Haddad, W.S., Cullen, D., Solem, J.C., Longworth, J.W., McPherson, A., Boyer, K., and Rhodes, C.K. "Fourier-transform holographic microscope," *Appl. Opt.* **31**, 4973–8 (1992).
15. Xu, W., Jericho, M.H., Meinertzhagen, I.A., and Kreuzer, H.J., "Digital in-line holography for biological applications," *Proc. Natl. Acad. Sci. USA* **98**, 11301-05 (2001).
16. Ashkin, A. and Dziedzic, J.M., "Radiation Pressure on a Free Liquid Surface," *Phys. Rev. Lett.* **30**, 139-142 (1973).
17. Casner, A. and Delville, J.-P., "Adaptative Lensing Driven by the Radiation Pressure of a Continuous-Wave Laser Wave Upon a Near-Critical Liquid–Liquid Interface," *Opt. Lett.* **26**(18), 1418-1420 (2001).
18. Chraïbi, H., Lasseux, D., Arquis, E., Wunenburger, R., Delville, J.-P., "Simulation of an Optically Induced Asymmetric Deformation of a Liquid–Liquid Interface," *Eur. J. Mech. B/Fluids* **27**, 419–432 (2008).
19. Sakai, K., Mizuno, D., and Takagi, K., "Measurement of Liquid Surface Properties by Laser-Induced Surface Deformation Spectroscopy," *Phys. Rev. E* **63**, 046302 (2001).
20. Cuche, E., Bevilacqua, F., Depeursinge, C., "Digital holography for quantitative phase-contrast imaging," *Opt. Lett.* **24**(5), 291 (1999).
21. Mann, C. J., Yu, L., Lo, C.-M., and Kim, M. K., "High-resolution quantitative phase-contrast microscopy by digital holography," *Opt. Express* **13**, 8693 (2005).

22. Mitani, S., Sakai, K., “Measurement of ultralow interfacial tension with a laser interface manipulation technique,” *Phys. Rev. E* **66**, 031604 (2002).
23. Yoshitake, Y., Mitani, S., Sakai, K., Takagi, K., “Measurement of high viscosity with laser induced surface deformation technique,” *J. Appl. Phys.* **97**, 024901 (2005).
24. Marcano, A., Loper, C., Melikechi, N., “High sensitivity absorption measurement in water and glass samples using a mode-mismatched pump-probe lens method,” *Appl. Phys. Lett.* **78**, 3415–3417 (2001).
25. Cabrera, H., Marcano, A., and Castellanos, Y., “Absorption coefficient of nearly transparent liquids measured using thermal lens spectrometry,” *Condensed Matter Physics* **9**, No. 2(46), 385-389 (2006).

## **CHAPTER 2**

### **PHASE IMAGING**

As will become quite apparent in the next few chapters, standard optical microscopy is insufficient to observe the structures presented in this dissertation. In fact, some structures are merely the result of variations in index of refraction which would be invisible to a standard microscope regardless of the structure size. Still other structures that we will discuss vary in physical dimensions on a scale that is far too small to be detected by standard light wavelengths. In this chapter, the concept of phase imaging and quantitative phase imaging will be described as this is a necessary imaging tool to overcome these barriers [1-4].

#### **2.1 Introduction**

Light may undergo phase variations as it passes through objects and media and structures within media. These normally invisible phase variations can be converted into observable amplitude variations by a number of phase imaging techniques. Some of the more popular techniques such as Zernike phase contrast (ZPC) and differential interference contrast (DIC) can qualitatively perform this conversion; however, if measurements are necessary, a quantitative technique must be employed.

In our research, we have used digital holographic quantitative phase microscopy (DH-QPM) so that our observations of phase modulation could be converted to real-world measurements of properties and structures. Rather than producing merely a qualitative contrast image of the phase differences, DH-QPM makes use of diffraction theory and holography to produce a complete phase variation map of the area of interest.

## **2.2 Techniques**

In this section we will discuss the qualitative phase contrast techniques as well as DH-QPM. The contrast methods, ZPC and DIC, give insight into the development and usefulness of phase imaging while DH-QPM makes complete use of the three-dimensional information that can be captured by a two-dimensional CCD array.

### **2.2.1 Zernike phase contrast microscopy**

Phase contrast microscopy was first proposed by Frits Zernike in 1934. It is a phase contrast-enhancing optical technique that can be used to produce high-contrast images of transparent specimens [5, 6].

Figure 2.1 shows a diagram of a phase contrast microscope and the schematic illustration of the phase contrast optical path. Partially coherent illumination, from the light source is directed through a collector lens and focused through the annulus and condenser. Wavefronts passing through the annulus illuminate the specimen and pass through unperturbed or are diffracted by structures and phase gradients present in the sample. Both non-diffracted and diffracted light waves are collected by the objective and

separated at the rear focal plane by the phase plate, then focused at the image plane to form the final phase contrast image observed by the camera.

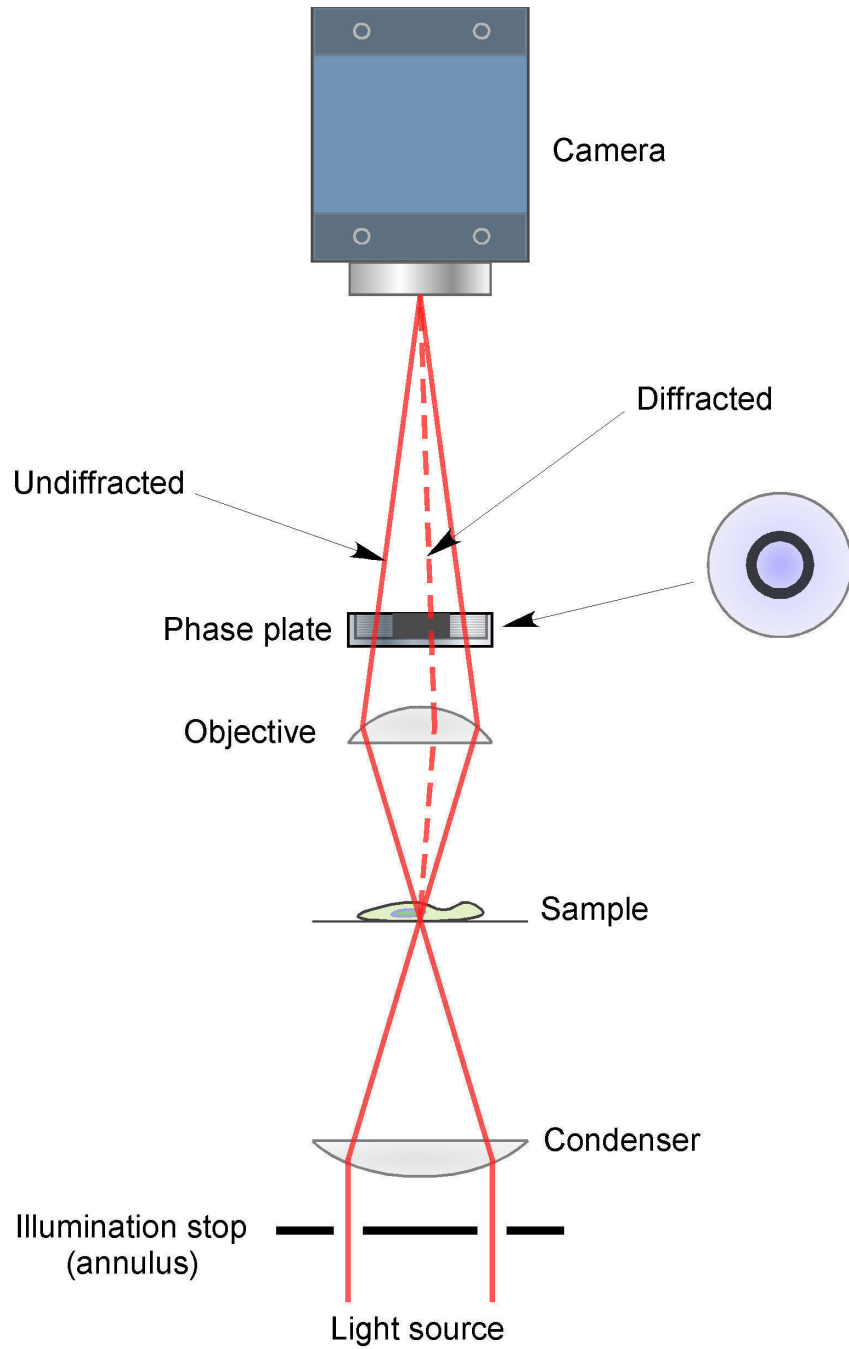


**Figure 2.1.** Zernike phase contrast microscope.

### **2.2.2 Differential interference contrast microscopy**

Differential interference contrast microscopy uses interferometry of two polarized light beams which take different paths through a sample [7]. The length of each optical path differs causing the beams to interfere when they are combined. This gives the appearance of a three-dimensional image due to the resulting contrast.

A schematic of a DIC microscope is shown in Figure 2.2. The incoming light is polarized and then split into two beams of perpendicular polarization by the Wollaston prism. These two beams are focused by the condenser so that they pass through two adjacent points in the sample separated usually by a value similar to the resolution of the microscope. The two optical paths result in a phase difference. The two beams then pass through the objective lens which focuses the beams for the second Wollaston prism to recombine them at a single polarization causing them to interfere due to phase variation. The full resulting image is therefore a combination of two bright field images slightly offset from one another, thus containing amplitude variations representing the phase variations.

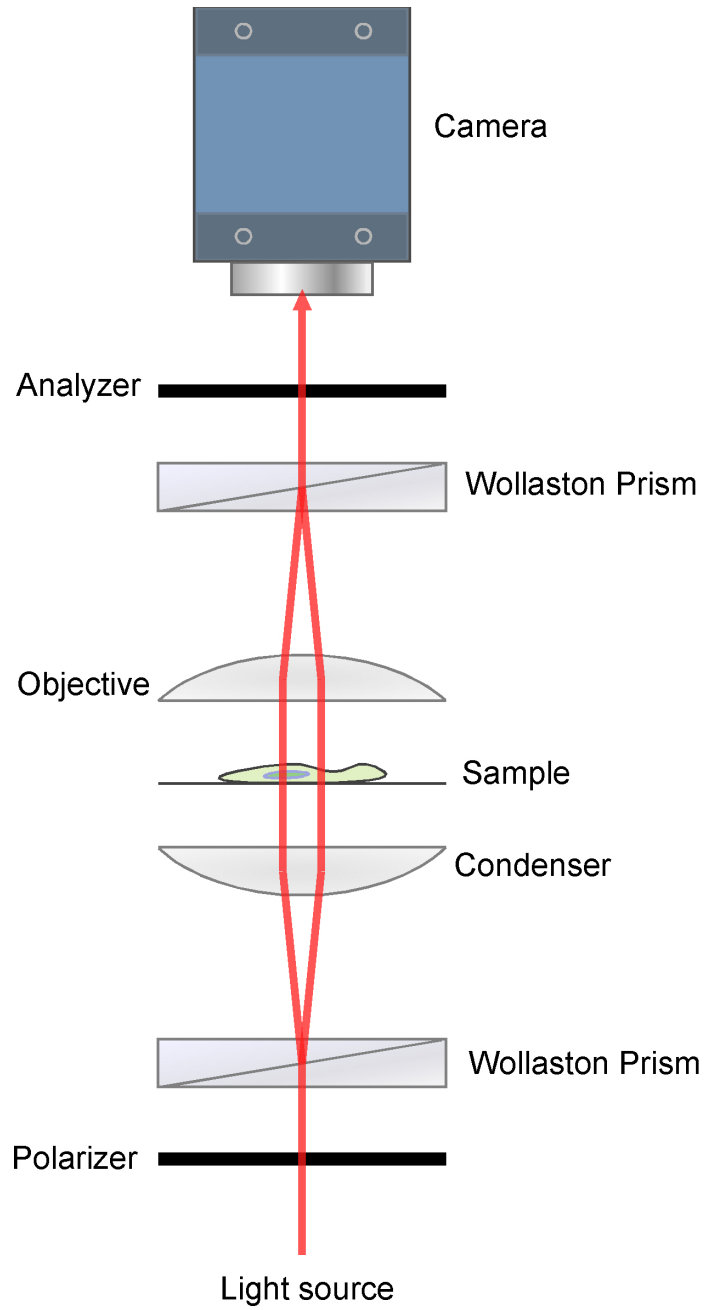


**Figure 2.2.** Differential interference contrast microscope.

### **2.2.3 Digital holographic microscopy.**

In ZPC and DIC microscopy, the phase to amplitude conversion is nonlinear; therefore, these methods cannot be used for quantitative phase analysis. Quantitative phase information yields a measure of the optical path length the light has travelled. Thus, a quantitative phase image can be converted to physical thickness or optical density variations within the sample. A quantitative phase image, therefore, truly carries three-dimensional information.

Due to advancement in computer processing speeds and the availability of high-resolution CCD cameras, digital holography has emerged in recent years as a powerful quantitative phase imaging technique. Just as in conventional holography, digital holographic recording is done optically, but the recording media is a CCD array, which allows for easy digitization and storage of the hologram. This recording then contains both the amplitude and phase information of the signal.

After the hologram is recorded, the process of reconstructing the amplitude and phase information is accomplished by numerically diffracting and propagating a reference wave through the hologram. The amplitude and phase maps produced are simply the amplitude and phase of a set of complex numbers. The process of holographic reconstruction is therefore reduced to a numerical diffraction problem, which is done entirely by a computer. A schematic of this process is shown in Figure 2.3.

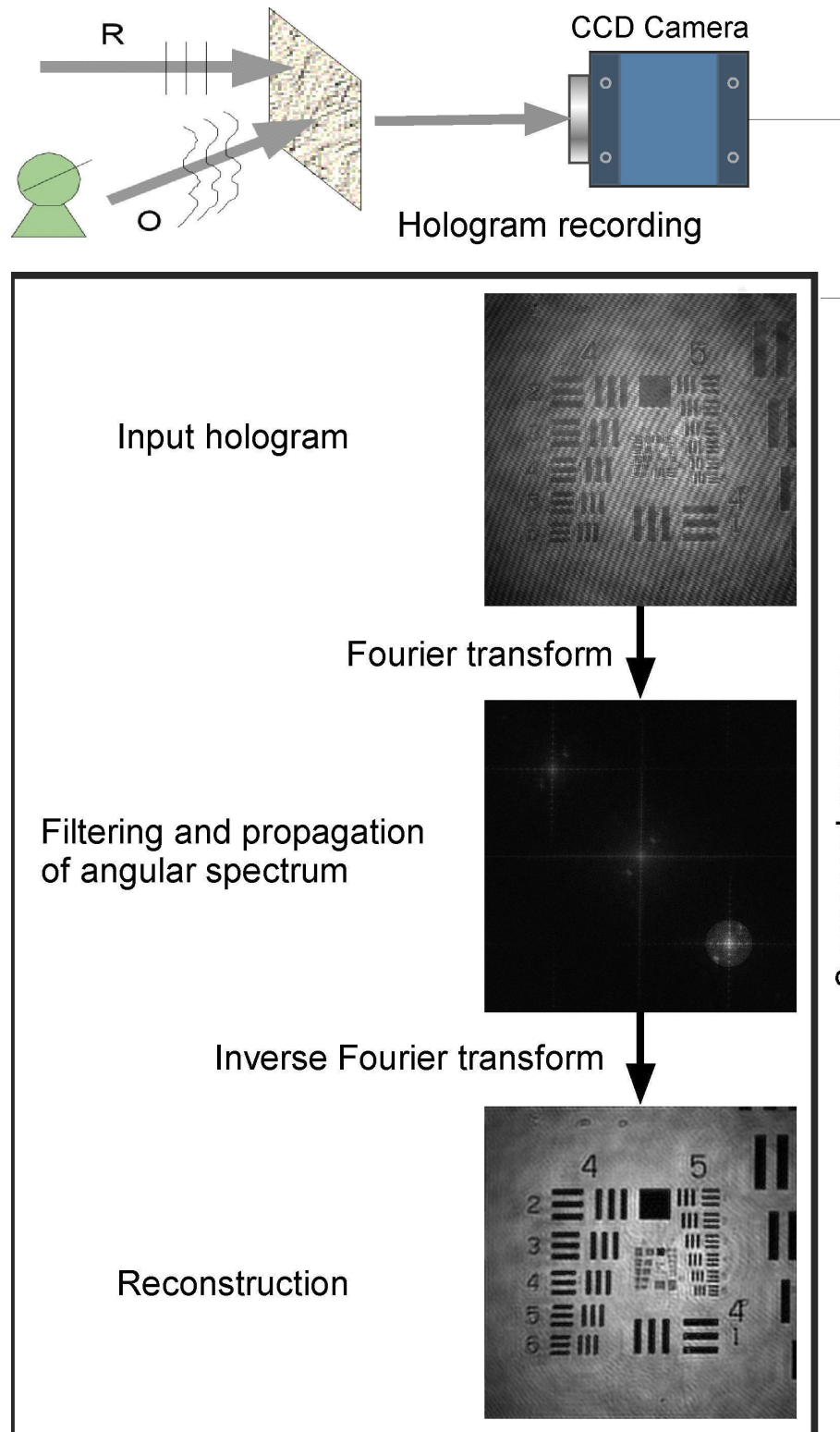


**Figure 2.3.** Digital holography by angular spectrum method.

One of the main advantages of digital holography is that image processing algorithms can be easily applied to various stages of the process. In our research, we use the angular spectrum method of numerical processing which provides significant advantages in filtering in Fourier domain, aberration correction, and numerical focusing.

### **2.3 Digital holography – Angular spectrum method[8,9]**

Numerical diffraction is the basis for digital holography and can be described by the Huygens convolution method, the Fresnel transform method, and the angular spectrum method (ASM). For our purposes we have chosen the angular spectrum method of numerical diffraction for some of its advantages which will be discussed shortly. The holographic image is numerically converted into Fourier space, the angular spectrum, which is then filtered to include only the real image peak. This filtered angular spectrum is propagated to the appropriate distance (such as to the focal plane of interest) before being reconstructed, by an inverse Fourier transform, back into real space as an array of complex numbers containing the complete amplitude and phase profile of the sample.

There are several advantages inherent to the angular spectrum method over the more commonly used Fresnel transform and Huygens convolution methods. The ASM maintains consistent pixel resolution, has no minimum reconstruction distance, it lends itself to easy filtering and compensation of noise and aberration, and has increased computational efficiency. Once the angular spectrum is calculated at  $z = 0$  by a Fourier transform of the optical field, the field at any other  $z$ -plane can be calculated by propagation in  $z$  followed by just one more Fourier transform. The Fresnel and Huygens convolution methods require two or three Fourier transforms for each value of  $z$ .

The theory behind digital holography is well understood and characterized for the ASM. Suppose  $E_0(x_0, y_0)$  represents the two-dimensional input optical field at the hologram plane (the CCD intensity image). Then, the input angular spectrum at this plane is given by the Fourier transform,

$$A_0(k_x, k_y) = F\{E_0\} = \frac{1}{2\pi} \iint dx_0 dy_0 E_0(x_0, y_0) \exp[-i(k_x x_0 + k_y y_0)] \quad (2.1)$$

where  $k_x$  and  $k_y$  are the spatial frequency components and  $k = 2\pi / \lambda$ . According to the principle of Fourier transform, this spectrum represents the various plane-wave components that comprise the input hologram. The input field, of course, can be immediately retrieved by an inverse Fourier transform of the angular spectrum at this plane,

$$E_0(x_0, y_0) = F^{-1}\{A_0\} = \frac{1}{2\pi} \iint dk_x dk_y A_0(k_x, k_y) \exp[i(k_x x_0 + k_y y_0)]. \quad (2.2)$$

The exponential,  $\exp[i(k_x x_0 + k_y y_0)]$ , is simply the projection of a plane-wave propagating along the vector,  $\mathbf{k} = (k_x, k_y, k_z)$  on the plane,  $(x_0, y_0)$  where,

$$k_z = \sqrt{k^2 - k_x^2 - k_y^2}. \quad (2.3)$$

So the entire input field,  $E_0$ , is a projection of many plane-wave components propagating in various directions,  $\mathbf{k}$ , with complex amplitudes given by the spectrum,  $A_0(k_x, k_y)$ . If the field is propagated by a distance,  $z$ , then each plane-wave component acquires the phase factor,  $\exp(ik_z z)$ . The output field then becomes,

$$E(x, y; z) = \frac{1}{2\pi} \iint dk_x dk_y A_0(k_x, k_y) \exp[i(k_x x + k_y y + k_z z)] \quad (2.4)$$

which is simply the inverse Fourier transform of  $A_0(k_x, k_y) \exp(ik_z z)$ .

## 2.4 Conclusion

We can make several observations from the formulation of the ASM. First, we note here that the square root factor from eq.(2.3) requires that  $k_x^2 + k_y^2 \leq k^2$  which means the diffraction imposes a low-pass filter on input spatial frequencies such that input structures finer than the wavelength will not propagate to far-field probes. Secondly, the description above is based on the fundamental properties of the Fourier transform without the need to impose boundary conditions. In addition, the diffraction is constructed from well-behaved plane waves where other methods are based on spherical waves which inherently require singularities at the point sources. The Fresnel transform method also requires the approximation factor,  $r \approx z$ , where the ASM does not. These advantages have important consequences when the integrals are discretized for numerical diffraction as described in [9].

The ASM method lends itself to easy filtering of unwanted noise and phase aberration as well. The angular spectrum filter can be easily and immediately adjusted in shape or size to avoid spurious noise from the direct image or other unwanted optical effects. In certain situations, it is even possible to remove the direct image information from the angular spectrum by storing separate images of the reference and object beams alone and subtracting their angular contribution. This would allow for a larger region

around the image peak of the angular spectrum and conserve lateral resolution. Geometrical wavefront aberration, such as spherical or elliptical, can be simply subtracted from any plane of interest by applying the necessary array of mathematically defined phase factors. Additionally, in some cases, general aberration can be nearly eradicated by storing and subtracting a background reference hologram. This reference hologram, just like the input hologram, contains the general phase aberration at every plane and can therefore be propagated and removed as different planes of interest are selected without the need for additional holograms. In the case of most of our experiments, this method is applicable and of high importance in the improvement of our measurable results. Figure 2.4 shows an example of this compensation.

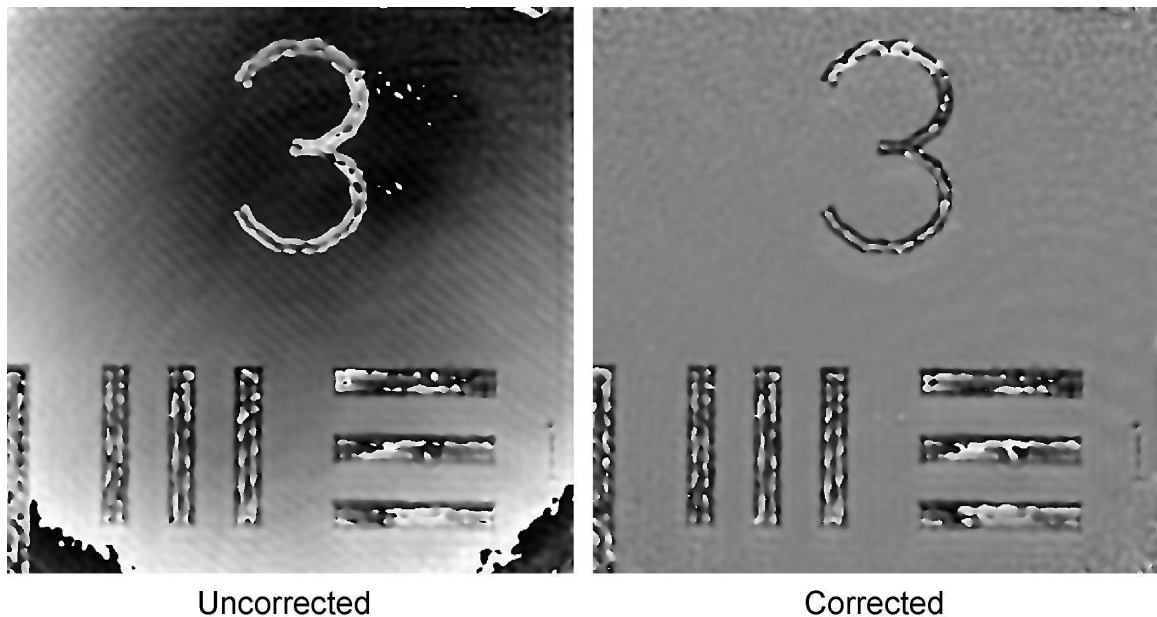


**Figure 2.4.** Phase aberration compensation. Elliptical phase aberration resulting from wavefront curvature mismatch between the reference and object beams (left) has been removed by numerical compensation (right).

## 2.5. References

1. Beuthan, J., Minet, O., Helfmann, J., Herrig, M., and Muller, G., "The spatial variation of the refractive index in biological cells," *Physics in Medicine and Biology* **41**, 369-382 (1996).
2. Cuche, E., Bevilacqua, F., and Depeursinge, C., "Digital holography for quantitative phase-contrast imaging," *Opt. Lett.* **24**, 291-293 (1999).
3. Cuche, E., Marquet, P., and Depeursinge, C., "Simultaneous amplitude-contrast and quantitative phase-contrast microscopy by numerical diffraction of Fresnel off-axis holograms," *Appl. Opt.* **38**, 6994-7001 (1999).
4. Kuhn, J., Charriere, F., Colomb, T., Cuche, E., Montfort, F., Emery, Y., Marquet, P., and Depeursinge, C., "Axial sub-nanometer accuracy in digital holographic microscopy," *Meas. Sci. Technol.* **19**, 074007 (2008).
5. Zernike, F., "Phase contrast, a new method for the microscopic observation of transparent objects," *Physica* **9**, 686-698 (1942).
6. Zernike, F., "Phase contrast, a new method for the microscopic observation of transparent objects Part II," *Physica* **9**, 974-986 (1942).
7. Allen, R.D., David, G.B., and Nomarski, G., "The Zeiss-Nomarski differential interference equipment for transmitted-light microscopy," *Z. Wiss. Mikrosk.* **69**, 193-221 (1969).
8. Kim, M.K., "Principles and techniques of digital holographic microscopy," *SPIE Reviews* **1**, 018005 (2010).
9. Kim, K., *Digital Holographic Microscopy: Principles, Techniques, and Applications* (Springer, 2011).

## **CHAPTER 3**

### **THERMAL LENSING**

In the pursuit of ultimately studying the effect of optical radiation pressure on the surface of a fluid, it was first very important to fully study and understand thermal effects of optical excitation. The use of quantitative phase imaging as the method of detection means sensitivity to both dimensional changes and optical property changes. In fact, we have taken advantage of the formation of the optically induced thermal lens described below to develop an improved method of determining the photothermal properties of transparent media. In this chapter, the thermal lens will be described and measured both spatially and temporally and the results will be used as a sensitive tool for the measurement of the absorption coefficient of the media involved.

#### **3.1 Introduction**

When a beam of incident light passes through a medium, that medium may absorb some of the energy of the beam. This absorbed energy, in turn, will cause a change in temperature of the absorbing region of the media which then will diffuse to other parts of the medium and its surroundings in some regular way described by the thermal properties of the media involved. Because the index of refraction is a temperature dependent property, the temperature gradient also causes a refractive index gradient. This

modulates variation in optical path length in these regions to light incident on the affected area of the media. This effect is referred to as thermal lensing (depicted in Figure 3.1) and has been the focus of many other studies as an indicator of the optical and thermal properties of materials [1,2].

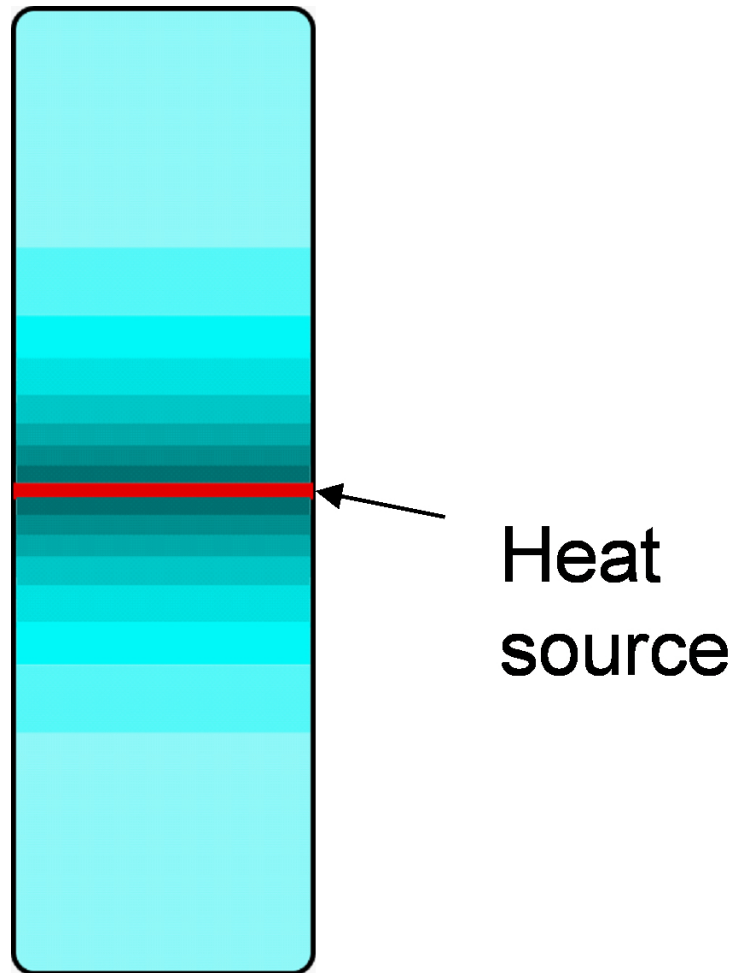


**Figure 3.1.** Cross-sectional representation of a thermal lens in a cuvette of liquid. Red line indicates a heat source while color gradient indicates the resulting temperature gradient from thermal diffusion.

Because of the change in optical path length, a resulting phase shift can be detected at a plane on the far side of the medium. Both a 2D infinite and a 3D finite model have been developed to associate this phase shift with the medium's absorption coefficient for a cw laser induced mode-mismatched dual beam set up such as that used in the current study [3,4]. The 2D infinite model has the assumption, among others, that the sample thickness is large enough that axial heat flow and sample edge effects can be ignored. This method becomes inadequate for the study of thin-film samples. The 3D finite model is able to successfully describe samples of all thicknesses; however, it lacks the convenient mathematical relation to thermo-optical properties like the 2D infinite model. For ease and freedom of setup, it is wise to choose sample parameters that are compatible with the 2D model for studies involving such conclusions.

### 3.2 Theory

To maintain validity of the 2D infinite model, several assumptions are made and experimental design should take these into account. The sample cell thickness should be short compared to the confocal distance of the beams to ensure the spot size remains relatively constant through the sample. The sample cell dimensions should be large compared with the excitation beam radius so as both radial and axial edge effects can be ignored. The sample should absorb very little power to avoid convection effects.

Finally, the temperature coefficient of refractive index,  $\frac{dn}{dT}$ , should be constant in the range of temperatures observed. With these assumptions in mind the laser induced change in temperature within the sample can be described. Using expressions for the

heat generated in a sample by a Gaussian excitation beam and the corresponding solution to the heat transfer equation, ref. [3] has derived the following relation,

$$\Delta T(r,t) = \frac{2P\alpha}{\pi c \rho w^2} \int_0^t \frac{1}{1+2t'/\tau} \exp\left(-\frac{2r^2/w^2}{1+2t'/\tau}\right) dt' \quad (3.1)$$

where  $r$  is the radial distance from the beam axis,  $t$  is the time of exposure to the excitation beam,  $P$  is the total excitation beam power at the sample,  $\alpha$ ,  $c$ , and  $\rho$  are the absorption coefficient, specific heat, and density of the sample, respectively, and  $w$  is the excitation beam radius in the sample. The characteristic thermal time constant,  $\tau$ , is given by  $\tau = \frac{w^2 c \rho}{4\kappa}$  with thermal conductivity,  $\kappa$ . The resulting refractive index gradient can be described by,

$$n(r,t) = n_0 + \frac{dn}{dT} \Delta T(r,t) \quad (3.2)$$

where  $n_0$  is the index of refraction at the starting temperature of the sample. This leads directly to phase shift described by,

$$\phi = \frac{2\pi}{\lambda} l [n(r,t) - n(0,t)] = \frac{2\pi}{\lambda} l \frac{dn}{dT} [\Delta T(r,t) - \Delta T(0,t)] \quad (3.3)$$

where  $\lambda$  is the wavelength of the probe beam and  $l$  is the thickness of the sample.

Substituting Eq. (3.1) into Eq. (3.3), the phase shift can be rewritten as,

$$\phi = \theta \int_0^t \frac{1}{1+2t'/\tau} \left[ 1 - \exp\left(-\frac{2r^2/w^2}{1+2t'/\tau}\right) \right] \frac{dt'}{\tau} \quad (3.4)$$

where,

$$\theta = -\frac{P\alpha l(dn/dT)}{\kappa\lambda}. \quad (3.5)$$

### 3.3 Experiments

Previous experimental methods have been developed to approximate the phase shift described above and have been used to measure very low absorption coefficients of materials with good agreement to expected values [1,2]. These methods detect the intensity, with and without an induced thermal lens present in the media, through a pinhole at a distance several meters away from the sample. This difference in intensity is used, through further mathematical approximation and fitting, to determine the change in the wavefront of the incident beam and, therefore, the phase shift resulting from the thermal lens [1-5]. While this is a sensitive photothermal spectroscopy method [6], this is not a direct measure of the resultant phase shift and gives rise to additional error as discussed in [4].

Since digital holography is a phase imaging method [7,8], we can measure this phase shift without further approximations in a process similar to photothermal interferometry [9]. In addition, there is no necessary minimum distance from the thermal lens to the detector plane when measuring by our method. In the studies that follow, we will show that the thermal lens behaves as predicted by the 2D infinite model both spatially and temporally. It will also be shown that our method is an excellent tool for the application of photothermal property measurement.

### 3.3.1 Measurement application using high-power excitation

It was the goal of this study to image the induced thermal lens directly and accurately and to use this compact, fast, and robust method to determine the absorption coefficients of transparent materials far below the detection level of standard spectrometers and with improved accuracy and precision over traditional photothermal spectroscopy methods.

Figure 3.2 shows a diagram of the experimental apparatus. A Mach-Zehnder interferometer is used to create the hologram of the sample using low power ( $\sim 2.5\text{mW}$ ) 633-nm laser light. The imaging beams (from a single source) are delivered by a 50:50 split fiber-optic cable (reference/probe beams), which are then collimated and passed through polarizers upon entering the system. The polarizers can be adjusted to aid in beam level balancing. The two beams then pass through matched microscope objectives before being superposed with one another by the beam combiner, differing only in that the probe beam path includes the transparent sample as shown. The resulting hologram is recorded by a digital CCD camera placed atop the setup and passed into our LabVIEW personal computer platform for amplitude and phase reconstruction based on the angular spectrum method [10].

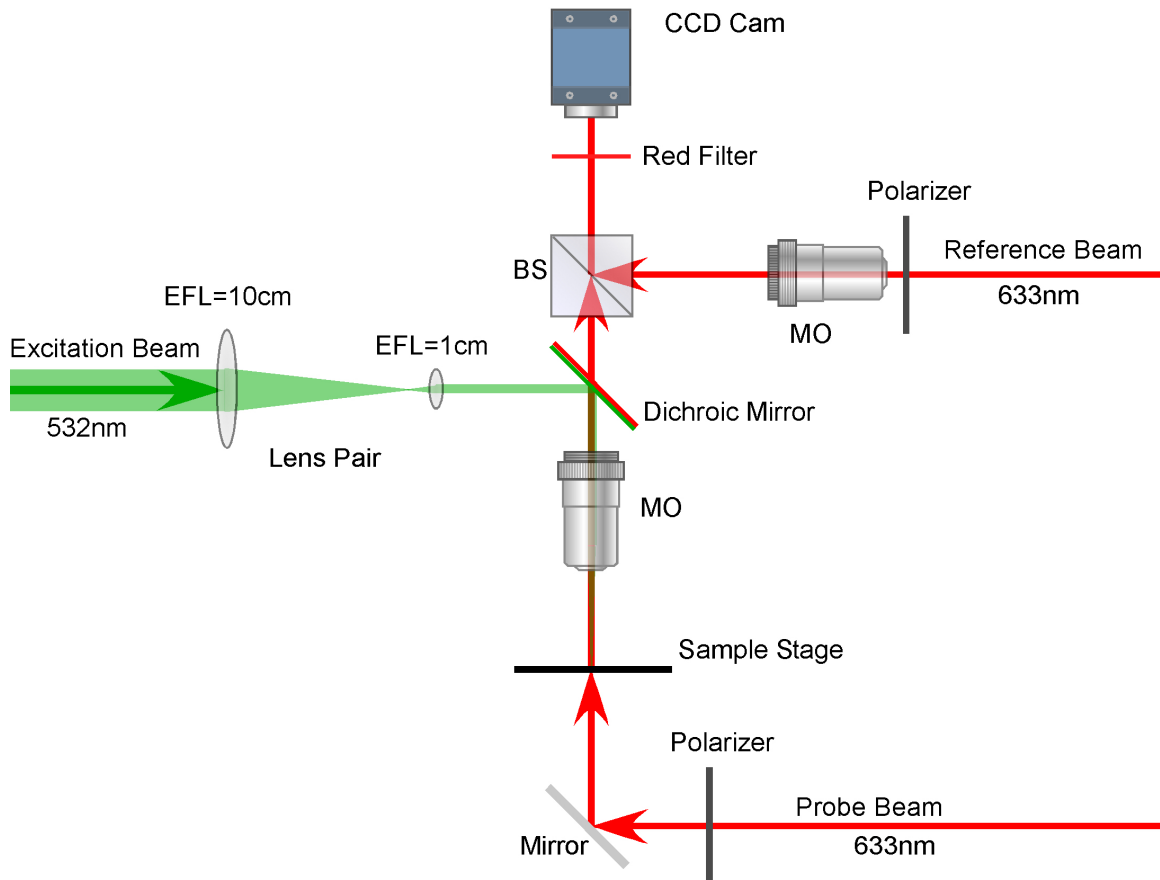


**Figure 3.2.** Experimental apparatus. The excitation beam (green) is focused downward through the sample by the probe-shared microscope objective (MO). The probe beam (red) is the object arm of the Mach-Zehnder interferometer and passes upward through the sample, combines with the reference beam, and creates the hologram captured by the CCD camera.

A high powered 532-nm cw laser beam is delivered to the integrated optical excitation arm from a fiber optic cable and collimation arrangement. The beam is then passed through a 10:1 focal length lens pair to create a much reduced collimated beam radius. A dichroic mirror reflects this excitation beam down toward the sample while allowing the probe beam to transmit up toward the CCD camera. The excitation beam

passes through the shared microscope objective which focuses the already thin beam through the sample area. The microscope objectives are chosen to have long effective focal lengths to aid in meeting the requirements of the 2D infinite model described above. A removable red bandpass filter is placed just in front of the CCD camera to filter any 532 excitation light leaking through the dichroic mirror. This “leaky” light, however, can be used to find the excitation beam radius and spot location as well as its waist along the beam axis by temporarily removing the red filter. The excitation beam radius,  $w$ , is defined as the radius at which our Gaussian beam intensity reduces to  $e^{-2}$  of its maximum value. With the red filter in place, a hologram, containing complete phase and amplitude information, is captured by the CCD camera and processed by our software routines to reconstruct the phase image in real time both with and without excitation.

The sample consists of a pure liquid in a standard glass cuvette of cross-sectional area, 5 mm by 10 mm, with a sealable lid. This sample is then placed on the sample stage on its side oriented with a 5 mm path length. While viewing the phase image, with the optical excitation beam on, the object stage was translated along the beam path ( $z$ -direction) until the focus of the excitation beam was centered within the sample. At this position, a well-defined phase signal, i.e. the thermal lens, was clearly observed (Figure 3.3). The faint diagonal fringing is a result of stray light interference within the setup. This can be removed through additional software filtering or by adjustment of the apparatus; however, this was not necessary at this time as the aberration did not affect our current measurement goals. A cross-section through the center of this thermal lens was used to plot the profile of the phase shift as a function of radial distance from the  $z$ -axis of the excitation beam (Figure 3.4). It should be noted that, due to the time-sensitivity of

the thermal effect, attention must be given to excitation beam exposure time to ensure measurements are taken in the proper regime. All measurements for the purpose of determination of absorption coefficient, for example, were performed at exposure times greater than  $2000 \tau$  (in the present case, 30 s) to ensure steady-state regime was approached. Though the model is time-resolved and our work, soon to be discussed, demonstrates excellent temporal agreement [11], near steady-state measurements drastically reduce error due to timing of measurements.

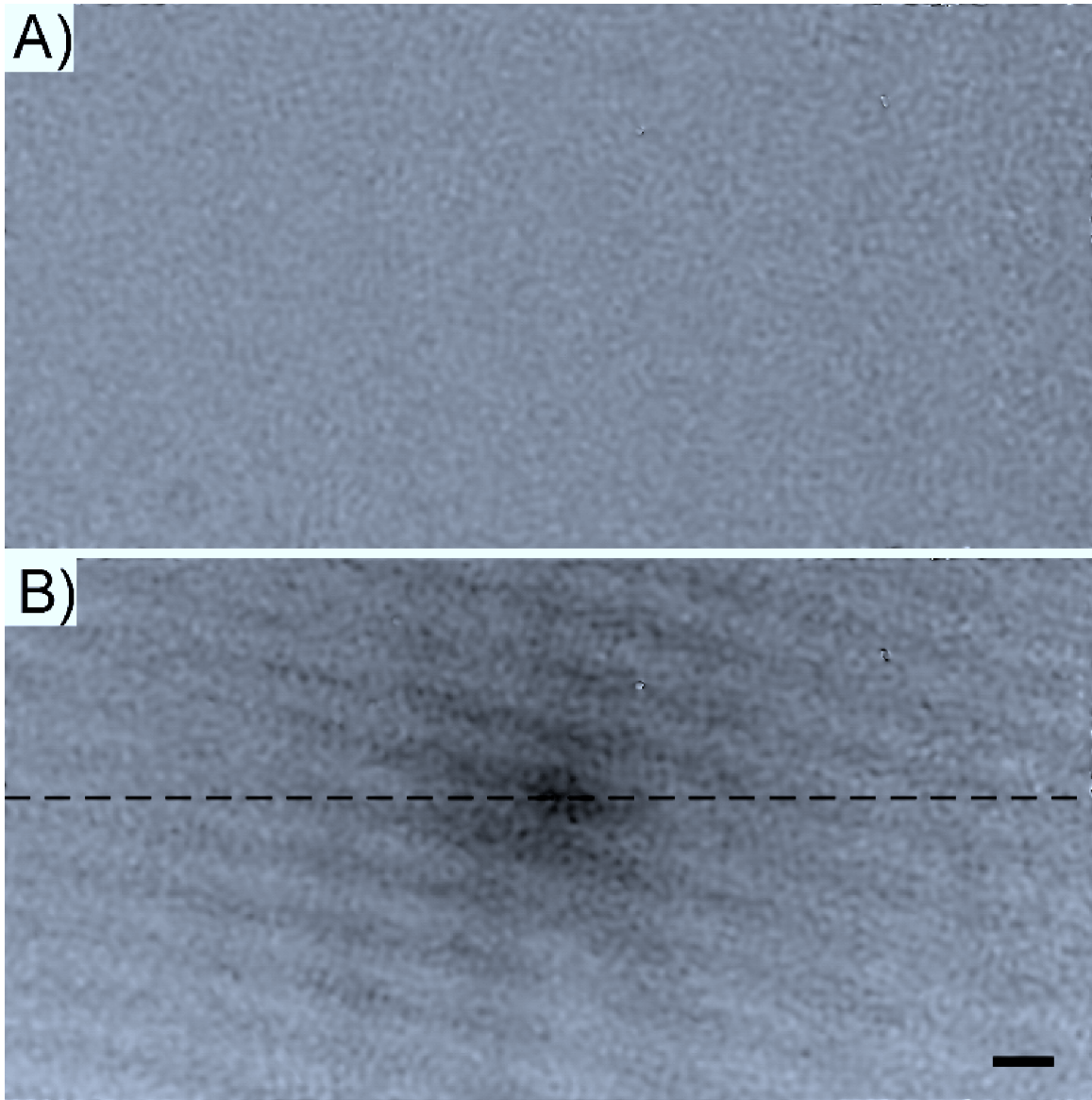


**Figure 3.3.** Phase images of methanol with, A) no excitation beam and B) 700mW excitation beam power. The phase scale of both images ranges from 0 (black) to  $2\pi$  (white) and the spatial scale bar is  $100\mu\text{m}$ . The dashed line indicates the selected cross-section used for further analysis.

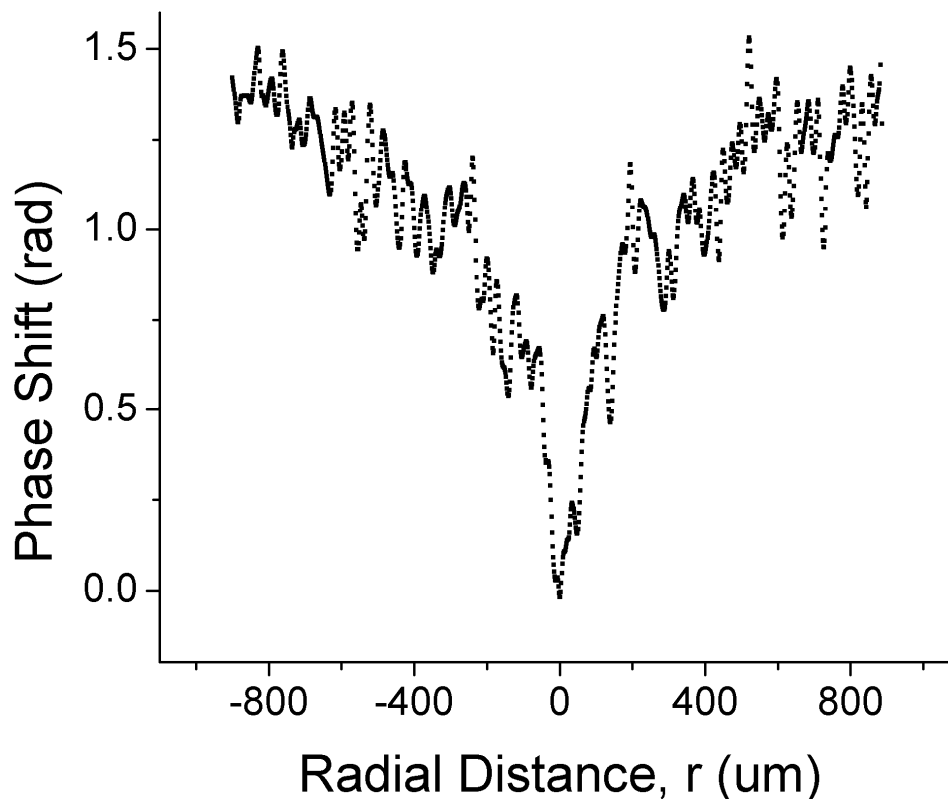


**Figure 3.4.** Cross-sectional profile of the thermal lens shown in Figure 3.3B (dashed line).

The experimental parameters and determined absorption coefficients at 532 nm,  $\alpha_{\text{exp}}$ , for methanol and ethanol are shown in table 3.1. The measured phase shift at  $t = 30$  s and  $r = 900 \mu\text{m}$  under 700mW excitation power was used to find the absorption coefficient that solved the 2D infinite model at this position and time. This determined absorption coefficient was then used to predict the entire phase profile of the thermal lens formed at varying excitation powers from 0 – 550mW. Figure 3.5 shows the raw phase data for methanol and ethanol at several of these powers and the predictions of the model with excellent fit. The displayed results are characteristic of the full range of powers tested. Note also that each plot of experimental data posted here has not been averaged,

but is the result of a single hologram. If desired, higher phase resolution can be achieved by averaging repeated phase profiles or averaging through symmetry in post-process or incorporating this into the software routine for real-time measurements; however this was not necessary for the goals of the current study.

**Table 3.1.** Experimental Parameters for methanol and ethanol.

	<b>Methanol</b>	<b>Ethanol</b>
<i>w</i>	43 $\mu\text{m}$	43 $\mu\text{m}$
<i>l</i>	5 mm	5 mm
<i>dn/dT</i>	$-3.9 \times 10^{-4} \text{ } ^\circ\text{C}^{-1}$	$-4.0 \times 10^{-4} \text{ } ^\circ\text{C}^{-1}$
<i><math>\kappa</math></i>	.202 W/m/ $^\circ\text{C}$	.167 W/m/ $^\circ\text{C}$
<i><math>\lambda</math></i>	633 nm	633 nm
<i>P</i>	0-550 mW	0-550 mW
<i><math>\tau</math></i>	4.7 ms	5.7 ms
<i>t</i>	30 s	30 s
<i><math>\alpha_{\text{exp}}</math></i>	$(3.6 \pm .3) \times 10^{-4} \text{ cm}^{-1}$	$(2.4 \pm .2) \times 10^{-4} \text{ cm}^{-1}$

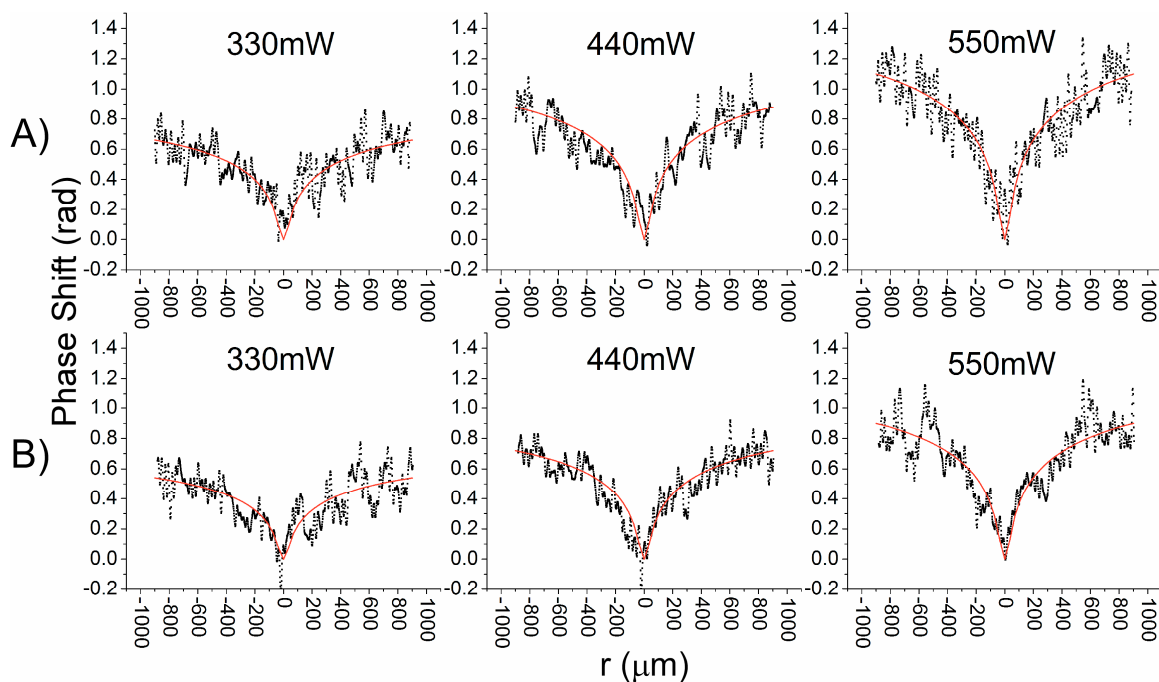


**Figure 3.5.** Experimental data (scatter plots) and model predictions (solid lines) at 330mW, 440mW, and 550mW excitation powers for both A) methanol and B) ethanol.

Methanol and ethanol were chosen for this study due to their immediate availability, ease of finding the necessary photothermal parameters, and the availability of results from previous experimental methods yielding absorption coefficients for comparison. We have measured absorption coefficients of  $(3.6 \pm 0.3) \times 10^{-4} \text{ cm}^{-1}$  and  $(2.4 \pm 0.2) \times 10^{-4} \text{ cm}^{-1}$  for methanol and ethanol, respectively. Previously, these values had been measured using the traditional “pinhole” method mentioned above as  $(5.9 \pm 0.5) \times 10^{-4} \text{ cm}^{-1}$  and  $(6.8 \pm 0.5) \times 10^{-4} \text{ cm}^{-1}$  for methanol and ethanol, respectively [2]. We have measured the values with improved precision, but what is more noteworthy is the difference in relative absorption coefficient between these two liquids. By imaging the

phase profiles directly with digital holography, this relation is straightforward and unmistakable suggesting much improved accuracy over the traditional method.

As mentioned earlier, there was some aberration (fringing in Figure 3.3) in the phase images which did not interfere with the purpose of the preceding experiments. This was explored before moving on to successive experiments and was corrected by slight adjustment to the imaging beam path, thus eliminating some arbitrary reflection from the structures of the apparatus. An example of the improved result is displayed in Figure 3.6.

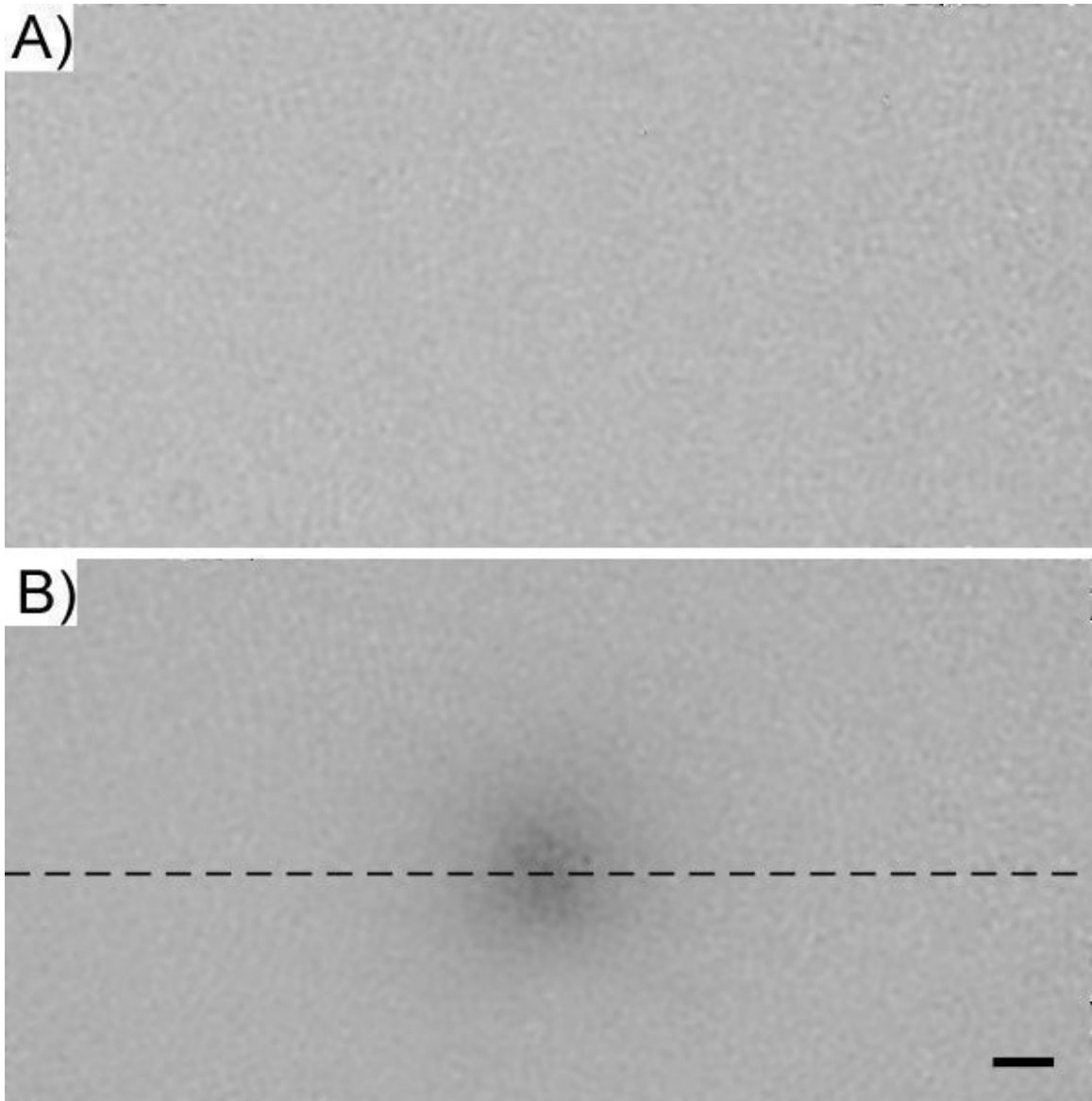


**Figure 3.6.** Improved phase images of a sample, A) with no excitation and B) with optical excitation. The phase scale of both images ranges from 0 (black) to  $2\pi$  (white) and the spatial scale bar is  $100\mu\text{m}$ . The dashed line indicates the selected cross-section used for further analysis.

### 3.3.2 Thermal lens time-resolution [11]

The absorption coefficient of methanol was determined in our previous work as indicated above. This value and the other experimental parameters for methanol are listed in table 3.2. The data from several time steps during the excitation event are displayed in Figure 3.7 as scatter plots with the model predictions superposed as solid line plots. The camera speed here was 20 frames/sec, so, the first observable frame could have occurred anywhere between 0 and 50 ms and was approximated from the series fit to be 25 ms. Subsequent captured frames occurred at 50 ms intervals, as indicated. There is clearly excellent agreement between the predicted and experimental values.

**Table 3.2.** Experimental parameters for methanol.

---

$w$	50 $\mu\text{m}$
$l$	5 mm
$dn/dT$	$-3.9 \times 10^{-4} \text{ }^\circ\text{C}^{-1}$
$\kappa$	.202 W/m/ $^\circ\text{C}$
$\lambda$	633 nm
$P$	750 mW
$\tau$	4.7 ms
$t$	0 – 1500 ms
$\alpha_{\text{exp}}$	$3.6 \times 10^{-4} \text{ cm}^{-1}$

---

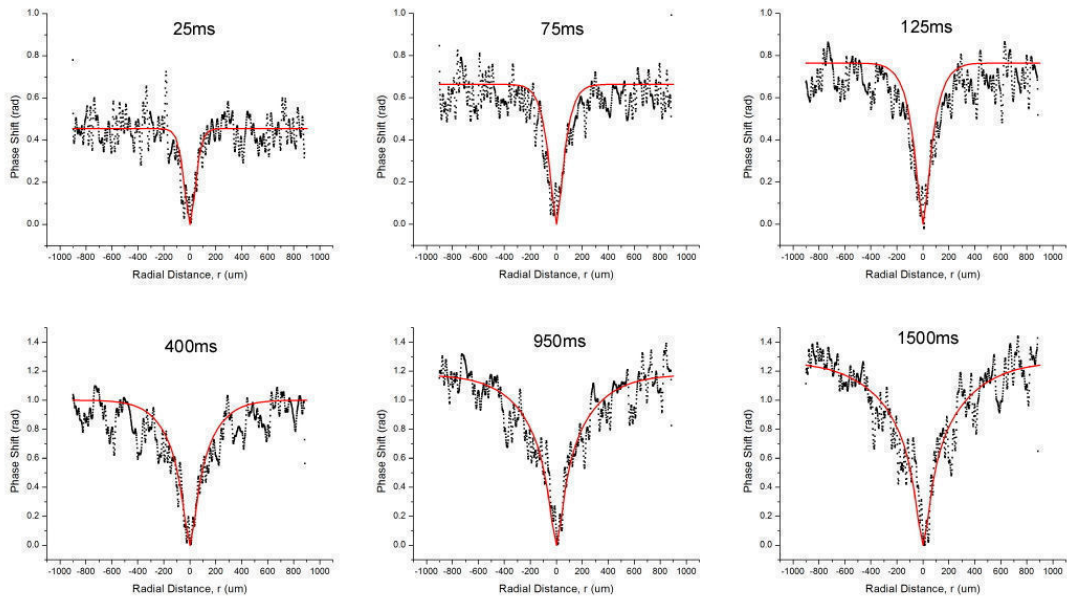


**Figure 3.7.** Experimental data (scatter plots) and 2D infinite model predictions (solid lines) at several time-resolved stages of the thermal lens excitation event in methanol.

These results are important in the experiments to follow, both in this chapter and even more importantly in the next two chapters. Knowing that the time sensitivity of the thermal lens formation is well predicted by the model allows the use of the thermal lens as a measurement tool for photothermal properties at greater speeds with little or no cost to the precision of the our method. Additionally, as we will see in the following chapters, this behavior is important in ultimately decoupling this thermal effect from overlapping optical radiation pressure effects.

### 3.3.3 Improved precision for standard-power excitation

Our previous absorption coefficient experiments have shown that, in fact, improved accuracy and precision over traditional methods is achieved through the use of

digital holography and a high-power excitation beam. In this section, we describe our use of DH-QPM with an improved apparatus and a higher precision method to map the thermal lens and measure the absorption coefficient of transparent media using low excitation power. It was the goal of this study to make full use of the data collected by an optimized system and achieve improved measurement precision with standard optical laboratory components.

Figure 3.8 shows a diagram of the improved experimental apparatus. A Mach-Zehnder interferometer is used to create the hologram of the sample using low power ( $\sim 1$  mW) 532-nm laser light. Instead of using a fiber-optic splitter to deliver separate reference and object beams into the interferometer, the single imaging beam arrives collimated at the first beam splitter of the interferometer which transmits half the beam into the reference arm and reflects half the beam into the object arm of the setup. The beams each follow a similar path, through matching singlet objective lenses (instead of compound microscope objectives), before recombining by another beam splitter with the main difference being that the object beam has passed through the sample area of the interferometer. The interference of the phase-modulated object beam with the reference beam creates the hologram. This hologram is recorded by a digital CCD camera placed atop the setup and passed into our LabVIEW personal computer platform for amplitude and phase reconstruction based on the angular spectrum method [10]

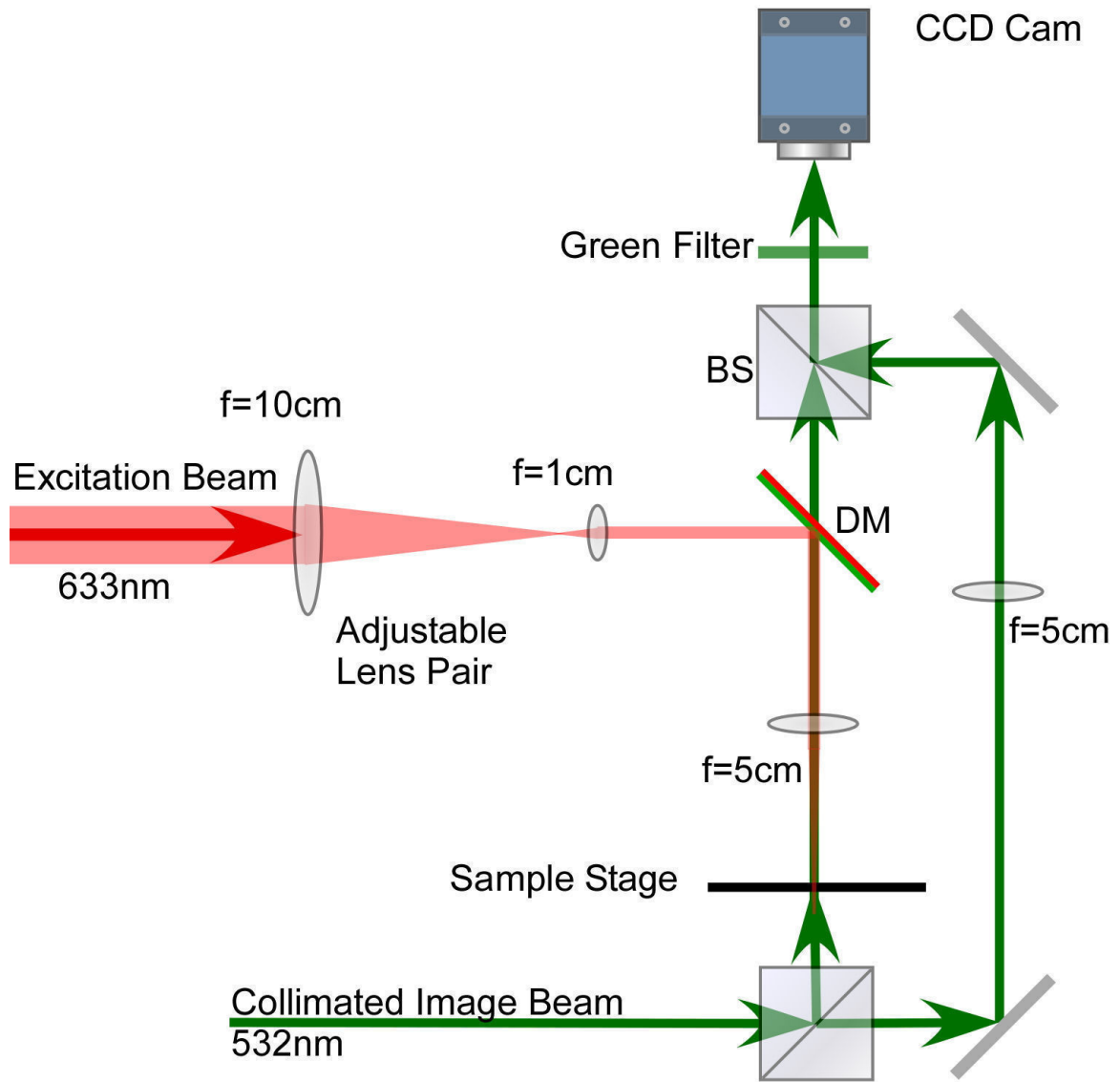


**Figure 3.8.** Experimental apparatus. The excitation beam (red) is reflected downward by the dichroic mirror (DM) through the sample by the probe-shared objective lens. The probe beam (green) is the object arm of the Mach-Zehnder interferometer and passes upward through the sample, combines with the reference beam, and creates the hologram captured by the CCD camera.

An integrated optical excitation arm delivers a 30 mW, 632.8 nm cw laser beam to the system (as opposed to the 750 mW excitation used previously). The beam is passed through a 10:1 focal length lens pair to create a much reduced beam radius. A dichroic mirror reflects this excitation beam down toward the sample while allowing the probe beam to transmit up toward the CCD camera. The excitation beam passes through the shared objective lens which focuses the already thin beam through the sample area. The objective lenses are chosen to have relatively long effective focal lengths to aid in meeting the requirements of the 2D infinite model described previously. A removable green bandpass filter is placed just in front of the CCD camera to filter out any red excitation light leaking through the dichroic mirror. This “leaky” light, however, can be used, as before, to profile the excitation beam by temporarily removing the green filter. The excitation beam radius,  $w$ , is defined as the radius at which the Gaussian beam intensity reduces to  $e^{-2}$  of its maximum. With the green filter in place, a hologram, containing complete phase and amplitude information, is captured by the CCD camera and processed by our software routines to reconstruct the phase image both with and without excitation.

The sample consists of a pure liquid in a glass cuvette 5 mm by 10 mm by 45 mm with a sealable lid. With the excitation beam profiled and adjusted to a desired radius via the excitation arm lenses, the sample is placed on the sample stage on its side oriented with a 5 mm path length. The sample stage can be adjusted in  $z$  to optimize the sample’s location for the desired beam radius. At this time, all general phase aberration, including wavefront curvature mismatch, can be easily compensated for by storing a background phase image and subtracting this from subsequent images. While viewing this baseline

phase image (Figure 3.9(a)), the optical excitation beam is turned on and a thermal lens becomes visible (Figure 3.9(b)).

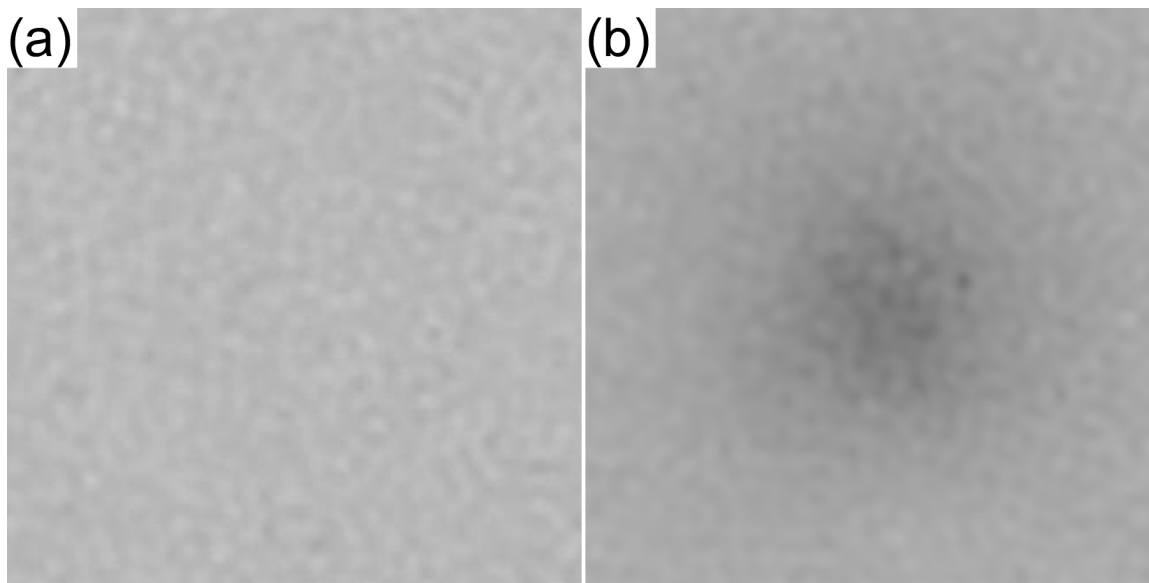


**Figure 3.9.** Example phase maps of a sample with (a) no excitation and (b) optical excitation resulting in a thermal lens (higher power excitation was used here to improve structure visibility for print). Phase shift is represented as darker for smaller values and lighter for higher values. Field of view is 1000  $\mu\text{m}$ .

Our previous work has demonstrated excellent temporal, as well as spatial, agreement with the 2D infinite model as described previously. Therefore, in the current study, we use optically triggered timing to capture the data at precisely 4000 ms after excitation begins with a shutter speed of less than 100  $\mu\text{s}$ . At this time, the rate of change of thermal lens phase signal is significantly reduced ( $\sim 0.001$  rad/s) that any error from our timing mechanism would be negligible.

Table 3.3 indicates the experimental parameters for the current study of benzyl alcohol, a transparent liquid. The absorption coefficient at 632.8 nm,  $\alpha_{exp}$ , was

determined experimentally to be  $(6.4 \pm 0.1) \times 10^{-4} \text{ cm}^{-1}$  as described herein. By taking a single cross-section through the center of the thermal lens structure in the phase map, a profile of the thermal lens phase signal vs. position is obtained as shown in Figure 3.10. Due to an improved apparatus, this raw data demonstrates an impressive precision (better than  $\pm 0.01$  rad); however, it does not adequately represent the large amount of data collected by our method.

**Table 3.3.** Experimental Parameters for Benzyl Alcohol.

Parameter	Symbol	Value
Power	$P$	30 mW
Excitation Beam Radius	$w$	70 $\mu\text{m}$
Probe Beam Wavelength	$\lambda$	532 nm
Sample Cell Path Length	$l$	5.0 mm
Excitation Duration	$t$	4.000 s
Refractive Index (20 °C) <sup>1</sup>	$n_0$	1.540
Thermal Conductivity <sup>1</sup>	$\kappa$	0.159 W/m/°C
Specific Heat Capacity <sup>1</sup>	$c$	2.02 J/g/K
Density <sup>1</sup>	$\rho$	1.044 g/ml
Thermal Time Constant	$\tau$	16.2 ms
Temp. Coefficient of RI <sup>2</sup>	$dn/dT$	$-3.5 \times 10^{-4} \text{ }^\circ\text{C}^{-1}$
Absorption Coefficient	$\alpha_{exp}$	$(6.4 \pm 0.1) \times 10^{-4} \text{ cm}^{-1}$

<sup>1</sup>CRC Handbook of Chemistry and Physics, 2008

<sup>2</sup>H. El-Kashef, G.E. Hassan, I. El-Ghazaly, App. Opt. **33**, 3540 (1994)

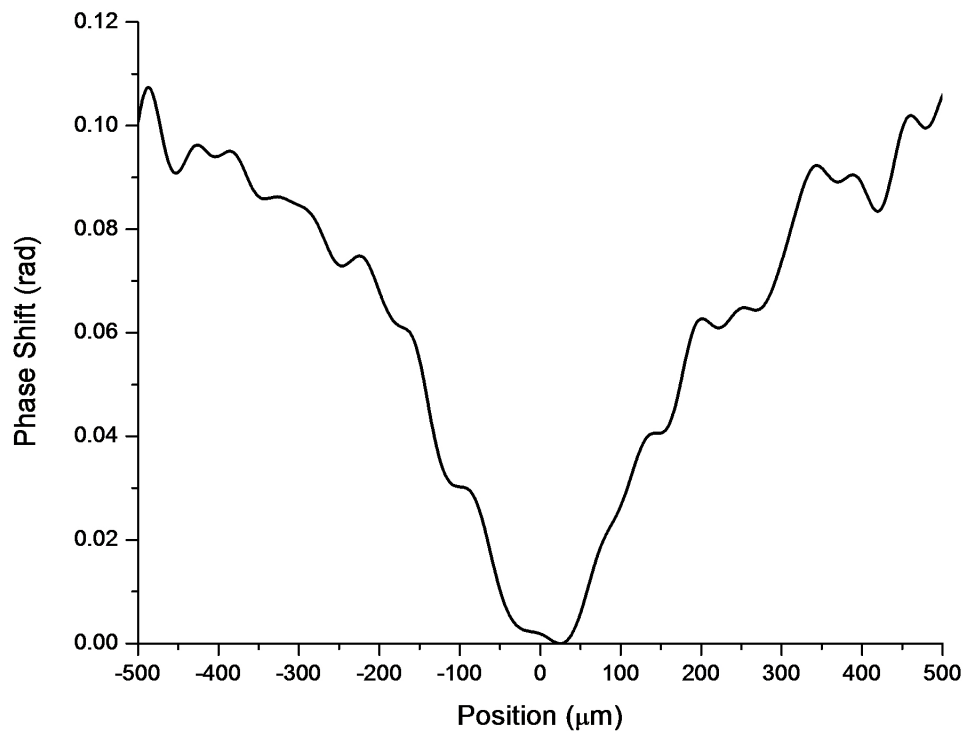


**Figure 3.10.** Single cross-section through center of the thermal lens phase structure in benzyl alcohol.

To take full advantage of the 2-dimensional array of data, we consider the radial symmetry of the structure being measured. The center of the thermal lens is determined by location of X- and Y- minima and a suitable radius is selected. A simple algorithm averages the phase data around the circumference of the circle for each radial distance to produce a 1-dimensional array of averaged phase values vs. radial distance. We elected to use 100 points around the circumference for this azimuthal averaging. This result is plotted in Figure 3.11 along with the model prediction using the experimentally determined absorption coefficient. Though the deviation is very small, we note here that there is greater deviation toward the center of the structure where the model assumes a constant excitation beam radius through the sample. This, of course, is not actually true

for a focused excitation beam and this small difference is detectable by the current method. The data taken at a sufficient distance from this artifact, in this case 170  $\mu\text{m}$  or further from the origin, never deviates more than .002 rad from the model prediction.

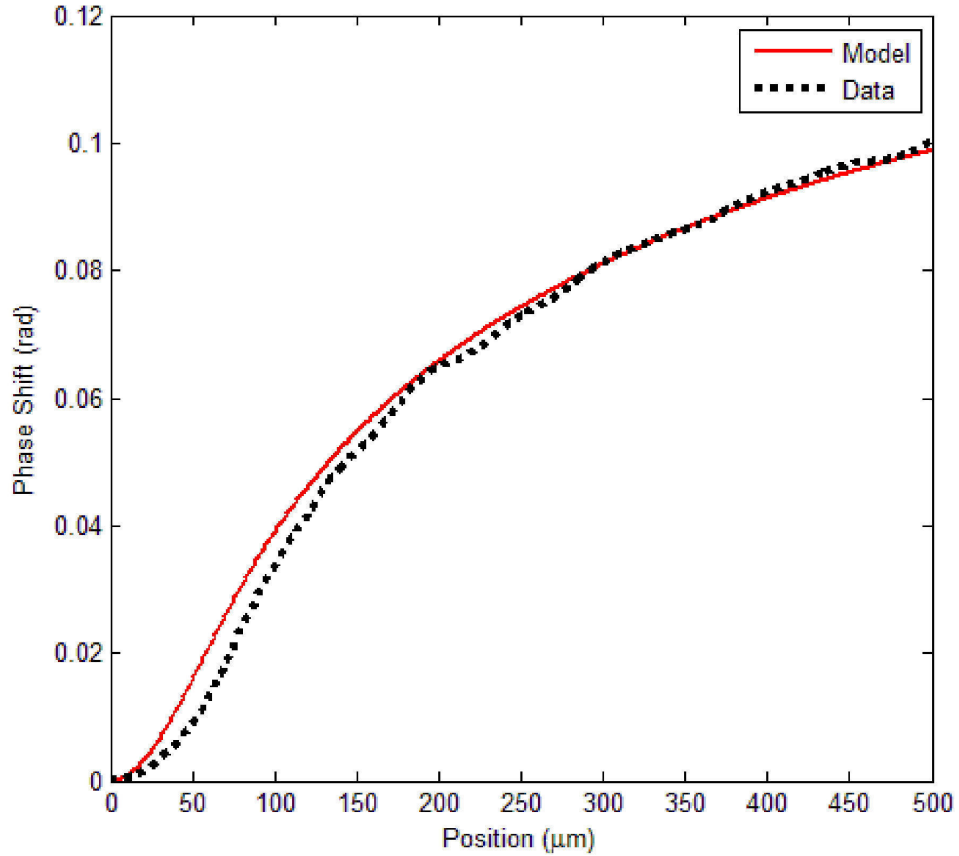


**Figure 3.11.** Phase shift vs. radial distance from center of excitation beam for experimental data (dotted) and model predictions (solid) for a thermal lens in benzyl alcohol. Shift at the origin is set to zero as a reference to the rest of the thermal lens.

We display the entire radial path here to demonstrate the strength of the relationship between the experiment and the model, however, the determination of the absorption coefficient only requires the selection of a single radial location. The most suitable selection is typically the farthest distance from the center of the thermal lens

structure that still allows complete circular averaging, but, as demonstrated, a wide range of selections are available with little or no consequence. Additionally, if the raw data is particularly noisy, the number of points around the azimuth for averaging can be increased (within the confines of the data array size).

### **3.4 Discussion and Conclusion**

Noise levels of our system were determined between each measurement by imaging the sample with no excitation beam present and taking the standard deviation of this phase profile to indicate background noise. Values from the experiments described in section 3.3.1 ranged between 0.03 and 0.17 radians with 0.12 radians being typical. While this resulted in significantly improved measurement of optical and thermal properties, we were able to achieve resolution better than an order of magnitude through improved apparatus alone (i.e. before azimuthal averaging). In the experiments from section 3.3.3, we were able to reduce background noise to between .003 and .015 radians with .01 radians being typical. In addition to the determination of absorption coefficient, the phase shift caused by a thermal lens has a direct mathematical relationship with shifts in temperature, index of refraction, and optical path length of the media as described by Eq.(3.3). As such, a direct measurement of the phase shift will yield these parameters with similar relative precision. By substituting the current typical noise level of our system (0.01 radians) into Eq.(3.3) and solving for the temperature shift difference, it is shown that the absolute difference in temperature between any two points can be determined to a precision of 0.0005 K. Similarly, the shift in refractive index is determined with  $1.7 \times 10^{-7}$  precision. Optical path difference is described by  $l(\Delta n)$

where  $l$  is our cuvette path length (5 mm) and  $\Delta n$  is the refractive index difference. Therefore, at the current typical noise level, this system determines the optical path difference with a typical 0.8 nm resolution. While these values of precision are based on the noise level of the system, the symmetry in this study permits improvement by almost another order of magnitude using the azimuthal averaging method described above.

We have successfully shown the usefulness of our method to obtain characteristic photothermal properties of pure substances. Furthermore, through careful optimization of a DH-QPM apparatus using standard optics laboratory components, we have demonstrated the measurement of photothermal properties of pure substances with very high precision. The currently described method could be immediately useful as a valuable tool in various analytical chemistry applications requiring high sensitivity [12-14]. In fact, DH-QPM is capable of a full armory of such measurement through robust adaptability to alternative compact apparatus.

In addition to its usefulness in chemical analysis, thorough testing and understanding of the thermal lens effect can be important in the observation of other optical effects. Of particular interest to us is the nanometric measurement of optical radiation pressure deformation from photon momentum exchange across a fluid interface. This effect will also result in a phase shift measurable by digital holography; however, it is very weak compared to and would be typically dominated by the thermal lens effect. For this reason, we have tested the time-resolved regime of the model by imaging at shortened time scales as described in section 3.3.2. This was done both to test the completeness of the model as well as to demonstrate that thermal effect presence is drastically reduced at very early time steps. Using this knowledge and other controllable

parameters, the next chapter will demonstrate our ability to predictably decouple these photothermal effects from the photomechanical effects of optical radiation pressure.

### 3.5 References

1. Marcano, A., Loper, C., Melikechi, N., “High sensitivity absorption measurement in water and glass samples using a mode-mismatched pump-probe lens method,” *Appl. Phys. Lett.*, **78**, 3415–3417 (2001).
2. Cabrera, H., Marcano, A., and Castellanos, Y., “Absorption coefficient of nearly transparent liquids measured using thermal lens spectrometry,” *Condensed Matter Physics*, **9**, No. 2(46), 385-389 (2006).
3. Shen, J., Lowe, R.D., and Snook, R.D., “A model for cw laser induced mode-mismatched dual-beam thermal lens spectrometry,” *Chem. Phys.*, **165**, 385 (1992).
4. Shen, J., Baesso, M.L., and Snook, R.D., “Three-dimensional model for cw laser-induced mode-mismatched dual-beam thermal lens spectrometry and time-resolved measurements of thin-film samples,” *J. Appl. Phys.*, **75**, 3738 (1994).
5. Shen, J., Soroka, A.J., and Snook, R.D., “A model for cw laser induced mode-mismatched dual-beam thermal lens spectrometry based on probe beam profile image detection,” *J. Appl. Phys.*, **78**, 700 (1995).
6. Bialkowski, S.E., *Photothermal Spectroscopy Methods for Chemical Analysis*, (John Wiley & Sons, Inc., 1996).
7. Cuche, E., Bevilacqua, F., and Depeursinge, C., “Digital holography for quantitative phase-contrast imaging,” *Opt. Lett.*, **24**, No. 5, 291 (1999).

8. Mann, C.J., Yu, L., Lo, C.-M., and Kim, M.K., "High-resolution quantitative phase-contrast microscopy by digital holography," *Opt. Express*, **13**, 8693 (2005).
9. Woodruff, S.D. and Yeung, E.S., "Refractive Index and Absorption Detector for Liquid Chromatography Based on Fabry-Perot Interferometry," *Anal. Chem.*, **54**, 7 (1982).
10. Yu, L. and Kim, M.K., "Wavelength-scanning digital interference holography for tomographic 3D imaging using the angular spectrum method," *Opt. Lett.* **30**, 2092 (2005).
11. Clark, D.C and Kim, M.K., "Nanometric measurement of optical pressure deformation of fluid interface by digital holography," *Proc. SPIE*, **7908**, 79080T (2011).
12. Pegau, W.S., Gray, D., and Zaneveld, J.R.V., "Absorption and attenuation of visible and near-infrared light in water: dependence on temperature and salinity," *Appl. Opt.*, **36**(24), 6035 (1997).
13. Babin, M., Stramski, D., Ferrari, G.M., Claustre, H., Bricaud, A., Obolensky, G., and Hoepffner, N., "Variations in the light absorption coefficients of phytoplankton, nonalgal particles, and dissolved organic matter in coastal waters around Europe," *J. Geophys. Res.*, **108**(C7), 3211 (2003).
14. Colcombe, S.M., Lowe, R. D., Snook, R.D., "Thermal lens investigation of the temperature dependence of the refractive index of aqueous electrolyte solutions," *Anal. Chim. Acta*, **356**, 277 (1997).

## **CHAPTER 4**

### **CONTINUOUS WAVE OPTICAL RADIATION PRESSURE**

The ability of digital holographic quantitative phase imaging to not only measure optical thickness with nano- and even subnanometric precision, but also to measure wavefront contours with similar lateral resolution to the CCD camera lends itself particularly well to the observation and measurement of the very weak optical radiation pressure effect on soft matter. Having described the well-behaved spatiotemporal nature of the more prominent thermal lensing effect in the experiments of the previous chapter, it was merely an academic problem to model the combined phase contributions of both the photothermal and photomechanical properties of light interaction with fluid interfaces provided the assumption that the latter takes place on a negligibly shorter time scale is true.

In this chapter, we will derive a combined model for these two effects and provide sound reasoning for the assumption of the important difference in time scale. We will then demonstrate a computer simulation showing the expected results and feasibility of a particularly favorable fluid interface. Next, we will describe the construction of the apparatus and the development of the experiments capable of demonstrating the modeled phenomenon. Our successful comparison between the experimental results and those

predicted by our combined model demonstrate another important step towards the complete decoupling of the photothermal and optical pressure effects on fluid media.

#### **4.1 Introduction**

Measurement of optical radiation pressure effects can be a very useful tool in soft matter physics for the efficient characterization of fluid interfaces and membranes. Although it is one of the most noninvasive methods, very little work has been done in this area due to the difficulty in observing these effects. Surface deformation on a fluid interface by optical radiation pressure using a continuous wave laser source is typically very weak. The output power of these lasers, even when focused tightly on the surface, is often insufficient to overcome the surface tensions of most fluid interfaces enough to form readily observable deformations. For this reason, pulse laser sources are often used to amplify laser intensity and, therefore, the resulting deformation to a more easily observable level [1]. Alternatively, standard liquids have been replaced with well-engineered temperature sensitive phase-separating microemulsions which will form a fluid-fluid interface with exceptionally reduced surface tension near a critical temperature [2,3]. The method often used to sense these deformations is far-field diffraction. The bent surface of a fluid acts as a lens and the profile of the exiting laser beam [1-3], or separate probing laser beam [4], can be scanned in an attempt to deduce the shape and size of the deformation.

It was our intent to use the method of digital holographic microscopy to image such deformations with nanometric precision and length scales. The quantitative phase analysis inherent to digital holography [5-8] yields an imaging method which can observe

very slight surface deformations of standard fluid-fluid interfaces by true continuous wave optical radiation effects. The stable nature of the cw laser is preferred to a pulse laser, in the present case, for improved static surface deformation. The freedom to choose from a potentially broad selection of fluids is advantageous as the optical properties will be preferably well-known making conversion of the optical phase images to real physical deformations quite straightforward. The relationship between surface deformation by known optical forces and other important surface properties, such as surface tension and viscosity, has previously been derived [9, 10].

We have found that many studies on optical radiation pressure dismiss thermal effects simply due to the transparent nature of the media under study. In fact, even transparent media can have a thermal effect which quickly becomes far dominant to the effect of optical radiation pressure. For this reason, it was our intent to study and understand these effects as a necessary step in our work on optical radiation pressure as previously described.

In summary, when a beam of incident light passes through transparent media that media may absorb some of the energy of the beam causing a rise in temperature of the local region of the beam. This produces a temperature diffusion gradient mathematically described by the thermal properties of the media involved. Because the index of refraction is a temperature dependent property, the temperature gradient also defines a refractive index gradient. This causes a change in the optical thickness of these regions to light incident on the affected area of the media. This effect is referred to as thermal lensing and has been the focus of many other studies as an indicator of the optical and thermal properties of materials [11, 12].

If a thermal lens is present during the course of an optical radiation pressure study, any far-field diffraction observed is actually the result of the superposition of the two lens effects. Our use of digital holography as an imaging method has proven to be a valuable indicator of both thermal and optical effects. With our continued attention to thermal lensing, it is our goal to decouple these effects so that optical radiation pressure deformations may be easily observed. As will be discussed in detail below, these deformations will always result in an increased optical path length (positive phase shift) within the structure. Meanwhile, the thermal lensing effect results in a shortened optical path length (negative shift). Additionally, these two effects differ greatly in the time scale with which they occur as will be discussed below.

It has been the goal of our ongoing research to make use of these differences to produce quantitative phase analyses of the two effects with excellent accuracy and precision using a Mach-Zehnder configured digital holographic microscope. The deformation can therefore be measured with nanometric precision enabling the possibility of calculating surface properties using non-invasive “light-only” manipulation and imaging techniques. This is ideal for both current work on fluid interfaces and future application to biological cell membranes.

## **4.2 Theory**

For thermal modeling, experimental dimensions were chosen as necessary for the application of the 2D infinite model which shall be described first. To maintain validity of this model, several assumptions are made that govern experimental design. The sample cell thickness should be short compared to the confocal distance of the beams to

ensure the spot size remains relatively constant through the sample. The sample cell dimensions should be large compared with the excitation beam radius so as both radial and axial edge effects can be ignored. The sample should absorb very little power to avoid convection effects. Finally, the temperature coefficient of refractive index,  $\frac{dn}{dT}$ , should be constant in the range of temperatures observed. With these assumptions in mind, the laser induced change in temperature within the sample can be described by [13],

$$\Delta T(r, t) = \frac{2P\alpha}{\pi C\rho w^2} \int_0^t \frac{1}{1+2t'/\tau} \exp\left(-\frac{2r^2/w^2}{1+2t'/\tau}\right) dt' \quad (4.1)$$

where  $r$  is the radial distance from the beam axis,  $t$  is the time of exposure to the excitation beam,  $P$  is the total excitation beam power at the sample,  $\alpha$ ,  $C$ , and  $\rho$  are the absorption coefficient, specific heat, and density of the sample, respectively, and  $w$  is the excitation beam radius in the sample. The characteristic thermal time constant,  $\tau$ , is given by

$$\tau = \frac{w^2 C \rho}{4\kappa} \quad (4.2)$$

with thermal conductivity,  $\kappa$ . The resulting refractive index gradient can be described by,

$$n(r, t) = n_0 + \frac{dn}{dT} \Delta T(r, t) \quad (4.3)$$

where  $n_0$  is the index of refraction at the starting temperature of the sample. This leads directly to phase shift due to the thermal lens described by,

$$\begin{aligned}
\phi_{TL} &= \frac{2\pi}{\lambda} l [n(r, t) - n(0, t)] \\
&= \frac{2\pi}{\lambda} l \frac{dn}{dT} [\Delta T(r, t) - \Delta T(0, t)]
\end{aligned} \tag{4.4}$$

where  $\lambda$  is the wavelength of the probe beam and  $l$  is the thickness of the sample.

Substituting Eq.(4.1) into Eq.(4.4), this phase shift can be rewritten as,

$$\phi_{TL} = -\frac{P\alpha l (dn/dT)}{\kappa\lambda} \int_0^t \frac{1}{1+2t'/\tau} \left[ 1 - \exp\left(-\frac{2r^2/w^2}{1+2t'/\tau}\right) \right] \frac{dt'}{\tau}. \tag{4.5}$$

This gives a complete time-resolved picture of the phase behavior due to the relevant thermal effect. This is the model that I have tested to show that sufficient reduction of the thermal effect can be achieved by reduction of excitation time. In addition, Eq.(4.2) shows that the thermal time constant increases with the square of the excitation beam radius, thus making this an equally valuable parameter that can easily be controlled.

Now, the deformation effect of optical radiation pressure is based on conservation of momentum across an interface as described by,

$$N \frac{n_1 h\nu}{c} \hat{z} = N \left( T \frac{n_2 h\nu}{c} - R \frac{n_1 h\nu}{c} \right) \hat{z} + \bar{p} \tag{4.6}$$

where  $n_1$  and  $n_2$  are the refractive index of the first and second media,

respectively,  $N$  represents the number of photons,  $T$  and  $R$  are the transmission and reflection coefficients, and  $\bar{p}$  is the momentum transfer to the interface. By solving this equation for the simple case of a flat interface with normal incident photons,

$$\vec{p} = \frac{2n_1}{c} \left( \frac{n_1 - n_2}{n_1 + n_2} \right) N h \nu \hat{z} \quad (4.7)$$

it becomes easy to see that the direction of momentum transfer, and therefore the deformation of the interface, will always point in the direction of the smaller refractive index material regardless of the direction of beam propagation. This is because a photon gains momentum when moving into a higher refractive index medium. This phenomenon was shown by Ashkin and Dziedzic in 1973 [1].

A relation between this exchange of momentum and the actual physical deformation will now be derived. The forces that must be overcome in order to create a surface deformation are those associated with buoyancy and surface tension (or more appropriately, interfacial tension). The force associated with interfacial tension has a direct mathematical relation to the contact angle of the deformation as follows,

$$\vec{F}_t = 2\pi w \sigma \sin \theta \hat{z} \quad (4.8)$$

with interfacial tension,  $\sigma$ , contact angle,  $\theta$ , and  $w$  is the excitation beam radius as this is expected to be the approximate radius of our induced deformation. Since our proposed deformations are of nanometric height scale, interfacial tension is by far the more dominant of the two. In fact, based on a typical deformation in the present case, the tension force is greater than 100 times that of the buoyant force as shown by,

$$F_t = 2.6 \text{ nN}$$

$$F_{buoy} = (\rho_b - \rho_w) V g = 23 \text{ pN}$$

Thus, buoyancy can be ignored. The tension force, then, must be balanced with the force associated with the incident excitation beam,

$$\bar{F}_{opt} = \frac{2n_1}{c} \left( \frac{n_1 - n_2}{n_1 + n_2} \right) P \hat{z} \quad (4.9)$$

where  $P$  is the excitation laser power just as above. Combining Eq.'s (4.8) and (4.9) and solving for  $\theta$  we have,

$$\theta = \sin^{-1} \left( \frac{P n_1 (n_1 - n_2)}{c \pi w \sigma (n_1 + n_2)} \right). \quad (4.10)$$

Assuming a spherically growing deformation, we can use geometric relations to model the deformation height as a function of radial distance from the beam axis,

$$h(r) = h_0 + \frac{w}{\sin \theta} - \sqrt{\frac{w^2}{\sin^2 \theta} + r^2} \quad (4.11)$$

where  $h_0$  is the maximum height of deformation (at  $r=0$ ),

$$h_0 = \frac{w}{\sin \theta} \left( 1 - \sqrt{1 - \sin^2 \theta} \right). \quad (4.12)$$

The phase shift then associated with this deformation would be,

$$\phi_{OP} = h (n_1 - n_2) \frac{2\pi}{\lambda}. \quad (4.13)$$

To get an expression for the time scale of the optically induced deformation, first consider the net force as a function of the growing contact angle,  $\theta'$ .

$$F_{net}(\theta') = F_t(\theta') + F_{opt}. \quad (4.14)$$

Now, using the integral definition of average to find the average net force,

$$\begin{aligned}
\langle F_{net} \rangle &= \frac{1}{\theta} \int_0^\theta F_t(\theta') - F_{opt} d\theta' \\
&= \frac{1}{\theta} (F_{opt} \theta + 2\pi w \sigma (1 - \cos \theta))
\end{aligned} \tag{4.15}$$

and acceleration from the relation,

$$\langle a \rangle = \frac{\langle F \rangle}{m}. \tag{4.16}$$

The time scale for the full deformation can be approximated by,

$$t_{opt} = \sqrt{\frac{2h_0}{\langle a \rangle}} = \sqrt{\frac{2h_0 \theta m}{(F_{opt} \theta + 2\pi w \sigma (1 - \cos \theta))}}. \tag{4.17}$$

With these approximations we have developed a computer simulation to combine thermal and optical models to better predict the experimental parameters necessary to decouple the two effects. Initial simulations showed promising results for optical radiation pressure experiments. Figure 4.1 is an example simulation for benzyl alcohol and water, a promising pair of pure substances that layer with a previously measured low interfacial tension of 3.5 mN/m [15] and a time scale of 16  $\mu$ s from Eq.(4.17). We begin by showing the predicted comparison of the two effects after a 2 second exposure to 700mW excitation from a 50 $\mu$ m radius beam (Figure 4.1(A)). It is seen here that any optical pressure deformation at the interface would be completely masked by the thermal lens (TL). By reducing the exposure to only 10 ms, we see the thermal effect is substantially reduced, however, any surface deformation is still expected to be below the detection limit and still strongly overwhelmed by the TL (Figure 4.1(B)). As mentioned above, increasing the excitation beam radius has a strong effect on the thermal time constant. Therefore, in Figure 4.1(C) we have increased the beam radius to 500 $\mu$ m, but

left the exposure time at 10ms, to reduce the thermal effect while increasing the beam power to 5W to enhance the optical pressure effect. The combined model now predicts that the optical pressure effect should dominate the phase image by more than 0.1 radians. This is well above the detection limit of our current setup and would be clearly evidenced in a successful conjugate experiment.

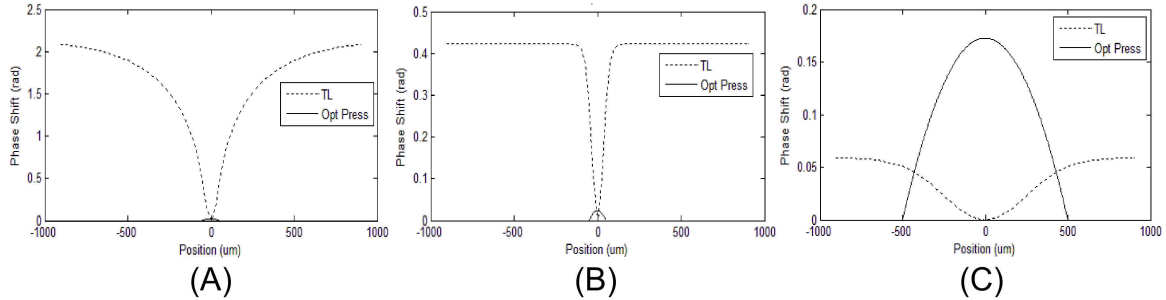


**Figure 4.1.** Model prediction for the thermal lens (TL) and optical pressure (Opt Press) effects for a sample of layered benzyl alcohol and water with an interfacial tension of 3.5 mN/m. A) 700 mW, 50  $\mu\text{m}$  beam excitation for a 2 second duration. B) Duration reduced to 10 ms. C) 5 W, 500  $\mu\text{m}$  beam excitation for 10 ms.

### 4.3 Experiments

The general apparatus and procedures for optical pressure excitation and measurement are similar to that for the thermal lens with some small modifications. The experiments described here were performed with an improved version of the interferometer used in the experiments of sections 3.3.1 and 3.3.2 (i.e. before the redesigned apparatus introduced in section 3.3.3). Figure 4.2 shows a diagram of the experimental apparatus. A Mach-Zehnder interferometer is used to create the hologram of the sample using low power ( $\sim 2.5$  mW) 633 nm laser light. The imaging beams (from a single source) are delivered by a 50:50 split fiber optic cable (reference/probe beams),

which are then collimated and passed through polarizers upon entering the system. The polarizers can be adjusted to aid in beam level balancing. The two beams then pass through matched microscope objectives before being superposed by the beam combiner, differing only in that the probe beam path includes the transparent sample area as shown. The resulting hologram is recorded by a digital CCD camera placed atop the setup and passed into our LabVIEW personal computer platform for amplitude and phase reconstruction based on the angular spectrum method [16].

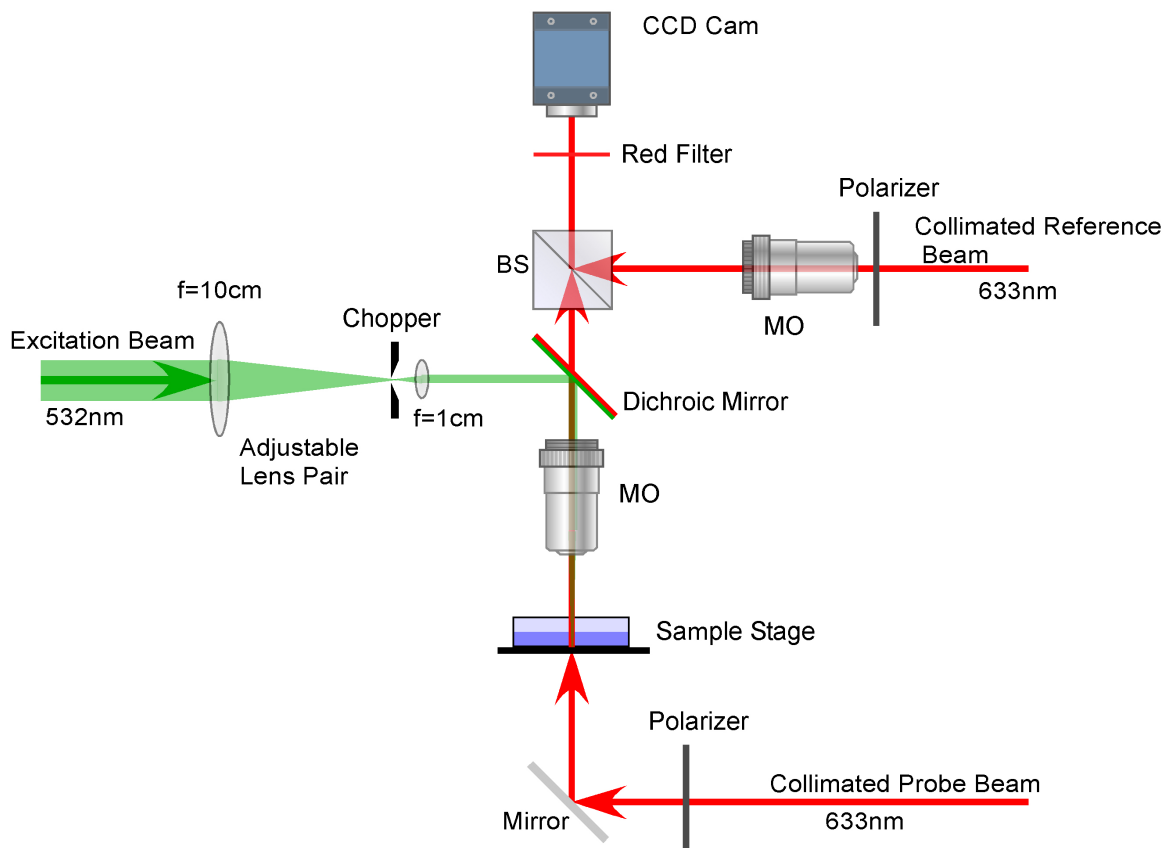


**Figure 4.2.** Experimental apparatus. The excitation beam (green) is shuttered by the electromechanical chopper and then focused downward through the sample by the probe-shared microscope objective (MO). The probe beam (red) is the object arm of the Mach-Zehnder interferometer and passes upward through the sample, combines with the reference beam, and creates the hologram captured by the CCD camera.

An integrated optical excitation arm delivers a high powered (up to 5.5 W) 532 nm cw laser beam to the system. The beam is steered directly from the source into the excitation arm in this case, instead of delivery through an optical fiber, to prevent loss of necessary power for these experiments. The collimated beam is passed through a 10:1 focal length lens pair to create a much reduced collimated beam radius. An electromechanical chopper is positioned at the focus within this lens pair to provide a fast opening shutter operation for controlled beam delivery. A dichroic mirror reflects this excitation beam down toward the sample while allowing the probe beam to transmit up toward the CCD camera. The excitation beam passes through the shared microscope objective which condenses the already thin beam through the sample area. The microscope objectives are chosen to have long effective focal lengths to aid in meeting the requirements of the 2D infinite model for thermal lensing described above. A removable red filter is placed just in front of the CCD camera to filter any 532 nm excitation light leaking through the dichroic mirror. This “leaky” light, however, can be used to find the excitation beam radius and spot location as well as its waist along the beam axis by temporarily removing the red filter. The excitation beam radius,  $w$ , is defined as the radius at which our Gaussian beam amplitude reduces to  $e^{-2}$  of its maximum value at the plane of interest. With the red filter in place, a hologram containing complete phase and amplitude information is captured by the CCD camera and processed by my LabVIEW software routines to reconstruct the phase images both with and without excitation.

### **4.3.1 Thermal behavior of benzyl alcohol**

Here we are working with benzyl alcohol, which has a very low interfacial tension when layered with water. Initial simulations shown above suggest that, using the currently described method and apparatus, it is possible to observe and measure the deformation of this interface on the order of 10's of nanometers. We have performed a time series experiment similar to that of section 3.3.2 to verify the thermal behavior of benzyl alcohol here. Figure 4.3 shows the comparison of these measurements with those predicted by our model with excellent agreement. We note that, while the layer of water produces a thermal lens, its effects are below the current detection limit at the shortened time scales of interest for cw optical radiation pressure detection.

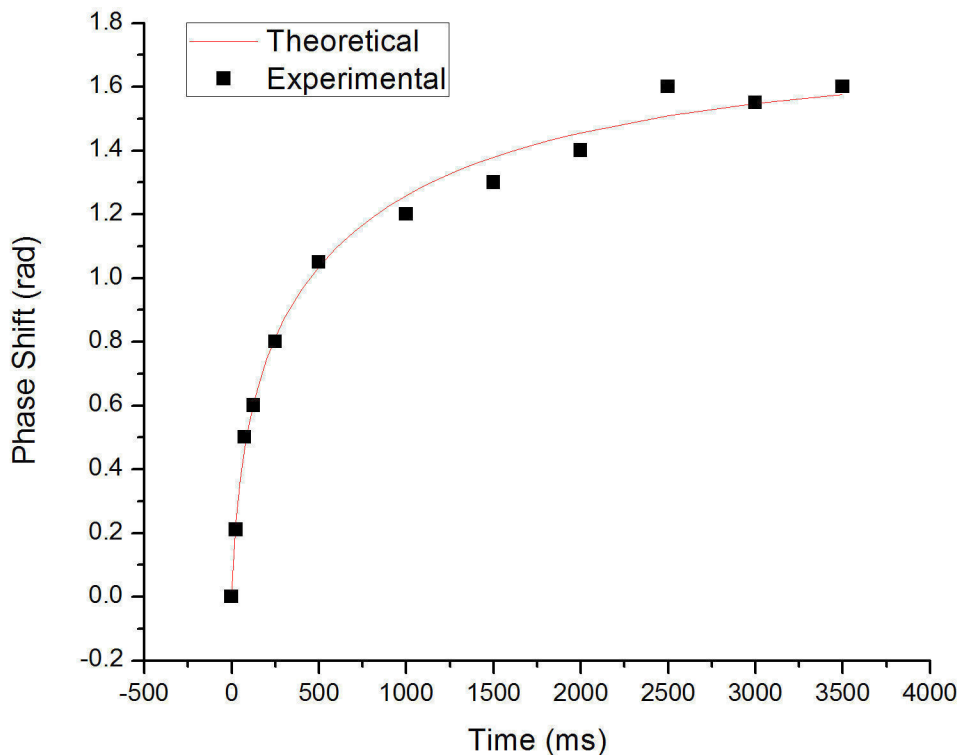


**Figure 4.3:** Time-resolved thermal lens phase shift measurements (at  $r = 900 \mu\text{m}$ ) of benzyl alcohol with model prediction (solid line).

#### 4.3.2 Detection of optical pressure effect

While significantly improved imaging time-resolution methods will be developed and introduced in the next chapter, the current method provides an adequate experimental demonstration of the predictions of the combined model. Here, water was layered on top of benzyl alcohol in a sample cell filled to the top wall (i.e. total physical path length remains constant). The experimental parameters for these liquids are listed in table 4.1. As mentioned above, these liquids form a relatively low interfacial tension of  $3.5 \text{ mN/m}$ . A  $4 \text{ W}$  excitation beam of  $500 \mu\text{m}$  radius was applied by a high speed electromechanical

shutter (full beam exposure in  $<17 \mu\text{s}$ ) while continuous imaging was acquired at 40fps (25ms/frame).

Below, the experimental captures at five time intervals are displayed and compared to our model predictions (figure 4.4). To more accurately represent the smooth contour of a surface deformation, the strict geometric theoretical bases described by Eq.(4.11) were used to define the parameters of the expected Gaussian deformation profile. The precise time of the first appearance of the structure is not directly known, but is approximated at 5 ms, based on the dataset fit to various model points, followed by the 25 ms intervals of the capture rate. The similarities to model predictions demonstrate the soundness and feasibility of the proposed method and model. Not only is there a clear change of phase shift direction as expected during the transition of effects, but the values of the measured and predicted shifts were in excellent agreement at each 25 ms time interval.

**Table 4.1.** Experimental parameters for benzyl alcohol and water layers.

Parameter	Symbol	BnOH	Water
Power	$P$		4 W
Excitation Beam Radius	$w$		500 $\mu\text{m}$
Probe Beam Wavelength	$\lambda$		633 nm
Path Length	$l$		5.0 mm
Excitation Duration	$t$		0-80 ms
Refractive Index (20 °C) <sup>1</sup>	$n_0$	1.540	1.333
Thermal Conductivity <sup>1</sup>	$\kappa$	0.159 W/m/°C	0.600 W/m/°C
Specific Heat Capacity <sup>1</sup>	$c$	2.02 J/g/°C	4.181 J/g/°C
Density <sup>1</sup>	$\rho$	1.044 g/ml	0.9971 g/ml
Thermal Time Constant	$\tau$	829 ms	434 ms
Temp. Coefficient of RI <sup>2</sup>	$dn/dT$	$-3.5 \times 10^{-4} \text{ }^\circ\text{C}^{-1}$	$-1.0 \times 10^{-4} \text{ }^\circ\text{C}^{-1}$
Absorption Coefficient	$\alpha_{exp}$	$6.4 \times 10^{-4} \text{ cm}^{-1}$	$6.0 \times 10^{-4} \text{ cm}^{-1}$

<sup>1</sup>CRC Handbook of Chemistry and Physics, 2008

<sup>2</sup>H. El-Kashef, G.E. Hassan, I. El-Ghazaly, App. Opt. **33**, 3540 (1994)

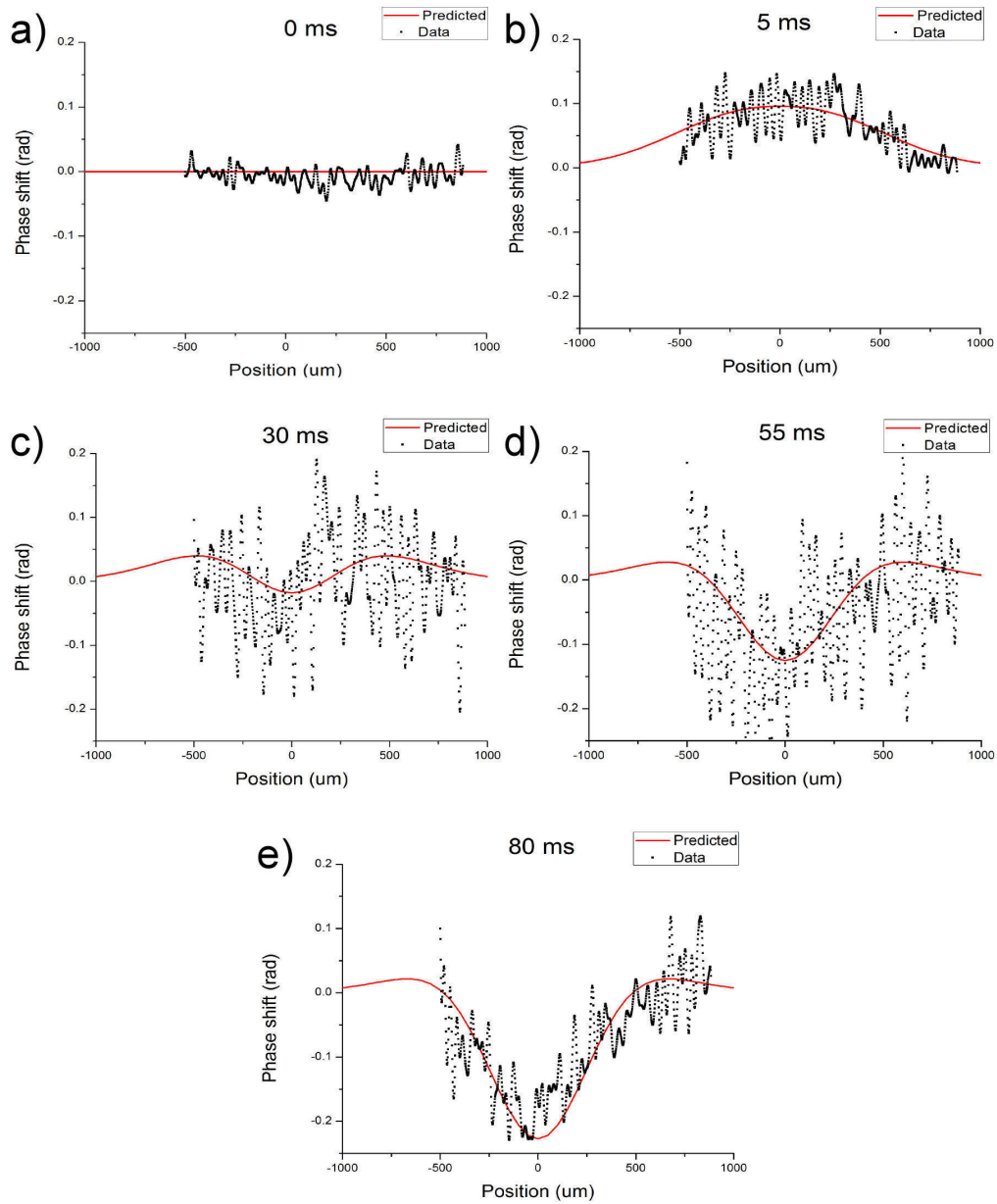


**Figure 4.4.** Phase shift data (scatter) and model predictions (solid) at 5 points in time of an excitation event: a) before excitation, b) 5 ms after excitation showing an observable optical pressure deformation before the negative thermal effect begins to dominate, and c) – e) captures at 25 ms intervals showing the growing and dominating thermal lens effect.

#### 4.4 Discussion and Conclusion

Noise levels of our system were again determined by imaging the sample with no excitation beam present and taking the standard deviation of this phase profile to indicate background noise, in this case, 0.025 rad. Though noise clearly increases during the transition of the observed effects, its level remains below 0.05 rad during the time regime of the optical radiation pressure deformation. It should be noted that phase noise has been a feature of constant improvement as our experiments proceed. As mentioned in the previous chapter, noise levels less than 10 mrad have already been achieved with an improved interferometer design which will be used in the optical radiation pressure experiments described in the next chapter.

At this point, it may be useful to summarize the success of the above experiments in imaging optical and thermal phenomenon by digital holography. Thermal lensing has been measured with such excellent spatial agreement to the existing 2D infinite model that photothermal properties of transparent media have been determined with better precision and accuracy than traditional methods. A method has been implemented to reduce the excitation duration time of the first time-series frame to between 0 and 25 ms followed by 25 ms interval frame captures with camera exposure times of about 80  $\mu$ s. This was done both to test the completeness of the model as well as to reduce the thermal effect on the media to a level that the optical pressure effect may be observed without the dominating effect of thermal lensing present. The near perfect match between the time-resolved model and our phase measurement is very promising for our future interests. The results of the above described experiments and our computer simulations suggest that

decoupling thermal and pressure effects and imaging with digital holography can prove successful for fluid-fluid interfaces.

It is expected that our optical pressure techniques can be adapted to the characterization of physical properties of biological cell membranes. The membrane-fluid interface should be very similar to the fluid-fluid interface currently under investigation. Though it is not certain which excitation source may be most advantageous for this future interest, the next chapter will demonstrate some additional advantages of a pulsed excitation source. Specifically, it will be shown that the photothermal effects can be eliminated completely from the quantitative phase analysis revealing a useful, fine-structured spatiotemporal surface response to an optical pressure impulse.

#### **4.5 References**

1. Ashkin, A. and Dziedzic, J.M., "Radiation Pressure on a Free Liquid Surface," *Phys. Rev. Lett.* **30**, 139-142 (1973).
2. Casner, A. and Delville, J.-P., "Adaptative Lensing Driven by the Radiation Pressure of a Continuous-Wave Laser Wave Upon a Near-Critical Liquid-Liquid Interface," *Opt. Lett.* **26**(18), 1418-1420 (2001).
3. Chraïbi, H., Lasseux, D., Arquis, E., Wunenburger, R., Delville, J.-P., "Simulation of an Optically Induced Asymmetric Deformation of a Liquid-Liquid Interface," *Eur. J. Mech. B/Fluids* **27**, 419-432 (2008).
4. Sakai, K., Mizuno, D., and Takagi, K., "Measurement of Liquid Surface Properties by Laser-Induced Surface Deformation Spectroscopy," *Phys. Rev. E* **63**, 046302 (2001).

5. CuChe, E., Bevilacqua, F., Depeursinge, C., "Digital holography for quantitative phase-contrast imaging," *Opt. Lett.* **24**(5), 291 (1999).
6. Kim, M. K., "Principles and techniques of digital holographic microscopy," *SPIE Reviews* **1**, 018005 (2010).
7. Kim, M., *Digital Holographic Microscopy: Principles, Techniques, and Applications* (Springer, 2011).
8. Mann, C. J., Yu, L., Lo, C.-M., and Kim, M. K., "High-resolution quantitative phase-contrast microscopy by digital holography," *Opt. Express* **13**, 8693 (2005).
9. Mitani, S., Sakai, K., "Measurement of ultralow interfacial tension with a laser interface manipulation technique," *Phys. Rev. E* **66**, 031604 (2002).
10. Yoshitake, Y., Mitani, S., Sakai, K., Takagi, K., "Measurement of high viscosity with laser induced surface deformation technique," *J. Appl. Phys.* **97**, 024901 (2005).
11. Marcano, A., Loper, C., Melikechi, N., "High sensitivity absorption measurement in water and glass samples using a mode-mismatched pump-probe lens method," *Appl. Phys. Lett.* **78**, 3415–3417 (2001).
12. Cabrera, H., Marcano, A., and Castellanos, Y., "Absorption coefficient of nearly transparent liquids measured using thermal lens spectrometry," *Condensed Matter Physics* **9**, No. 2(46), 385-389 (2006).
13. Shen, J., Lowe, R. D., and Snook, R. D., "A model for cw laser induced mode-mismatched dual-beam thermal lens spectrometry," *Chem. Phys.* **165**, 385 (1992).
14. Shen, J., Baesso, M. L., and Snook, R. D., "Three-dimensional model for cw laser-induced mode-mismatched dual-beam thermal lens spectrometry and time-resolved measurements of thin-film samples," *J. Appl. Phys.* **75**, 3738 (1994).

15. Kim, H. and Burgess, D. J., "Prediction of interfacial tension between oil mixtures and water," *J. Colloid Interface Sci.* **241**, 509-513 (2001).
16. Yu, L. and Kim, M. K., "Wavelength-scanning digital interference holography for tomographic 3D imaging using the angular spectrum method," *Opt. Lett.* **30**, 2092 (2005).

## **CHAPTER 5**

### **PULSED OPTICAL PRESSURE AND APPLICATION**

In the preceding chapters, we have discussed the development of high-precision quantitative phase analysis, spatial and temporal analysis of photothermal effects, and introduced and observed the photomechanical effects of optical radiation pressure. We will now make use of all that we have discussed thus far to produce a well-defined, high-precision picture of the surface response to an optical impulse while ensuring the absence of a thermal lens. In fact, the main content of this chapter will be the application of the time-resolved, fine-structured three-dimensional mapping of these events for the purpose of surface mechanical property measurement.

We introduce here a noncontact purely optical approach to measuring the localized surface properties of an interface within a system using a single optical pressure pulse and a time-resolved digital holographic quantitative phase imaging technique to track a propagating nanometric capillary disturbance. We demonstrate the method's ability to measure the surface energy of deionized water, methanol, and chemical monolayers formed by surfactants with good agreement to published values. The developments described in this chapter boast immediate application to static and dynamic systems and near-future applications for living biological cell membranes as will be discussed at the end of this chapter.

## 5.1 Introduction

Interfacial analysis is a valuable tool in areas of soft matter physics, chemistry, and biology. In fact, many surface energy measurement techniques have been employed for their varying degrees of improvement in accuracy, precision, or adaptability. Most of these tend to be invasive to the interface and suffer from an inability to make measurements within an intact system. Droplet methods [1], such as the popular pendant drop method [2], require a small sample to be removed from the system and tested separately, while probing methods [3], including the widely used Wilhelmy plate method [4], require a full contact probe through or on the interface of interest. Continuous wave (cw) optical manipulation techniques, including trapping [5] and radiation pressure [6], have grown popular for their noncontact nature and precise control. Optical trapping methods, however, require a tightly focused beam which may have unwanted effects on the media and often use microspheres as probes in contact with the interface. The loosely focused cw optical pressure techniques overcome some of these drawbacks, however, observation of the resulting weak deformation effect may be limited to very low surface tension applications, such as phase separating microemulsions [7], and imaging that relies on surface lensing or phase modulation, both of which are also affected by the imminent thermal effects as has been shown even for very transparent media applications [8-10].

A frequency-regulated optical pressure approach which induces capillary waves on the surface of interest has been shown to provide a good measure of surface tension [11]. The method makes use of a characteristic frequency which is related to the surface tension of the interface. This frequency scanning, however, requires the repeated

excitation of the sample and, as mentioned in the cited reference, is limited by the build-up of thermal effects.

The approach that we introduce here makes use of the dependence of the capillary wave velocity on the surface energy of the interface. We induce a capillary wave with a single laser pulse and the propagating wavefront of only a few nanometers in amplitude is easily tracked by our time-resolved digital holographic quantitative phase microscopy (DH-QPM) imaging apparatus (figure 5.1). The result is a complete spatiotemporal mapping of the surface response to a purely optical impulse (figure 5.2 and 5.3). Furthermore, due to the axial symmetry of the disturbance, an azimuthal average is used to improve image and tracking precision [10]. The short (5 ns) single pulse does not produce a measurable thermal effect compared to the physical deformation and there is no further excitation in our proposed process.

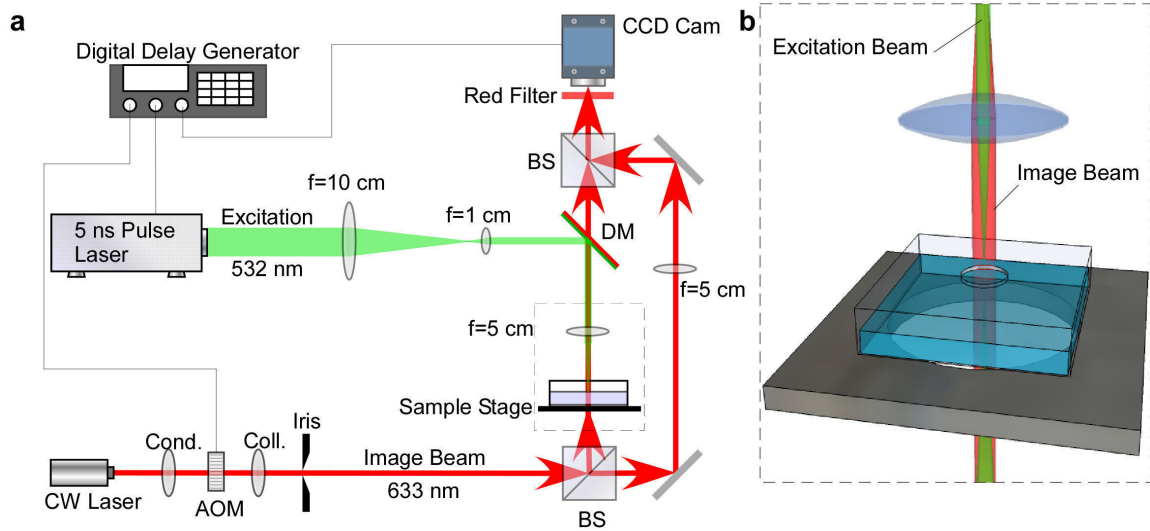


**Figure 5.1.** Experimental apparatus. (a) The cw imaging beam, red, is condensed through the acousto-optic modulator, AOM, then collimated through the iris (only while the AOM is triggered). The collimated beam enters the Mach-Zehnder interferometer where the first 50/50 beam splitter, BS, separates the beam into object and reference arms, with matching objective lenses, and the second BS recombines the two for the CCD camera. The pulsed excitation beam, green, is condensed and collimated by a 10:1 focal length lens pair. A dichroic mirror, DM, transmits the imaging beam while reflecting the excitation beam down toward the sample. The shared 5 cm focal length objective lens loosely focuses the excitation beam onto the interface of interest. (b) A magnified view of the dual-beam sample region (dashed area of (a)).

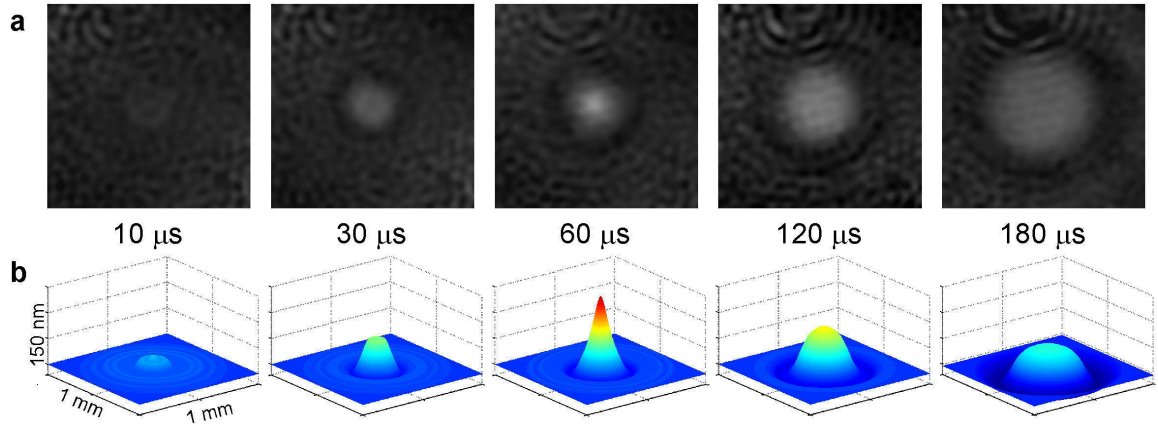


**Figure 5.2.** Time-dependent surface response to optical impulse for DI water. (a) Raw phase images (1.0 x 1.0 mm) of selected time steps and (b) corresponding azimuthal averaged 3D reconstruction (1.0 mm x 1.0 mm x 150 nm).

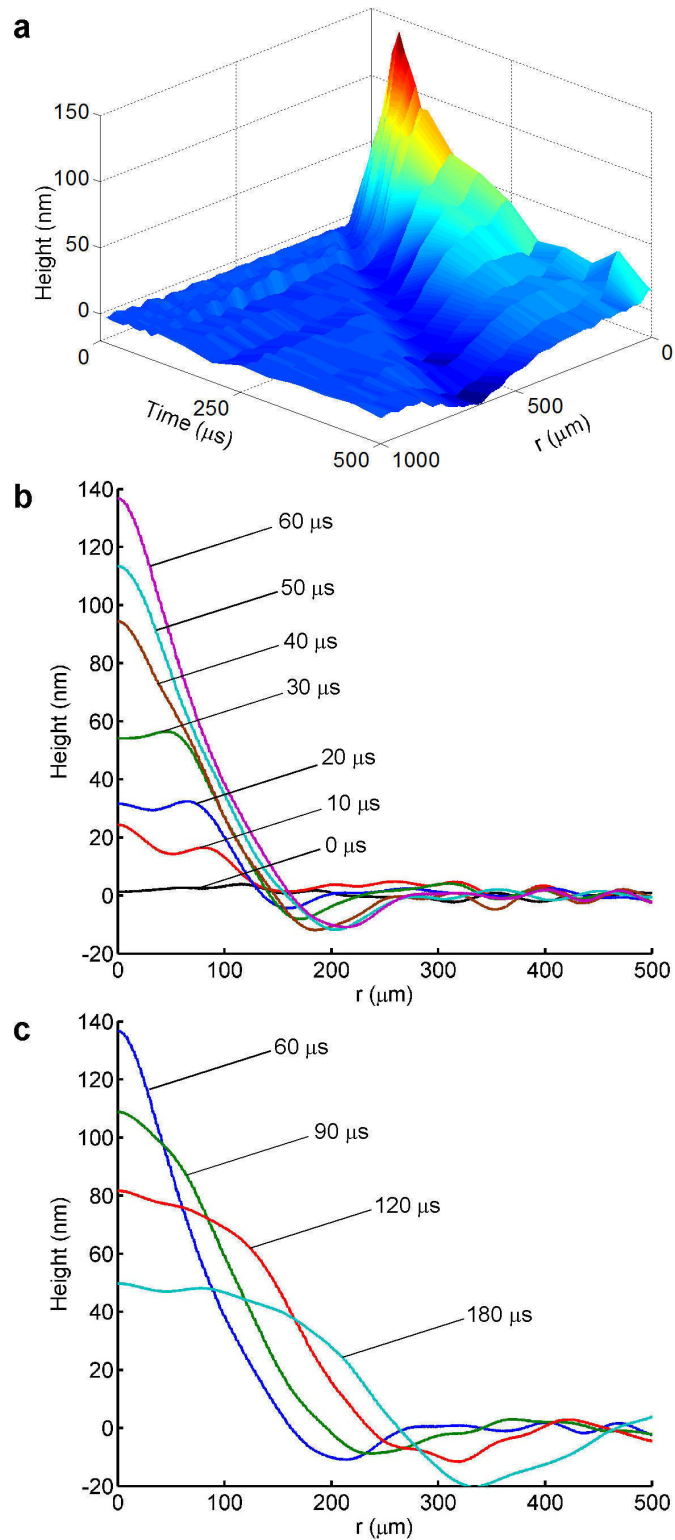


**Figure 5.3.** Time-series data. (a) Spatiotemporal plot of a complete time series. (b) Height profiles for selected time steps during deformation and (c) relaxation.

## 5.2 Theory

The initial deformation is a direct result of the conservation of photon momentum [12] as the photon encounters a boundary of differing refractive indices [7, 13, 14] described by,

$$\frac{n_1 h\nu}{c} \hat{z} = \left( T \frac{n_2 h\nu}{c} - R \frac{n_1 h\nu}{c} \right) \hat{z} + \bar{p}$$

where  $n_1$  and  $n_2$  are the refractive indices of the first and second media, respectively,  $T$  and  $R$  are the transmittance and reflectance,  $h\nu/c$  is the photon's momentum in vacuum and the final term,  $\bar{p}$  represents the exchange of momentum with the interface. By solving for the simplified case of a flat interface with normal incident photons on transparent media, we have for the momentum exchange,

$$\bar{p} = \frac{h\nu}{c} 2n_1 \left( \frac{n_1 - n_2}{n_1 + n_2} \right) \hat{z}.$$

It is easy to see from this relation that the direction of momentum transfer, and therefore the deformation of the interface, will always point in the direction of the smaller refractive index regardless of the direction of beam propagation. The resulting phase shift will therefore always be positive (longer optical path length), which is opposite that of the thermal lensing effect [9], making the two easily distinguishable by DH-QPM [15], though the current method of pulsed excitation eliminates this necessity [16]. The observed phase profile is related to physical surface deformation by,

$$\phi = h(n_2 - n_1) \frac{2\pi}{\lambda}$$

where  $\lambda$  is the wavelength of the imaging beam and  $h$  is the height profile of the deformation field including a capillary wavefront propagating from the source.

The dispersion relation for capillary waves at the interface of two media is described by [17],

$$\omega^2 = \kappa^2 \left( \frac{\sigma \kappa}{\rho + \rho_a} \right)$$

where  $\rho$  and  $\rho_a$  are the densities of the lower and upper fluids, respectively,  $\kappa$  is the angular wavenumber, and  $\sigma$  represents the surface tension between the fluids. For the present case of the air-liquid interface  $\rho_a$  can be dropped since  $\rho_a \ll \rho$  and by substituting the phase velocity,  $v = \omega / \kappa$ , the relation can be written succinctly,

$$v = \sqrt{\frac{\sigma \kappa}{\rho}}.$$

In our experiments, we track the single-pulse capillary wavefront position as a function of time (figure 5.4(a-d)) to determine a velocity. We acknowledge at this point that the determination of a wavenumber is not straightforward for a single propagating pulse. The wavenumber for a repeating waveform is determined by the distance between corresponding points of two adjacent cycles. Since a single pulse is not amenable to this definition, we determine our disturbance wavenumber when the source deformation reaches its maximum height. At this time step, the half-wavelength, and therefore the wavenumber, can be determined by the horizontal distance from the center to the minima of the deformation. This method of determining our single pulse wavenumber has been

sustained empirically thus far. Therefore, we shift  $t = 0$  to this time step and, by integrating with respect to time, we can write the linear expression

$$r(t) = t \sqrt{\frac{\sigma \kappa}{\rho}} + \frac{\pi}{\kappa}$$

where the second term on the right is the constant of integration defined by our initial boundary condition. The slope of this relation yields the surface tension for our given wavenumber and density. Since this input wavenumber may vary from one experiment to the next and the density value will change for different interfaces, the relation of  $(r(t) - \pi / \kappa) \sqrt{\rho / \kappa}$  vs.  $t$  can be plotted for the purpose of universal comparison as shown in figure 5.4(e). The square of the slope of this relation is then equal directly to the surface energy of the interface. We note here that it is only necessary to create an observable capillary disturbance in order to make use of our method. It is not necessary to have additional knowledge of the properties that may describe the deformation itself.

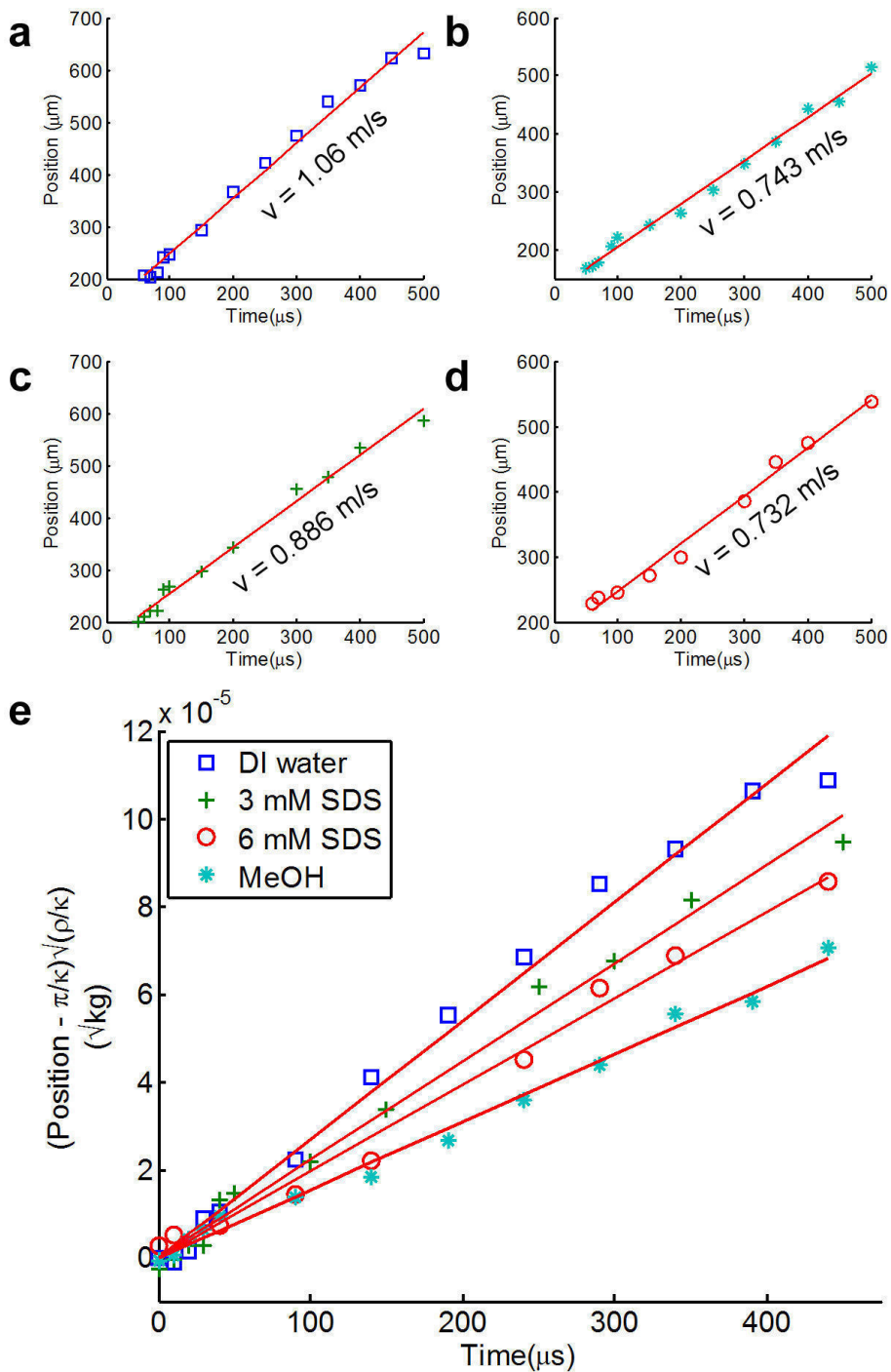


**Figure 5.4.** Capillary wave front velocity. Position vs. time plots of data and linear fits for: (a) DI water, (b) methanol, (c) 3 mM SDS in DI water, and (d) 6 mM SDS in DI water. (e) Comparison plot of  $(r(t)-\pi/\kappa)\sqrt{(\rho/\kappa)}$  vs.  $t$  for each sample type where the square of each slope is equal to the surface tension.

### 5.3 Experiments

The diagram of the experimental apparatus is shown in figure 5.1 with a close-up view of the dual-beam sample region. A version of the improved Mach-Zehnder interferometer design introduced in section 3.3.3 is used to create a hologram of the sample using low power ( $<1\text{mW}$ ) 633-nm laser light. The imaging beam arrives collimated at a beam splitter that transmits half the beam into the reference arm and reflects half the beam into the object arm of the interferometer. The beams each follow a similar path, through matching singlet objective lenses, before recombining by another beam splitter. The interference of the phase-modulated object beam with the reference beam creates the hologram and is recorded by a digital CCD camera placed atop the setup. The holograms are processed by our LabVIEW personal computer platform for amplitude and phase reconstruction based on the angular spectrum method [18].

An integrated optical excitation arm delivers a 532-nm, 5 ns pulse to the system. The pulse energy is adjustable from 0-25 mJ with a built in attenuator. For all present experiments, the output was set to  $\sim 5$  mJ. The pulse-beam is passed through a 10:1 focal length lens pair to create a much reduced beam radius. A dichroic mirror reflects this excitation beam down toward the sample while allowing the probe beam to transmit up toward the CCD camera. The excitation beam passes through the shared objective lens which loosely focuses the already narrowed beam through the sample area. The objectives are chosen to have long effective focal lengths to aid in maintaining constant beam radius at the interface ( $\sim 100\mu\text{m}$  presently). A removable red bandpass filter is

placed just in front of the CCD camera to filter out any 532-nm excitation light leaking through the dichroic mirror.

The sample consists of a partially liquid-filled modified glass cuvette 10 mm by 40 mm by 45 mm with a sealable lid. The cuvette is placed on the sample stage on its side oriented with a 10 mm path length. The liquid level in the cuvette is filled to a height of 5 mm in this orientation. The modified cuvette has a small (~6 mm) hole drilled through the upper glass surface providing an unimpeded excitation beam delivery. All general phase aberration, including wavefront curvature mismatch, can be easily compensated for by storing a background phase image prior to excitation and subtracting this from the excited images. Additional compensation for the inherent dynamic nature of the free liquid surface is also easily achieved as needed with DH-QPM.

A digital delay generator controls precise timing of both excitation and imaging. Prior to delivery to the system, the imaging beam is condensed through an acousto-optic modulator (AOM) which, during triggering, diffracts the imaging beam through a collimating lens and iris. The pulse delay generator sends a 5  $\mu$ s square pulse signal to this AOM shutter system at specified delay times relative to the excitation pulse. This delivery method produces the short exposure images required for this study without sacrificing phase quality as would be likely if a pulsed imaging beam were used instead.

We have employed here a time-resolved imaging technique which requires each time step to be the result of a separate optical impulse followed by an appropriately delayed short (5  $\mu$ s) camera exposure. This introduces some uncertainty due to variation in the output energy of each pulse. The use of a high-speed camera or alternative rapid

imaging method may eliminate this uncertainty; however, the demonstration of our proposed technique's capabilities is affected little by this.

First, we characterized our technique for known substances at both high and low surface energy standards. For the high range, we chose the deionized (DI) water-air interface as the expected value is well known to be 72.8 mN/m at 20°C [19]. Our measured surface energy for this interface was  $72.9 \pm 0.6$  mN/m where the tolerance here represents the standard deviation of repeated trials. For the low range standard, we chose the methanol-air interface with a previously reported surface energy of 22.6 – 22.9 mN/m at 20°C [19, 20] and we have measured this to be  $23.8 \pm 0.3$  mN/m.

Some differences in these values may be expected due to the noncontact nature of our approach versus the typical probe techniques traditionally used for this measurement. For now, we will assume that the above measurements are reasonably close to expected values and continue with the application of our method to chemical monolayers. Again, we have chosen a well-known surfactant, sodium dodecyl sulfate (SDS), whose effect on the water-air interface has been studied previously [21, 22]. An SDS molecule contains a hydrophilic head group and a hydrophobic tail. As such, when molecules of SDS are added to water they have an affinity for a boundary where the tail can point away from the polar liquid. It is this behavior that gives SDS its surface energy reducing effect as it reduces the strength of attraction of the surface water molecules toward one another.

We measured the surface energy at the solution-air interfaces of 3 mM and 6 mM SDS concentrations in DI water. Our results of 50.1 mN/m and 38.9 mN/m, respectively, are within the expected range for typical stock solutions at these concentrations [21]. It can be noted here that a variation around measured values for such mixtures are discussed

at length in the cited reference. It is beyond the scope of our study to address this; however, this dynamic nature of monolayers presents a favorable application for our method as will be discussed shortly.

#### **5.4 Discussion and Conclusion**

There are several advantages inherent to the method described here, not the least of which is the freedom of choices for excitation and imaging sources. Since the optical pressure effect is entirely dependent on the difference in refractive index across the interface, the choice of excitation wavelength can be freely changed to benefit the application without cost to the mode of operation. Furthermore, since the imaging method is entirely phase related, the choice of imaging wavelength is also free to depend upon the application at hand or the availability of resources. In either case, the best choices would be the most transparent to the system to avoid any chance of unwanted thermal or scattering effects, but in most cases a broad selection of sources will perform the task with little consequence.

The use of time-resolved DH-QPM has some additional inherent advantages and adaptations, as well. Mainly, through careful construction, DH-QPM has been shown to measure optical path differences in the sub-nanometer range [10] making it well-suited for observation of very small physical disturbances qualifying the use of mild excitation pulses. Since DH-QPM is a 3D volumetric imaging method [23], it is also possible to observe the multiple interfacial planes of a complex, layered system with a single time series of holograms using the same excitation pulse. Furthermore, because the basis of the measurement is the capillary wavefront velocity, the temporal resolution requirement

may be less stringent at lower surface energies suggesting this method to be well adapted for such applications.

Surface tension is traditionally thought of as a characteristic property of an entire interface. As alluded to earlier, particularly in the case of monolayers, the surface energy can be quite dynamic and likely varies from region to region of a given surface based on localized conditions. In many cases, it may be of interest to monitor these local values of surface energy rather than attempting to obtain a single value for the surface as a whole. The technique presented here is adapted to this kind of localized measurement and can be adjusted in scale to match the region of interest for a given application simply by choice of lenses. Where measurements like this are intended, it would certainly be of high importance to use a noncontact method such as that introduced here.

The surface energy of biological cell membranes and systems has long been a topic of interest and studies continue to emerge as modern techniques prevail [24-27]. Of particular need are techniques that can perform this analysis in living cells as they undergo natural processes and life cycle behavior. The noninvasiveness of the applied method is therefore of utmost importance. Several optical approaches have been practiced including stretching of the cell [28] or optical tweezing techniques which involve the use of microspheres attached to or inserted inside of the cellular membrane [29, 30]. The use of optical forces on these membranes without the need for stretching or foreign microspheres in contact would be a distinct improvement. With the advantages described in the preceding paragraphs, our noncontact single optical pressure pulse method could be an excellent candidate for such applications.

## 5.5 References

1. Hu, H.H., and Joseph, D.D., "Evolution of a Liquid Drop in a Spinning Drop Tensiometer," *J. Colloid Interf. Sci.* **162**, 331-339 (1994).
2. Lin, S.-Y., and Hwang, H.-F., "Measurement of Low Interfacial Tension by Pendant Drop Digitization," *Langmuir* **10**, 4703-4709 (1994).
3. Franses, E. I., Basaran, O. A., and Chang, C.-H., "Techniques to measure dynamic surface tension," *Curr. Opin. Colloid In.* **1**, 296-303 (1996).
4. Tsay, R.-Y., Yan, S.-C., and Lin, S.-Y., "A video-enhanced plate method for simultaneous measurements of surface tension and contact angle," *Rev. Sci. Instrum.* **66**, 5065-5069 (1995).
5. Ashkin, A., "History of optical trapping and manipulation of small-neutral particle, atoms, and molecules"" *IEEE J. Sel. Top. Quant.* **6**, 841-856 (2000).
6. Sakai, K., Mizuno, D., and Takagi, K., "Measurement of liquid surface properties by laser-induced surface deformation spectroscopy," *Phys. Rev. E* **63**, 046302 (2001).
7. Casner, A. and Delville, J.-P., "Adaptative lensing driven by the radiation pressure of a continuous-wave laser wave upon a near-critical liquid liquid interface," *Opt. Lett.* **26**, 1418-1420 (2001).
8. Marcano, A., Loper, C., and Melikechi, N., "High-sensitivity absorption measurement in water and glass samples using a mode-mismatched pump-probe thermal lens method," *Appl. Phys. Lett.* **78**, 3415-3417 (2001).
9. Clark, D. C. and Kim, M. K., "Determination of absorption coefficient by digital holographic measurement of optical excitation," *Appl. Opt.* **50**, 1668-1672 (2011).

10. Clark, D. C. and Kim, M. K., "High-precision method for measuring the photothermal properties of transparent media with digital holography (Invited Paper)," *Chin. Opt. Lett.* **9**, 120001 (2011).
11. Mitani, S. and Sakai, K., "Measurement of ultralow interfacial tension with a laser interface manipulation technique," *Phys. Rev. E* **66**, 031604 (2002).
12. Hecht, E., *Optics* (Addison Wesley, San Francisco, CA, 2002).
13. Ashkin, A. and Dziedzic, J. M., "Radiation Pressure on a Free Liquid Surface," *Phys. Rev. Lett.* **30**, 139-142 (1973).
14. Komissarova, I. I., Ostrovskaya, G. V., and Shedova, E. N., "Light pressure-induced deformations of a free liquid surface," *Opt. Commun.* **66**, 15-20 (1988).
15. Clark, D. C. and Kim, M. K., "Time-dependent phase response of fluid interface to optical excitation," in *Frontiers in Optics*, OSA Technical Digest, FThU5 (Optical Society of America, 2011).
16. Clark, D. C. and Kim, M. K., "Time-dependent Surface Response of Fluid to Transmission Optical Pressure Impulse," in *Digital Holography and Three-Dimensional Imaging*(Optical Society of America, Miami, FL, 2012), p. DW1C.5.
17. Landau, L. D. and Lifshitz, E. M., *Fluid Mechanics* (Pergamon Press, London, 1959).
18. Kim, M. K., "Principles and techniques of digital holographic microscopy," *SPIE Reviews* **1**, 018005 (2010).
19. Vazquez, G., Alvarez, E., and Navaza, J. M., "Surface Tension of Alcohol Water + Water from 20 to 50 .degree.C," *J. Chem. Eng. Data* **40**, 611-614 (1995).

20. Součková, M., Klomfar, J., and Pátek, J., “Measurement and Correlation of the Surface Tension–Temperature Relation for Methanol,” *J. Chem. Eng. Data* **53**, 2233-2236 (2008).
21. Mysels, K. J., “Surface tension of solutions of pure sodium dodecyl sulfate,” *Langmuir* **2**, 423-428 (1986).
22. Kawai, T., Kamio, H., Kondo, T., and Kon-No, K., “Effects of Concentration and Temperature on SDS Monolayers at the Air–Solution Interface Studied by Infrared External Reflection Spectroscopy,” *J. Phys. Chem. B* **109**, 4497-4500 (2005).
23. Kim, M., *Digital Holographic Microscopy: Principles, Techniques, and Applications* (Springer, 2011).
24. Hochmuth, R. M., “Micropipette aspiration of living cells,” *J. Biomech.* **33**, 15-22 (2000).
25. Spelt, J., Absolom, D., Zingg, W., van Oss, C., and Neumann, A., “Determination of the surface tension of biological cells using the freezing front technique,” *Cell Biochem. Biophys.* **4**, 117-131 (1982).
26. Brodland, G. W., Yang, J., and Sweny, J., “Cellular interfacial and surface tensions determined from aggregate compression tests using a finite element model,” *HFSP J.* **1**, 108 (2009).
27. David, R., Ninomiya, H., Winklbauer, R., and Neumann, A. W., “Tissue surface tension measurement by rigorous axisymmetric drop shape analysis,” *Colloid Surface B* **72**, 236 (2009).

28. Guck, J., Ananthakrishnan, R., Mahmood, H., Moon, T. J., Cunningham, C. C., and Käs, J., “The Optical Stretcher: A Novel Laser Tool to Micromanipulate Cells,” *Biophys. J.* **81**, 767-784 (2001).
29. Dai, J. and Sheetz, M. P., “Mechanical properties of neuronal growth cone membranes studied by tether formation with laser optical tweezers,” *Biophys. J.* **68**, 988-996 (1995).
30. Hénon, S., Lenormand, G., Richert, A., and Gallet, F., “A New Determination of the Shear Modulus of the Human Erythrocyte Membrane Using Optical Tweezers,” *Biophys. J.* **76**, 1145-1151 (1999).

## **CHAPTER 6**

### **CONCLUSIONS AND FUTURE WORK**

Our research has successfully made use of the advantages of digital holography and, more specifically, the angular spectrum method to observe and measure structures which are otherwise unobservable by standard optical microscopy. We have incorporated specialized techniques and fabricated unique apparatus to suit the growing demands of our research goals. The observation of the individual phase effects of both photothermal and optical radiation pressure phenomena have required mathematical modeling and computer simulation to define the necessary parameters for the fabrication of the apparatus and experimental design. We have shown that the effects can be successfully decoupled and precisely measured independently and have found useful applications for our work as it has progressed. Additionally, as our research evolved, so did the quality of our imaging apparatus and software processing. In this chapter we will summarize the main conclusions of the topics described in this dissertation.

#### **6.1 Summary of conclusions**

The importance of quantitative phase imaging and the advantages of the angular spectrum method of digital holography were made apparent in chapter 2. The purely phase nature of the thermal lens and the nanometric surface disturbances of the optical

pressure effect render direct optical microscopy methods useless. Digital holographic quantitative phase microscopy (DH-QPM) was necessary for the precise measurement and therefore the real-world applications of our results. Since the formulation of the angular spectrum method (ASM) is based on the fundamental properties of the Fourier transform, there is no need to impose boundary conditions as with comparative methods. In addition, there are advantages that have important consequences when the integrals are discretized for numerical diffraction such as; the diffraction is constructed from well-behaved plane waves instead of spherical waves with point source singularities, and there is no requirement for the approximation factor,  $r \approx z$ , as with the Fresnel transform method. Combining these advantages with the ease of angular spectrum filtering and phase aberration compensation made DH-QPM by ASM an ideal choice for the research topics investigated in this dissertation.

In order to study the effect of optical radiation pressure on the surface of a fluid, it was first very important to fully investigate the thermal effects from optical interaction. The use of quantitative phase imaging as the method of detection means sensitivity to both dimensional changes and optical density changes. In chapter 3, the thermal lens was described and mapped both spatially and temporally and the results were used as a sensitive tool for the measurement of the absorption coefficient of transparent media. Although we have shown our initial approach to be an improvement in both accuracy and precision over previously existing methods, our apparatus and process have undergone continued improvement during the course of our thermal lens investigations. In fact, measurement of thermal lensing can be used as a standard to demonstrate our improvements in parameter measurement precision as shown in table 6.1. These

improvements became increasingly important, of course, in the optical pressure deformation experiments that followed.

**Table 6.1.** Comparison of improved measurement precision.

<b>Parameter</b>	<b>Previous Reference[1]<sup>1,2</sup></b>	<b>Initial DH-QPM<sup>1</sup></b>	<b>Improved Apparatus<sup>3</sup></b>	<b>Azimuthal Averaging<sup>3,4</sup></b>
<b>Phase (mrad)</b>	200	120	10	2
<b>Temperature (K)</b>	0.012	0.0072	0.0005	0.0001
<b>Refractive Index</b>	$4 \times 10^{-6}$	$2.4 \times 10^{-6}$	$1.7 \times 10^{-7}$	$3.4 \times 10^{-8}$
<b>Optical Thickness (nm)</b>	20	12	0.8	0.2
<b>Absorption Coef. (cm<sup>-1</sup>)</b>	$5 \times 10^{-5}$	$3 \times 10^{-5}$	$1 \times 10^{-5}$	$2 \times 10^{-6}$

<sup>1</sup>Values taken from methanol study.

<sup>2</sup>Values based on claimed tolerance from reference.

<sup>3</sup>Values taken from benzyl alcohol study.

<sup>4</sup>Radial symmetry required and actual precision dependent on original system noise level.

At this point, we had demonstrated that our DH-QPM method could be immediately useful as a valuable tool in various analytical chemistry applications requiring photothermal property measurement with high sensitivity [2-4]. This was not our intended ultimate goal, but actually a consequence of the required steps in our pursuit of developing a measurement technique for the nanometric deformation caused by optical radiation pressure from photon momentum exchange across fluid interfaces.

In chapter 4, we derived a combined model of these two effects which differ not only greatly in time-scale, but also oppositely in phase signal direction making DH-QPM ideal for their very distinguishable detection. Computer simulations were then performed in order to determine the experimental parameters required to observe them separately.

We then modified our apparatus and processing routine to accommodate the requirements predicted by simulations. A method was implemented to reduce the excitation duration time of the first time-series frame to between 0 and 25 ms, where it was predicted that a deformation could be observed due to the optical pressure on the interface. Subsequent frames were captured at the camera rate of 25 ms intervals with camera exposure times of about 80  $\mu$ s, showing the evolution of the phase signal in time as thermal lensing reversed the phase signal and grew to dominate the interaction. The nearly perfect match between our predictions and our phase measurements demonstrated the completeness of the combined model as well as the ability to use shortened time scales to observe optical pressure deformations before the dominating effects of thermal lensing. This suggested that completely decoupling these effects would be possible by developing a method of controlled DH-QPM capture at much shorter time scales.

In chapter 5, we demonstrated not only a method for completely decoupling the photomechanical from the photothermal effects discussed earlier, but developed a useful and unique noncontact method for the application of measuring mechanical properties of surfaces of soft matter. We introduced a purely optical approach to measuring the localized surface energy of an interface within a system using a single, 5 ns, optical pressure pulse and a time-resolved digital holographic quantitative phase imaging technique to track a propagating nanometric capillary disturbance. The 5 ns pulse does not produce a discernible thermal phase signature and, since there is no additional optical excitation, the time series of data to follow contains only the time-dependent signal due to the mechanical disturbance at the surface. The method was used to measure the surface energy of deionized water, methanol, and chemical monolayers formed by

surfactants with good agreement to published values as summarized here in table 6.2. Due to the noncontact nature of our approach, it is likely that differences in our measurements are due to improved accuracy over the previously reported methods which require the use of an invasive probe. In fact, this is the most significant advantage that our method has over these traditional techniques.

**Table 6.2.** Experimental results for surface tension (mN/m).

	<b>Published Contact Probe Methods[5-7]</b>	<b>Noncontact DH-QPM Method</b>
<b>DI Water</b>	72.8	72.9
<b>Methanol</b>	22.6-22.9	23.8
<b>3 mM SDS</b>	47-57*	50.1
<b>6 mM SDS</b>	35-45*	38.9

\*Range of values taken from figure 7 of Ref[7].

Several additional advantages of the approach in chapter 5 were described. Since both the imaging and excitation mechanisms are grossly independent of source wavelength, there is a large variety of options for these sources increasing adaptability to other applications. We have demonstrated that DH-QPM is capable of subnanometer optical thickness precision making the deformation structures easily visible even with the use of mild excitation energy. Also, the true 3D volumetric imaging capabilities make it easy to propagate to different planes of focus or possibly, under certain circumstances, observe multiple interfacial planes of a more complex layered system with the same time series of holograms. For applications involving very low surface tension measurement,

our approach should be particularly well-suited since the capillary wavefront velocity will notably decrease and the observable deformation will occur with greater ease, thus putting, all around, less restriction on the experimental design. Furthermore, our approach measures the effective surface tension of adjustable regions of interest rather than treating the surface as a whole, which may be of high importance for many applications.

## **6.2 Future Work**

There has long been an interest in the surface energy of biological cell membranes and studies have continued to emerge in recent years [8-11]. Of particular need are techniques that can perform this analysis, with minimal invasiveness, in living cells as they undergo natural processes and life cycle behavior. With this in mind, optical approaches have become quite prominent and recently include optical stretching of the cell [12] or optical tweezing techniques which involve the use of microspheres attached to or inserted inside of the cellular membrane [13, 14]. The use of optical forces on these membranes without the need for stretching or foreign microspheres would be a distinct improvement. We believe our approach to sensing and measurement involving purely optical nanometric manipulation and imaging has important advantages and may be adapted to the study of biological cell membranes.

The approach proposed here is based on the single-pulse optical pressure method described in chapter 5. In this approach, diagramed in figure 6.1, a tightly focused optical radiation beam is applied to a localized portion of the cell membrane. This may produce an observable deformation followed by a capillary wave disturbance on the

membrane surface which may be tracked by time-resolved DH-QPM. The surface energy can then be determined just as described for the chemical monolayers in chapter 5. If scaled properly, this procedure could be applied to various regions of interest around the cell body for a useful profile of the distribution of energies if desired.

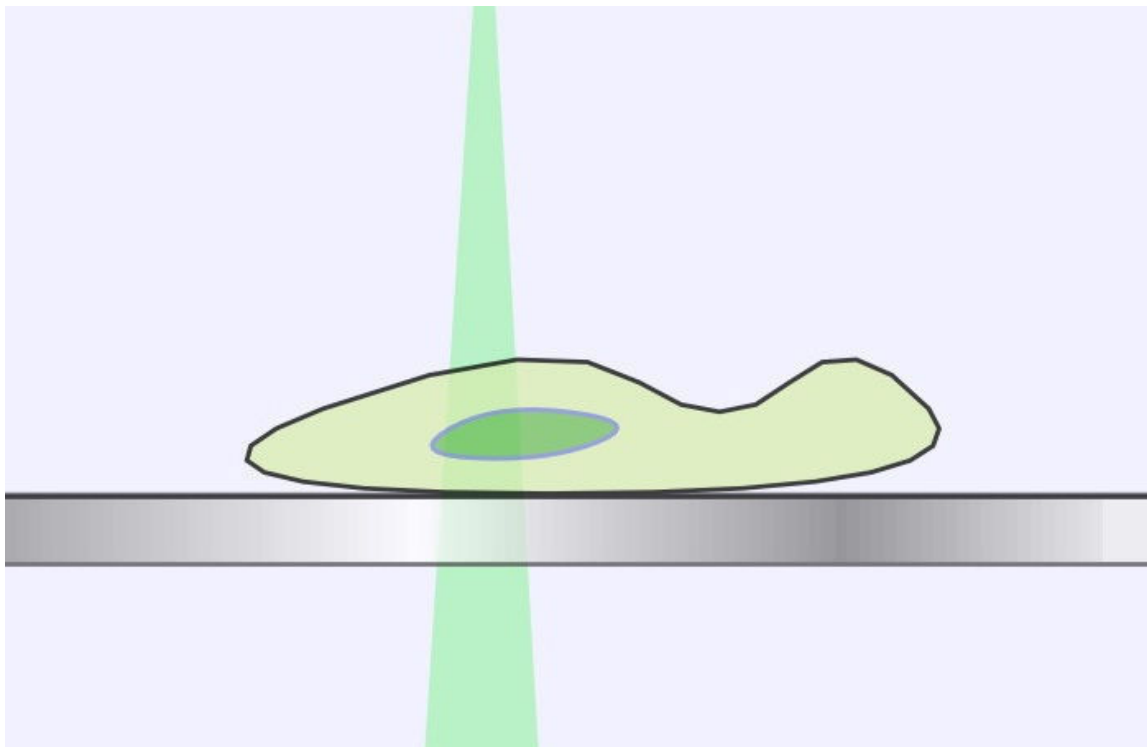


**Figure 6.1.** Application to biological cell membrane.

This application does present several restrictions and barriers to overcome in order to be feasible in practice. Though the technique described can, in theory, be scaled down to accommodate smaller regions of interest, the cell should be large enough that this can be reasonably accomplished. Also, the cell must be transparent to the imaging light and to the excitation light, so many cellular species may impose high limitations on these sources. Even if the cell is mostly transparent, the state of the cell may alter availability of the transparent regions for the experiment, for example, by shifting non-

transparent organelles or particulates around. Additionally, the cell and its surface must remain free of any unwanted capillary vibrations that may occur on similar time scales to those induced from the excitation source. While our experiments performed in chapter 5 were time-resolved by a technique that did not require a high-speed camera, the motion of certain cell species may demand this expensive adaptation. Finally, even if a cell is highly transparent to the selected excitation source, it may be possible to cause damage to the cell which prevents completion of the measurement, especially if the spot-size has been scaled down significantly, such as to accommodate the requirements of certain cell species.

Regardless of the possible limitations that may be imposed, we believe the application described here is worth exploring. There are many variations available for the method described and it is likely that it can be adapted to achieve the proposed goals for many cell species. In fact, even a few successful representative cell species could greatly increase the existing knowledge of the relationships between cellular membrane surface energy and environmental, behavioral, or developmental factors.

### **6.3 References**

1. Cabrera, H., Marcano, A., and Castellanos, Y., "Absorption coefficient of nearly transparent liquids measured using thermal lens spectrometry," *Condensed Matter Physics*, **9**, No. 2(46), 385-389 (2006).
2. Pegau, W.S., Gray, D., and Zaneveld, J.R.V., "Absorption and attenuation of visible and near-infrared light in water: dependence on temperature and salinity," *Appl. Opt.*, **36**(24), 6035 (1997).

3. Babin, M., Stramski, D., Ferrari, G.M., Claustre, H., Bricaud, A., Obolensky, G., and Hoepffner, N., "Variations in the light absorption coefficients of phytoplankton, nonalgal particles, and dissolved organic matter in coastal waters around Europe," *J. Geophys. Res.*, **108**(C7), 3211 (2003).
4. Colcombe, S.M., Lowe, R. D., Snook, R.D., "Thermal lens investigation of the temperature dependence of the refractive index of aqueous electrolyte solutions," *Anal. Chim. Acta*, **356**, 277 (1997).
5. Vazquez, G., Alvarez, E., and Navaza, J. M., "Surface Tension of Alcohol Water + Water from 20 to 50 .degree.C," *J. Chem. Eng. Data* **40**, 611-614 (1995).
6. Součková, M., Klomfar, J., and Pátek, J., "Measurement and Correlation of the Surface Tension–Temperature Relation for Methanol," *J. Chem. Eng. Data* **53**, 2233-2236 (2008).
7. Mysels, K. J., "Surface tension of solutions of pure sodium dodecyl sulfate," *Langmuir* **2**, 423-428 (1986).
8. Hochmuth, R. M., "Micropipette aspiration of living cells," *J. Biomech.* **33**, 15-22 (2000).
9. Spelt, J., Absolom, D., Zingg, W., van Oss, C., and Neumann, A., "Determination of the surface tension of biological cells using the freezing front technique," *Cell Biochem. Biophys.* **4**, 117-131 (1982).
10. Brodland, G. W., Yang, J., and Sweny, J., "Cellular interfacial and surface tensions determined from aggregate compression tests using a finite element model," *HFSP J.* **1**, 108 (2009).

11. David, R., Ninomiya, H., Winklbauer, R., and Neumann, A. W., "Tissue surface tension measurement by rigorous axisymmetric drop shape analysis," *Colloid Surface B* **72**, 236 (2009).
12. Guck, J., Ananthakrishnan, R., Mahmood, H., Moon, T. J., Cunningham, C. C., and Käs, J., "The Optical Stretcher: A Novel Laser Tool to Micromanipulate Cells," *Biophys. J.* **81**, 767-784 (2001).
13. Dai, J. and Sheetz, M. P., "Mechanical properties of neuronal growth cone membranes studied by tether formation with laser optical tweezers," *Biophys. J.* **68**, 988-996 (1995).
14. Hénon, S., Lenormand, G., Richert, A., and Gallet, F., "A New Determination of the Shear Modulus of the Human Erythrocyte Membrane Using Optical Tweezers," *Biophys. J.* **76**, 1145-1151 (1999).

## BIBLIOGRAPHY

Kim, M. K. *Digital Holographic Microscopy: Principles, Techniques, and Applications*, 1<sup>st</sup> edn, (Springer, 2011).

Schnars, U. and Jueptner, W., *Digital Holography*, (Springer Verlag, 2005).

Hecht, E., *Optics*, 4<sup>th</sup> edn, (Addison Wesley, 2002).

Goodman, J. W., *Introduction to Fourier Optics*, 2<sup>nd</sup> edn, (McGraw-Hill, 1996).

Landau, L. D. and Lifshitz, E. M., *Fluid Mechanics*, (Pergamon Press, 1959).

Brash, J. L. and Wojciechowski, P. W., *Interfacial phenomena and bioproducts*, (Marcel Dekker, 1996).

Bender, M., *Interfacial phenomena in biological systems*, (Marcel Dekker, 1991).

Myers, D., *Surfaces, interfaces, and colloids: principles and applications*, 2<sup>nd</sup> edn, (Wiley-VCH, 1999).

## **APPENDICES**

**APPENDIX A**  
**APPARATUS PHOTOGRAPHS**

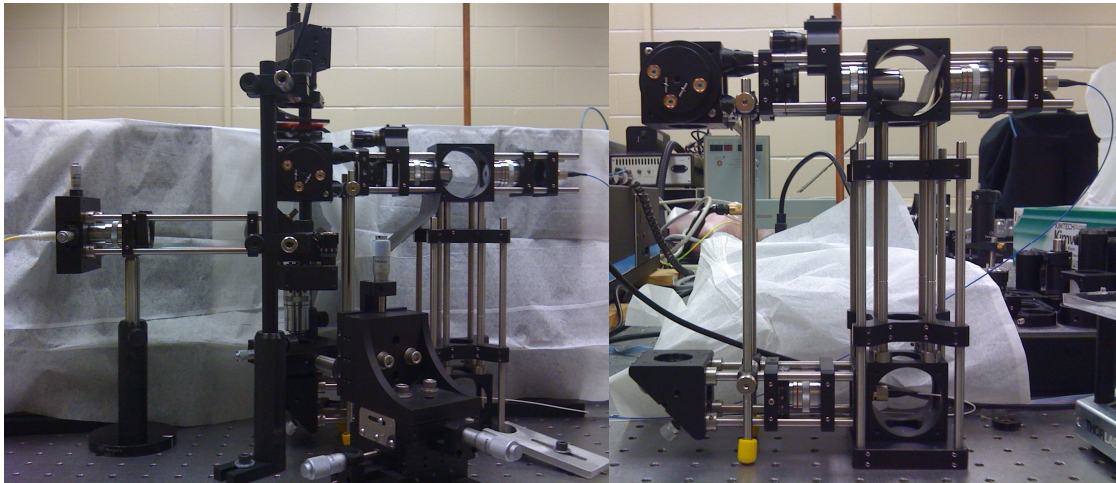


**Figure A.1.** Early apparatus. Left: Complete assembled apparatus with CW excitation beam delivered by fiber optic from the left and imaging (reference and object) beams delivered separately from the right by 50/50 beam-splitting fiber optic from single HeNe source. Right: Mach-Zehnder interferometer with other components removed for clarity.

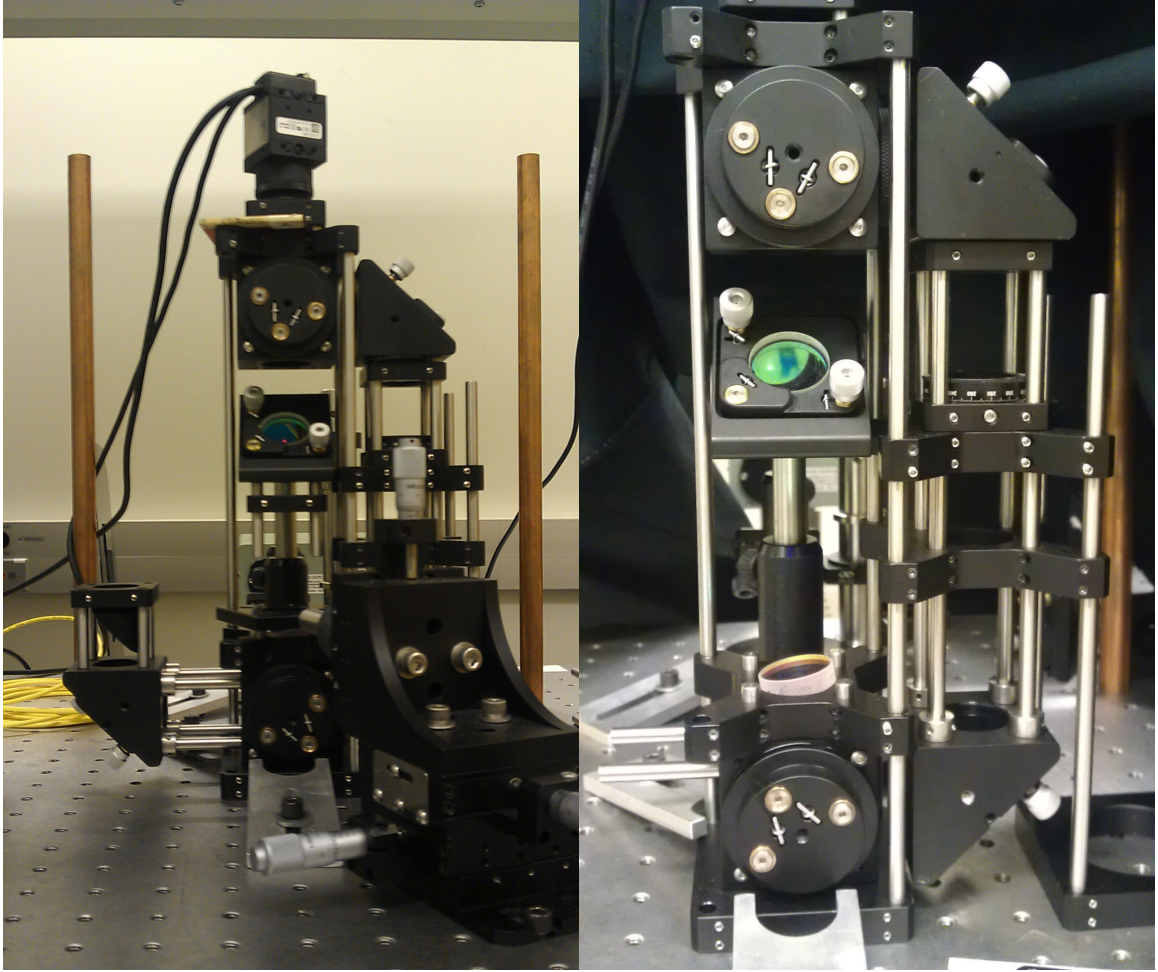


**Figure A.2.** Improved apparatus. Compact, low-noise Mach-Zehnder interferometer for high-precision phase imaging (shown on the right with some components removed for clarity). Single imaging beam enters lower beam splitter from the left and excitation arm enters at the dichroic mirror from the back.

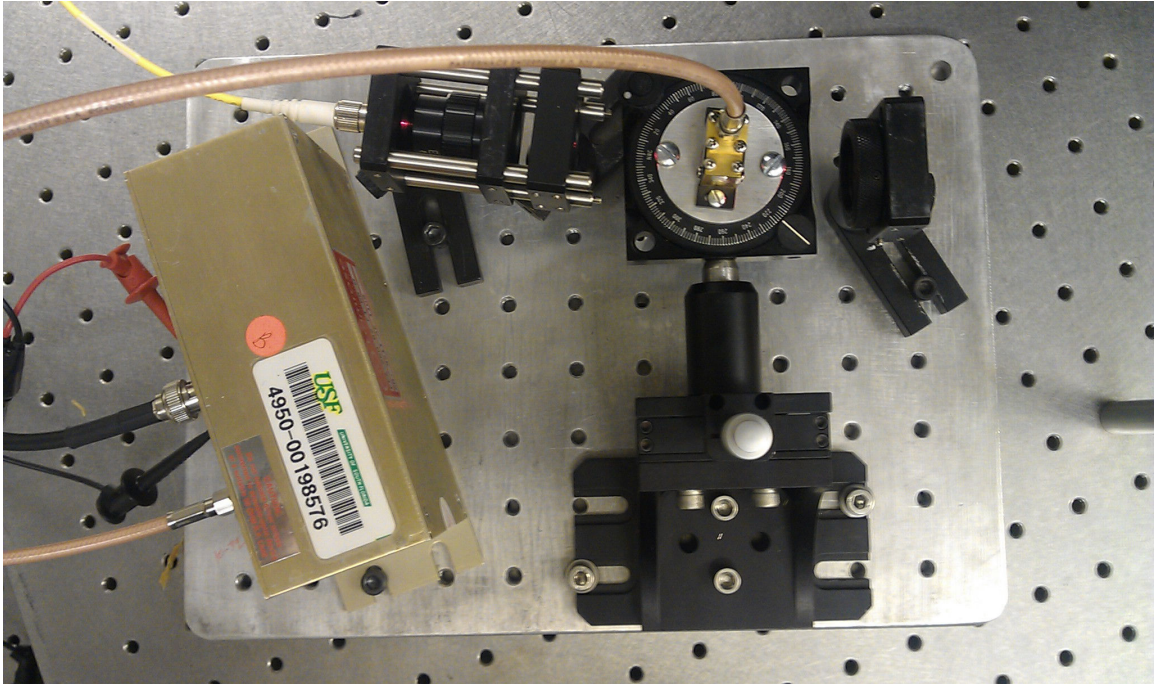


**Figure A.3.** Acousto-Optic Modulator (AOM) shutter system. Imaging beam enters from HeNe source through fiber optic from left, is condensed through AOM and diffracted (when triggered by driver) through iris and collimating lens exiting to the right.

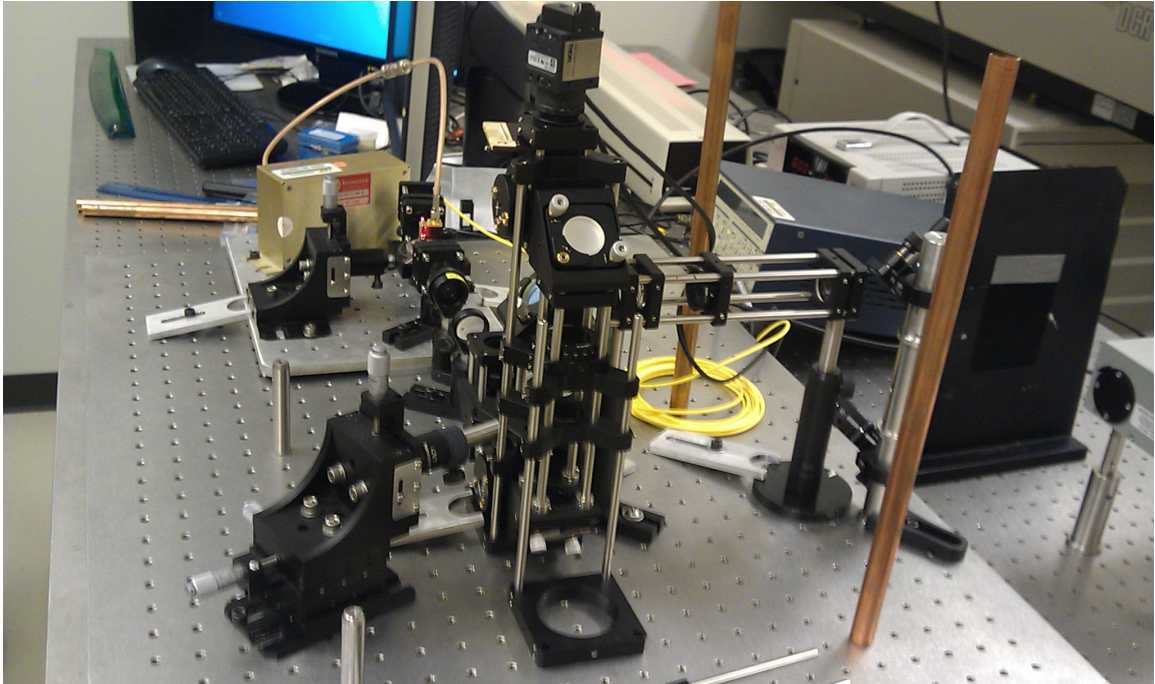


**Figure A.4.** Pulsed optical pressure, time resolved DH-QPM apparatus complete.

**APPENDIX B**  
**COMPUTER PROGRAMS**

Displayed here are some of the important LabVIEW and MATLAB software developments created for the purpose of this research.

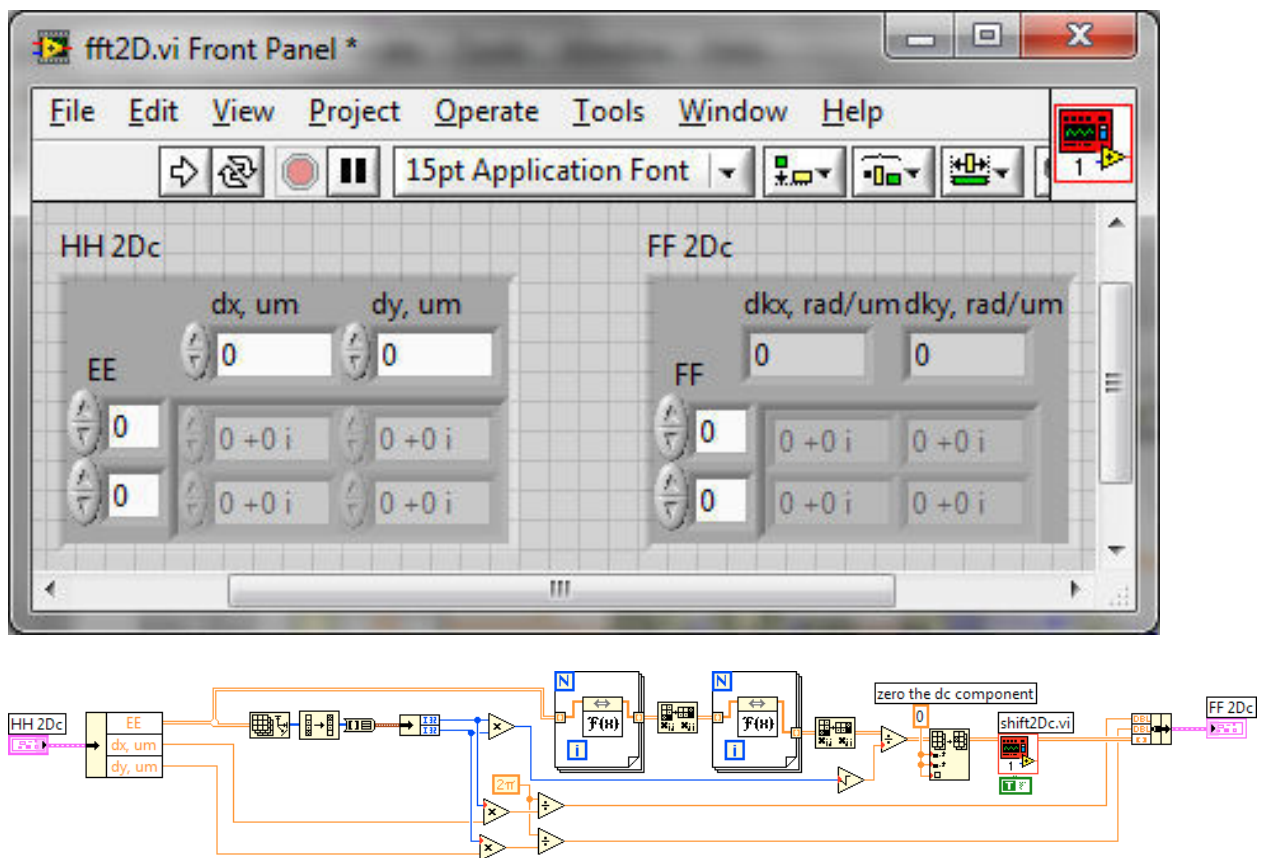


**Figure B.1.** Front panel and block diagram of the Fourier Transform VI.

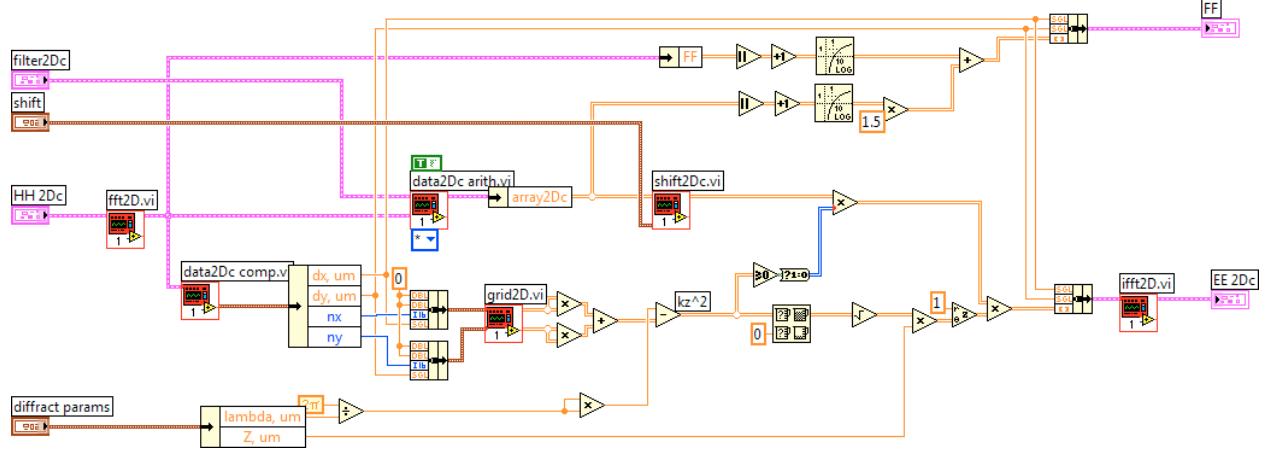
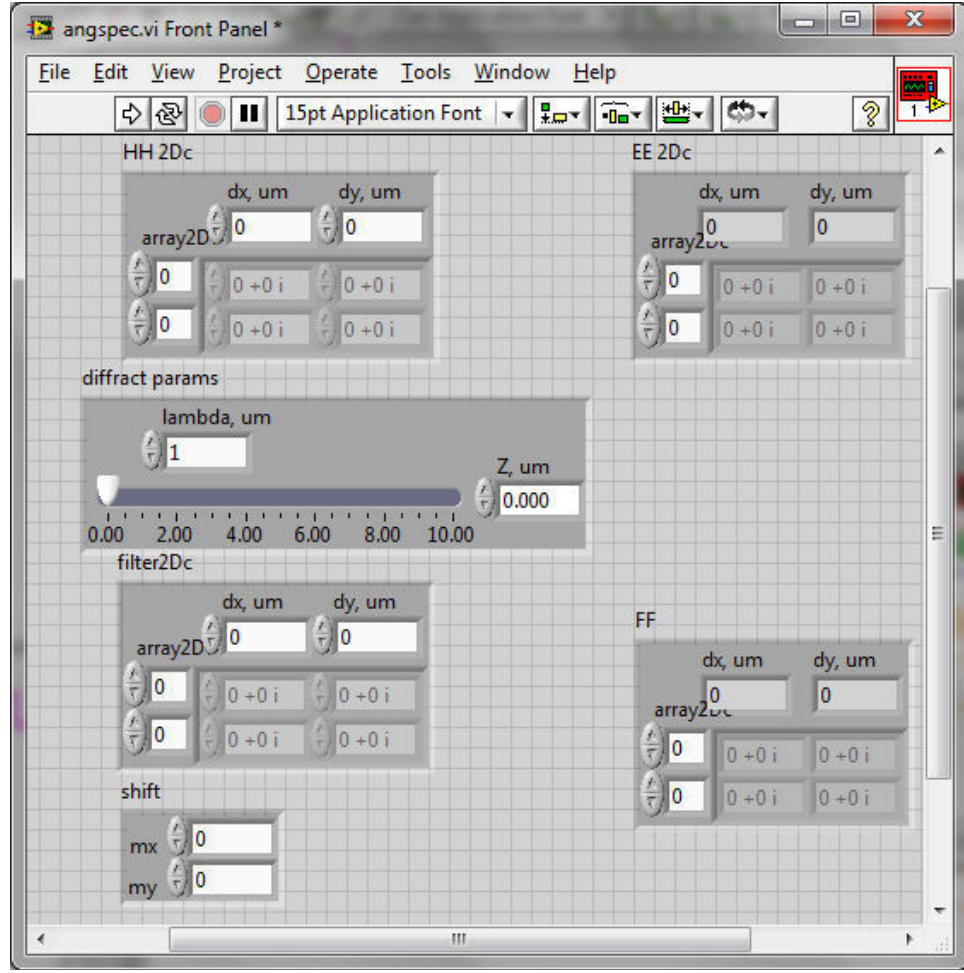


**Figure B.2.** Front panel and block diagram of the sub-VI for filtered angular spectrum numerical diffraction.

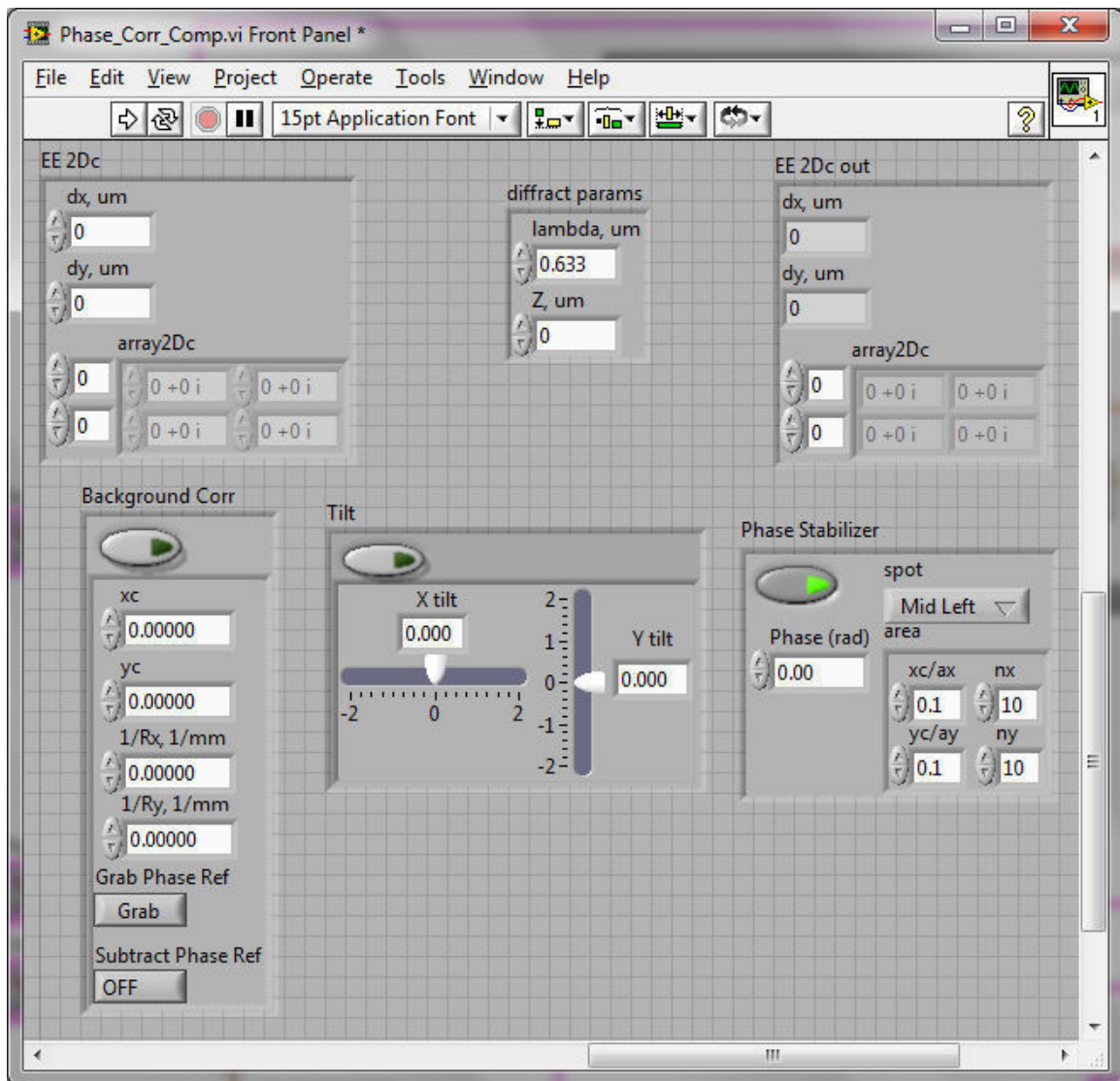


**Figure B.3.** Front panel of the sub-VI for phase correction routines.

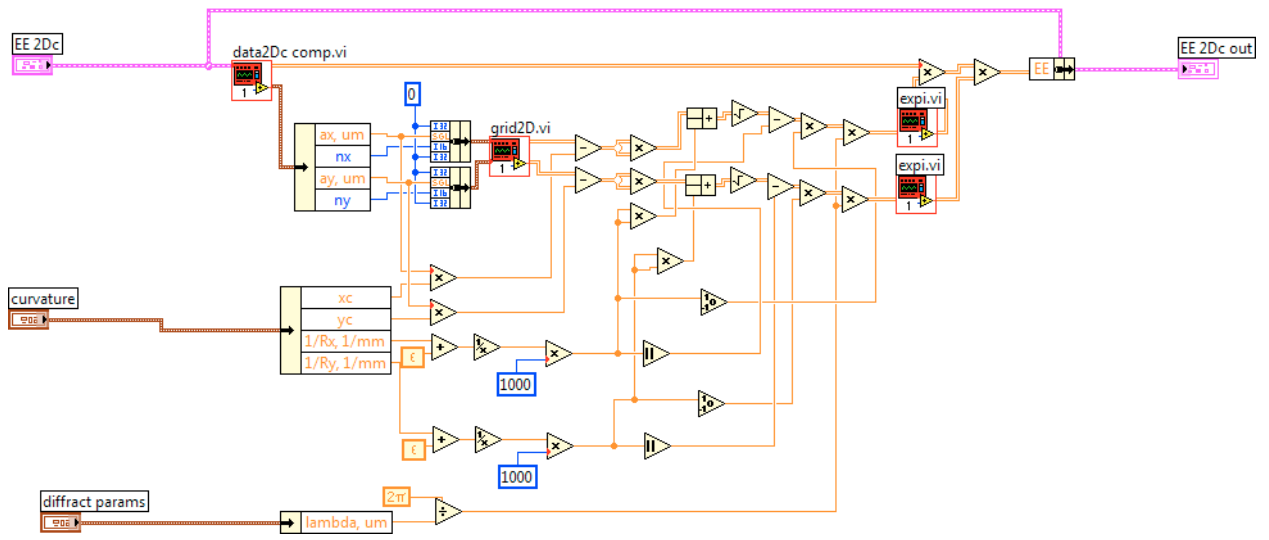


**Figure B.4.** Block diagram for wavefront curvature mismatch correction.

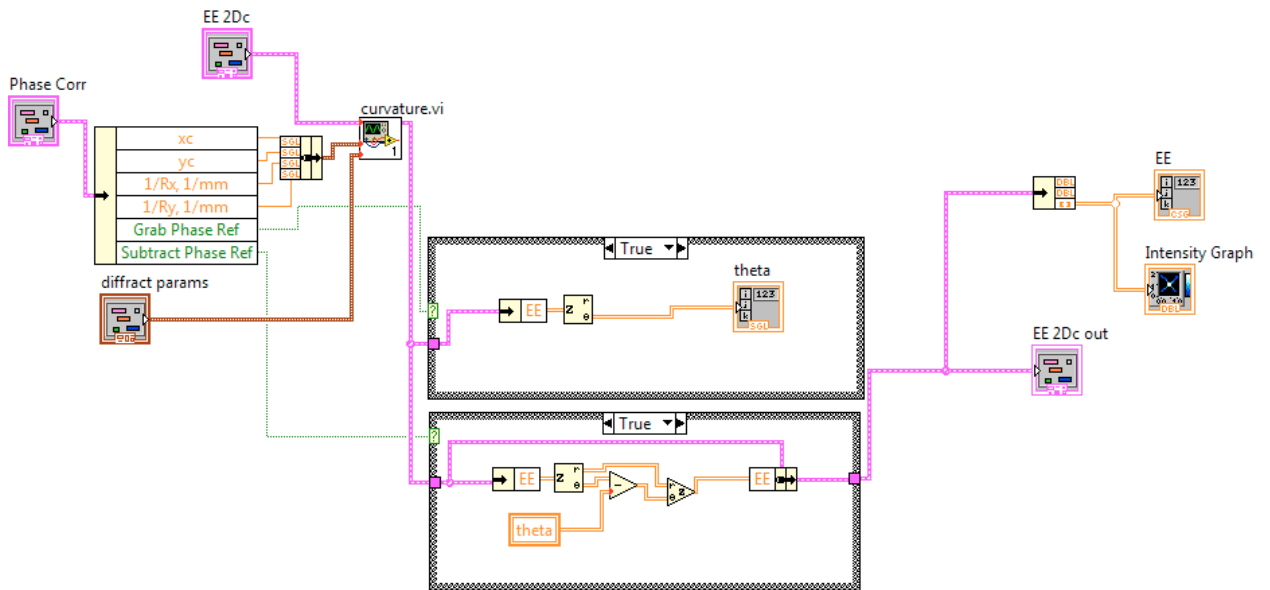


**Figure B.5.** Block diagram for general background phase aberration compensation.

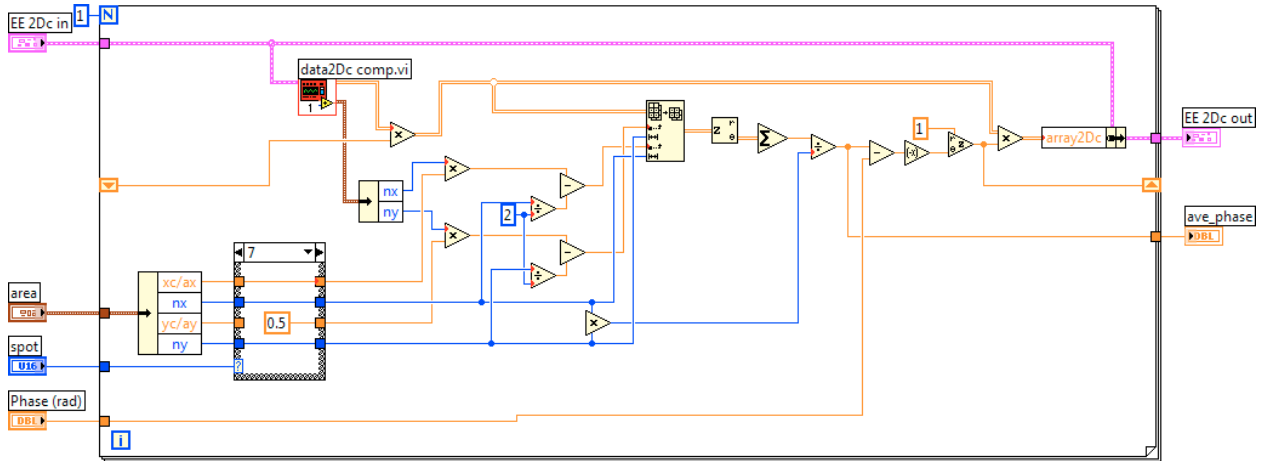


**Figure B.6.** Block diagram for phase level stabilization.

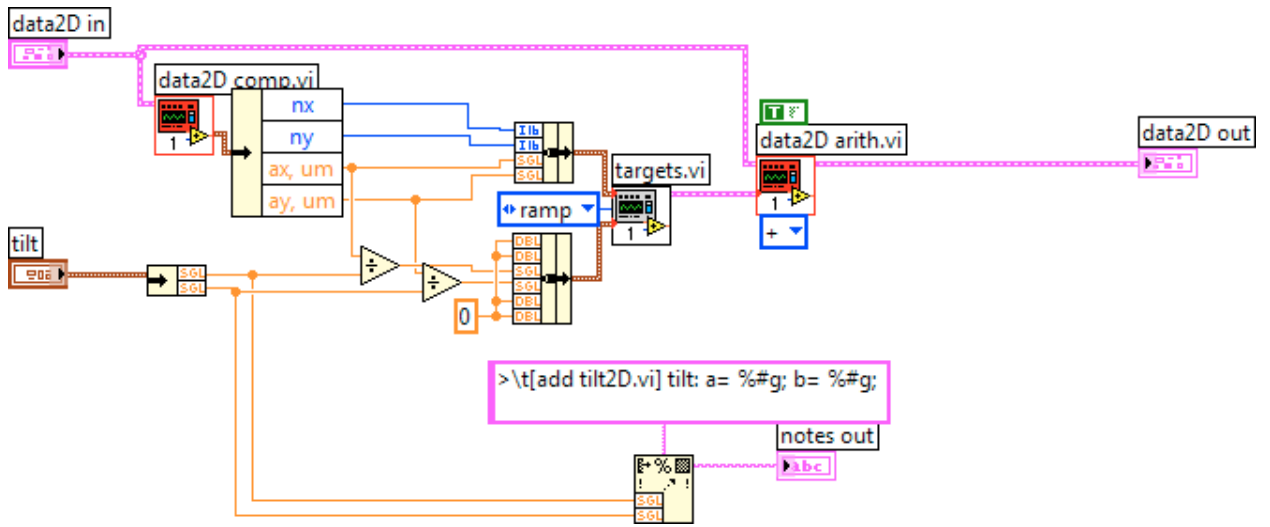


**Figure B.7.** Block diagram for phase tilt correction.

**MATLAB program “360QuadSymm.m” written to perform azimuthal averaging of axisymmetric phase image structures and to check the symmetry in four quadrants:**

```

%Written as LabVIEW MatLab Script, inputs: I, dx, dy, ROI,
Xc, Yc
%Compares symmetries in quadrants of I
rawmax=max(max(I)); rawmin=min(min(I));
rawr=(rawmax-rawmin);
%zr=1.58;
scale=1;           %=zr/rawr;
Irad=I*scale;
xc=round(Xc/dx);
yc=round(Yc/dy);
Itrim=Irad(yc-round(ROI/dy):yc+round(ROI/dy),xc-
round(ROI/dx):xc+round(ROI/dx));
Radialavg=zeros(1,ROI);
for n=0:round(ROI)
    [X,Y]=pol2cart(-.25*pi:pi/100:.25*pi,round(n/dx));
    X=round(X)+round(ROI/dx); Y=round(Y)+round(ROI/dy);
    Radial=zeros(size(X));
    for i=1:size(X,2)
        Radial(i)=Itrim(Y(i)+1,X(i)+1);
    end
    m=n+1; Radialavg1(m)=mean(Radial);
end
for n=0:round(ROI)
    [X,Y]=pol2cart(.75*pi:pi/100:1.25*pi,round(n/dx));
    X=round(X)+round(ROI/dx); Y=round(Y)+round(ROI/dy);
    Radial=zeros(size(X));
    for i=1:size(X,2)
        Radial(i)=Itrim(Y(i)+1,X(i)+1);
    end
    m=n+1; Radialavg2(m)=mean(Radial);
end
for n=0:round(ROI)
    [X,Y]=pol2cart(.25*pi:pi/100:.75*pi,round(n/dx));
    X=round(X)+round(ROI/dx); Y=round(Y)+round(ROI/dy);
    Radial=zeros(size(X));
    for i=1:size(X,2)
        Radial(i)=Itrim(Y(i)+1,X(i)+1);
    end
    m=n+1; Radialavg3(m)=mean(Radial);
end
for n=0:round(ROI)

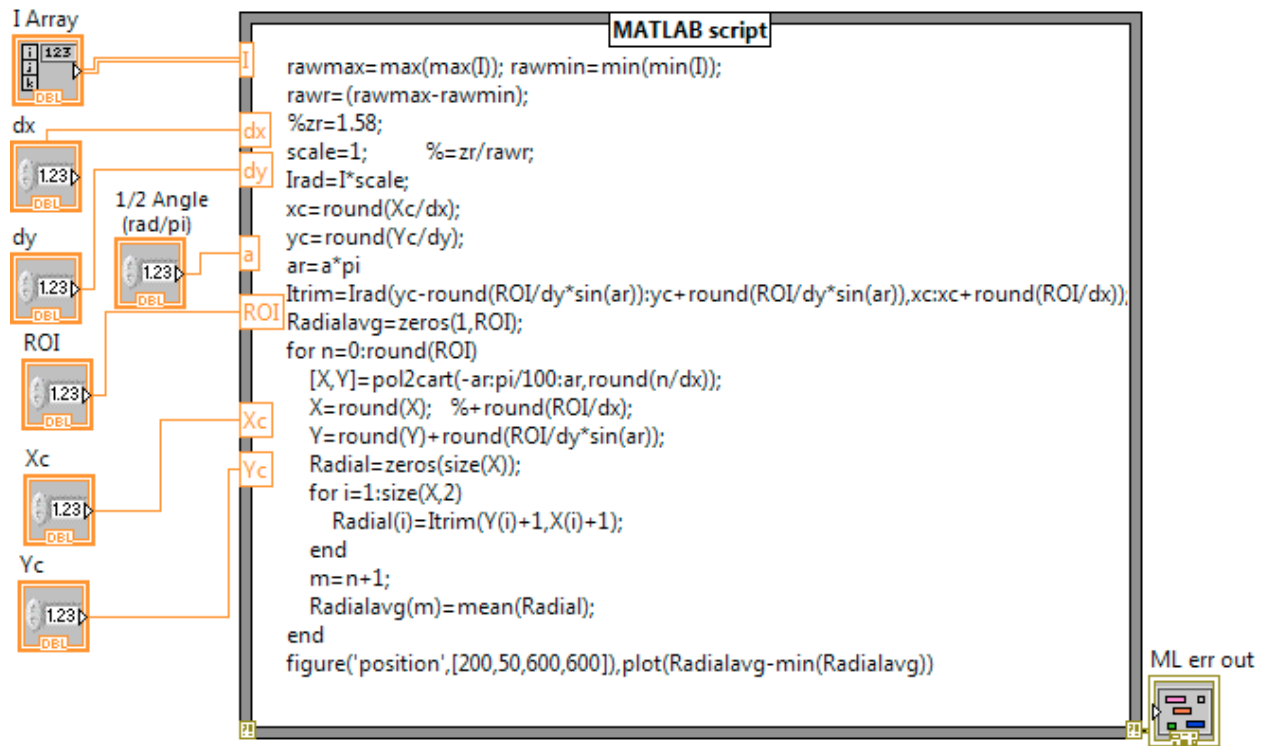
```

```

[X,Y]=pol2cart(1.25*pi:pi/100:1.75*pi,round(n/dx));
X=round(X)+round(ROI/dx); Y=round(Y)+round(ROI/dy);
Radial=zeros(size(X));
for i=1:size(X,2)
    Radial(i)=Itrim(Y(i)+1,X(i)+1);
end
m=n+1; Radialavg4(m)=mean(Radial);
end
RadialavgH = (Radialavg1+Radialavg2)/2;
RadialavgV = (Radialavg3+Radialavg4)/2;
Radialavg360 = (RadialavgH+RadialavgV)/2;
figure('position',[200,50,600,600]),plot(RadialavgH-
min(RadialavgH)), title('Horizontal')
figure('position',[300,50,600,600]),plot(RadialavgV-
min(RadialavgV)), tital('Vertical')
figure('position',[400,50,600,600]),plot(Radialavg360-
min(Radialavg360)), tital('360 Degree')
figure('position',[500,50,600,600])
subplot(2,2,2);plot(Radialavg1-min(Radialavg1)),
title('Right')
subplot(2,2,1);plot(Radialavg2-min(Radialavg2)),
title('Left')
subplot(2,2,3);plot(Radialavg3-min(Radialavg3)),
title('Top')
subplot(2,2,4);plot(Radialavg4-min(Radialavg4)),
title('Bottom')

```

**Compact version of above scripted into LabVIEW vi:**



**MATLAB program “PlotSeriesFigDataMODS.m” written to automate analysis of the output cross-sectional time-series data from optical pressure impulse**

**experiments:**

```
%Get data from time series .fig files, mesh plot all, track
and plot
%propagating wavefront, and use velocity to solve for
surface tension
clear;
d=997;
lamda=633e-9;
n1=1;
n2=1.333;
t=[10:10:90 100:50:500];
path='P:\CAS-PHY Kim Lab\AAA KimLab Folders\__folder 2009 -
Dave C\__data & notes - Dave\Optical Pressure\data 2012-02-
24\DI figs\di';
i=1;
for n=t
    if n<100
        num=num2str(n);
        file=strcat(path,'0',num,'.fig');
    else
        num=num2str(n);
        file=strcat(path,num,'v.fig');
    end
    s=hgload(file);
    h = findobj(s,'Type','line');
    z(i,:)=get(h,'ydata');
    x=get(h,'xdata')-1;
    close(s)
    z(i,:)=z(i,:)-mean(z(i,size(z,2)-100:size(z,2)));
    i=i+1;
end
trim=size(z,2);
figure(1);
surf(x(1:trim),t,z(:,1:trim)),colormap(jet),xlabel('Radial
Position (\num)'),ylabel('Time (\mus)'),zlabel('Phase Shift
(rad)'),title('Phase Response')
camorbit(120,20);shading flat;

%%%%%Determining Surface Tension%%%%%
```

```

[pk pkia]=max(z(:,1));
pki=pkia;
fin=size(t,2);
[~,pos]=min(transpose(z(pki:fin,1:800)));
%pos(1)=225; %%Enter a value in for input wavelength only
if check (fig3) indicates the need
linearCoef = polyfit(t(pki:fin),pos,1);
vel=linearCoef(1);
wn=pi/(pos(1)*1e-6);
s=vel^2*d/wn*1e3;
linearFit = polyval(linearCoef,t(pki:fin));
figure(2);
plot(t(pki:fin),pos,'s',t(pki:fin),linearFit,'r-
'),xlabel('Time(\mus)'),ylabel('Position
(\mum)'),title(['Density = ',num2str(d),' kg/m^3,
',' \kappa = ',num2str(wn),' m^-^1, ',' Velocity = ',
num2str(vel),' m/s'],['Peak@ ',num2str(t(pki)),' \mus',',',
Surface tension = ',num2str(s),' mN/m']])

%%%Checking wn selection
figure(3)
plot(x(1:400),z(pki,1:400)),xlabel('Radial Position (um)'),
ylabel('Phase Shift (rad)'),title(['Autoselected Wavelength
= ',num2str(pos(1)),' \mum'])

%%%%%%%%Alternative Relationship%%%%%%%%

posv=pos*1e-6/sqrt(wn);
linearCoef2 = polyfit(t(pki:fin)*1e-6,posv,1);
altm=linearCoef2(1);

s2=d*altm^2;
linearFit2 = polyval(linearCoef2,t(pki:fin)*1e-6);
figure(4);
plot(t(pki:fin),posv,'s',t(pki:fin),linearFit2,'r-
'),xlabel('Time(\mus)'),ylabel('Position/\surd\kappa
(m^3/^2)'),title(['Density = ',num2str(d),' kg/m^3,
',' \kappa = ',num2str(wn),' m^-^1, ',' Slope = ',
num2str(altm),' m^3/^2s^-^1'],['Peak@ ',num2str(t(pki)),'
\mus',',', Surface tension = ',num2str(s2*1e3),' mN/m']])

%%%%%%%%Additional Displays%%%%%%%%
%%Overlapping 2D time series
dfact=lamda/(2*pi*(n2-n1));
prange=[1:pki];
figure(5)

```

```
plot(x(1:trim),z(prange,1:trim)*dfact*1e9),xlabel('Radial  
Position (\num)'), ylabel('Z Position (nm)'),  
legend(num2str(transpose(t(prange))))
```

**MATLAB program “3Dbuild.m” written to reconstruct 3D representations of fully treated optical impulse surface response data:**

```
%%% Run PlotSeriesFigData.m first to build matrices z,t,
and x or import
%%% previously built matrices stored in builddata.mat
for i=1:20
    rho=z(i,:);
    sizes=size(rho,2);
    [theta,rr]=cart2pol(sizes,sizes);
    padrho=padarray(rho,[0 round(rr)-
sizes], 'replicate', 'post');

    for n=1:sizes
        for m=1:sizes
            [theta,rr]=cart2pol(n,m);
            cart(n,m)=padrho(round(rr));
        end
    end

    comp=padarray(cart,size(cart), 'symmetric', 'pre');
    padx=padarray(x,[0 size(x,2)], 'symmetric', 'pre')-1;
    padx(1,1:501)=padx(1,1:501)*-1;

    adjcomp=comp-comp(1,1);

    figure('position',[20,20,800,800])

    mesh(padx,padx,adjcomp*633/2/pi/.33),colormap(jet),xlabel('
Position (um)'),ylabel('Position (um)'),zlabel('Height
(nm)'),title({'t= ',num2str(t(i)), ' us'})
    zlim([-30 150]);caxis([-30 150])
    %halfs:

    %mesh(padx,padx(501:1002),adjcomp(501:1002,:)*633/2/pi/.33)
    ,colormap(jet),xlabel('Position (um)'),ylabel('Position
(um)'),zlabel('Height (nm)'),title({'t=
',num2str(t(i)+j*5), ' us'})
    %camorbit(50,-20); ylim([0 500])
    filen=char({'3D_',num2str(t(i))});
    saveas(gcf,[filen, '.fig'])
    export_fig([filen, '.bmp'])
end
```

**APPENDIX C**  
**LIST OF PUBLICATIONS**

**Peer-reviewed Journal Articles**

- D. C. Clark and M. K. Kim, "High-precision method for measuring the photothermal properties of transparent media with digital holography (Invited Paper)," *Chin. Opt. Lett.* **9**, 120001:1-4 (2011).
- D. C. Clark and M. K. Kim, "Determination of absorption coefficient by digital holographic measurement of optical excitation," *Appl. Opt.* **50**, 1668-1672 (2011).
- X. Yu, M. Cross, C. Liu, D. C. Clark, D. T. Haynie, and M. K. Kim, "Measurement of the traction force of biological cells by digital holography," *Biomed. Opt. Express* **3**, 153-159 (2011).
- D. C. Clark and M. K. Kim, "Noncontact single-pulse optical method to measure interfacial properties in intact systems," *Opt. Lett.*, (2012, under review).
- X. Yu, M. Cross, C. Liu, D. C. Clark, D. T. Haynie, and M. K. Kim, "Quantitative imaging and measurement of cell-substrate surface deformation by digital holography," *J. Mod. Opt.*, (2012, accepted for publication).

### **Refereed Conference Papers**

- D. C. Clark and M. K. Kim, "Noncontact single optical pulse method to measure cell membrane properties," in *Frontiers in Optics, OSA Technical Digest* (Optical Society of America, 2012).
- D. C. Clark and M. K. Kim, "Time-dependent surface response of fluid to transmission optical pressure impulse," in *Digital Holography and Three-Dimensional Imaging, OSA Technical Digest* (Optical Society of America, 2012).
- X. Yu, M. Cross, C. Liu, D. C. Clark, D. T. Haynie, and M. K. Kim, " Quantitative imaging of surface deformation on substrata due to cell motility by digital holography," in *Digital Holography and Three-Dimensional Imaging, OSA Technical Digest* (Optical Society of America, 2012).
- D. C. Clark and M. K. Kim, "Time-dependent phase response of fluid interface to optical excitation," in *Frontiers in Optics, OSA Technical Digest* (Optical Society of America, 2011).
- D. C. Clark and M. K. Kim, "Decoupling of thermal effects to image nanometric optical pressure deformation by digital holography," in *Digital Holography and Three-Dimensional Imaging, OSA Technical Digest* (Optical Society of America, 2011).
- C. Liu, X. Yu, D. C. Clark, and M. K. Kim, "Digital Holographic Adaptive Optics for Retinal Imaging," in *Digital Holography and Three-Dimensional Imaging, OSA Technical Digest* (Optical Society of America, 2011).

- X. Yu, C. Liu, D. C. Clark, and M. K. Kim, "Measurement of Young's Modulus of Polyacrylamide Gel by Digital Holography," in Digital Holography and Three-Dimensional Imaging, OSA Technical Digest (Optical Society of America, 2011).
- D. C. Clark and M. K. Kim, "Nanometric measurement of optical pressure deformation of fluid interface by digital holography," Proc. SPIE **7908**, 79080T (2011).
- D. C. Clark, L. Krzewina, and M. K. Kim, "Quantitative Analysis by Digital Holography of the Effect of Optical Pressure on a Biological Cell," in Digital Holography and Three-Dimensional Imaging and Biomedical Optics, OSA Technical Digest (Optical Society of America, 2010).
- W. M. Ash III, D. Clark, C. M. Lo, and M. K. Kim, "Quantitative Characterization of Cellular Adhesions with Total Internal Reflection Holographic Microscopy," in Digital Holography and Three-Dimensional Imaging, OSA Technical Digest (Optical Society of America, 2010).
- W. M. Ash, D. C. Clark, C-M Lo and M. K. Kim, "Total internal reflection holographic microscopy for quantitative phase characterization of cellular adhesion," Proc. SPIE **7568**, 756803 (2010).

## **ABOUT THE AUTHOR**

David Clark received a Bachelor of Science degree in Biology from the University of South Florida in 2000. It was during his following years as a public school science teacher that he discovered his fondness for the subject of physics. He then applied and was admitted into the physics graduate program at the University of Central Florida in 2004 and received his Master of Science degree in Physics in 2006. In 2007 he was admitted into the Ph.D. program in Applied Physics at the University of South Florida.

While in the Ph.D. program, David presented his work at many technical conferences by SPIE and OSA. He was also published in peer-reviewed journals such as Applied Optics, Biomedical Optics Express, Journal of Modern Optics, an invited paper in Chinese Optics Letters, and a paper under review for Optics Letters at the time of this dissertation. He won the Duckwall graduate research summer fellowship in 2011 and 2012. He was an elected official in the USF OSA student chapter from 2009-2012.